

# **ACOUSTIC TRANSDUCTION – MATERIALS AND DEVICES**

**Period 1 January 1998 to 31 December 1998**

**Annual Report**

**VOLUME II**

**OFFICE OF NAVAL RESEARCH  
Contract No: N00014-96-1-1173**

**APPROVED FOR PUBLIC RELEASE –  
DISTRIBUTION UNLIMITED**

**Reproduction in whole or in part is permitted for any  
purpose of the United States Government**

**Kenji Uchino**

**PENNSTATE**



**THE MATERIALS RESEARCH LABORATORY  
UNIVERSITY PARK, PA**

19990427 042

**Reproduced From  
Best Available Copy**

# REPORT DOCUMENTATION PAGE

Form Approved  
OMB No. 0704-0188

Public reporting burden for this collection of information is estimated to average 1 hour per response, including the time for reviewing instructions, searching existing data sources, gathering and maintaining the data needed, and completing and reviewing the collection of information. Send comments regarding this burden estimate or any other aspect of this collection of information, including suggestions for reducing this burden, to Washington Headquarters Services, Directorate for Information Operations and Reports, 1215 Jefferson Davis Highway, Suite 1204, Arlington, VA 22202-4302, and to the Office of Management and Budget, Paperwork Reduction Project (0704-0188), Washington, DC 20503.

1. AGENCY USE ONLY (Leave blank)		2. REPORT DATE 04/05/99	3. REPORT TYPE AND DATES COVERED ANNUAL REPORT 01/01/98-12/31/98	
4. TITLE AND SUBTITLE ACOUSTIC TRANSDUCTION -- MATERIALS AND DEVICES			5. FUNDING NUMBERS ONR CONTRACT NO: N00014-96-1-11173	
6. AUTHOR(S) KENJI UCHINO				
7. PERFORMING ORGANIZATION NAME(S) AND ADDRESS(ES) Materials Research Laboratory The Pennsylvania State University University Park PA 16802			8. PERFORMING ORGANIZATION REPORT NUMBER	
9. SPONSORING/MONITORING AGENCY NAME(S) AND ADDRESS(ES) Office of Naval Research ONR 321SS Ballston Centre Tower One 800 N Quincy Street Arlington VA 22217-5660 Office of Naval Research Regional Office Chicago 536 S Clark Str., RM 208 Chicago IL 60605-1588			10. SPONSORING/MONITORING AGENCY REPORT NUMBER	
11. SUPPLEMENTARY NOTES				
12a. DISTRIBUTION/AVAILABILITY STATEMENT			12b. DISTRIBUTION CODE	
13. ABSTRACT (Maximum 200 words)				
14. SUBJECT TERMS			15. NUMBER OF PAGES	
			16. PRICE CODE	
17. SECURITY CLASSIFICATION OF REPORT	18. SECURITY CLASSIFICATION OF THIS PAGE	19. SECURITY CLASSIFICATION OF ABSTRACT	20. LIMITATION OF ABSTRACT	

## ABSTRACT

This report documents work performed over the period 1 January 1998 to 31 December 1998 on a MURI under the Office of Naval Research Contract N00014-96-1-1173. The topic "Acoustic Transduction Materials and Devices" brings together groups in the Materials Research Laboratory (MRL), the Applied Research Laboratory (ARL), and the Center for Acoustics and Vibrations (CAV) at Penn State.

Research on the program is adequately represented in the 80 technical appendices.

Outstanding accomplishments include:

Exploration of several new relaxor ferroelectric perovskite solid solution with morphotropic phase boundaries. New evidence of the onset of nonlinearity in soft donor doped PZTs at surprisingly low (1V/cm) fields. Confirmation of the relaxor phase induced by electron irradiation in PVDF:TrFE copolymers, and a processing method which permits very high (4%) electrostrictive strain in the transverse direction, vital for the practical use in actuator systems. In composite transducer, "first fruits" of the cooperative program are cymbal arrays which form most effective acoustic projectors, and a new "dog bone" design which permits deeper submergence for the cymbal. Agile transducers, the 3-D acoustic intensity probe and high force high strain torsional and step and repeat systems continue to make excellent progress. In actuator studies true acoustic emission is proving to be an excellent tool in reliability studies and a new design of small-scale (mini) piezoelectric motor shows outstanding performance. Thick thin film studies and are now "gearing up" for the development of the mini tonpilz arrays. New combinations of ultrasonic and resonance methods appear to offer unique capability for complete characterization of ferroelectric piezoelectric materials.

The mode of presentation of the report emphasizes the outstanding progress made in published research. It is important to also document that the slower and more painstaking development of practical transducer systems in the cymbal and mini tonpilz arrays is progressing very favorably.

## APPENDICES

### VOLUME I

#### GENERAL SUMMARY PAPERS

1. Cross, L.E., "Recent Developments in Piezoelectric Ferroelectric Materials and Composites," Proceedings of the 4<sup>th</sup> European Conference on Smart Structures and Materials in Conjunction with the 2<sup>nd</sup> International Conference on Micromechanics, Intelligent Materials and Robotics, Harrogate, UK (6-8 July 1998).
2. Newnham R.E., "Functional Composites for Sensors and Actuators," Chapter in *The Era of Materials*, edited by S. Majumdar, R. Tressler, and E. Miller, 259-275, Pennsylvania Academy of Science (1998).
3. Uchino, K., "Piezoelectric Ultrasonic Motors: Overview," *Smart Mater. Struct.* **7**, 273-285 (1998).
4. Newnham, R.E., "Phase Transformations in Smart Materials," *Acta Cryst. A* **54**, 729-737 (1998).

#### 2.0 MATERIALS STUDIES

##### 2.1 Polycrystal Perovskite Ceramics

5. Liu, S.F., I.R. Abothu, S. Komarneni, P. Poosanaas, D.S. Paik, Y. Ito, and K. Uchino, "PLZT Ceramics from Conventional and Microwave Hydrothermal Powders," Proceedings in Asian Meeting on Ferroelectrics (AMF2), Singapore (December 8-11, 1998).
6. Abothu, I.R., P. Poosanaas, S. Komarneni, Y. Ito, and K. Uchino, "Nanocomposite Versus Monophasic Sol-Gel Processing of PLZT Ceramics," Proceedings in Asian Meeting on Ferroelectrics (AMF2), Singapore (December 8-11, 1998).
7. Kim, J.S., Y.H. Chen, and K. Uchino, "Dielectric and Piezoelectric Properties of Fe<sub>2</sub>O<sub>3</sub>-Doped 0.57PSN-0.43PT Ceramics," *J. Korean Phys. Soc.* **32** [2], S1248-1250 (1998).
8. Alberta, E.F. and A.S. Bhalla, "Electrical Property Diagram and Morphotropic Phase Boundary in the Pb(In<sub>1/2</sub>Ta<sub>1/2</sub>)O<sub>3</sub>-PbTiO<sub>3</sub> Solid Solution System," *Ferroelectric Letters* (1998). [accepted]
9. Meng, J.F., Z.-Y. Cheng, B.K. Rai, R.S. Katiyar, E. Alberta, R. Guo, and A.S. Bhalla, "Photoluminescence in PbMg<sub>1/3</sub>Nb<sub>2/3</sub>O<sub>3</sub>-PbIn<sub>1/2</sub>Nb<sub>1/2</sub>O<sub>3</sub> Systems," *J. Mater. Res.* **13** (7), 1861 (1998).
10. Alberta, E.F. and A.S. Bhalla, "Investigation of the Lead Indium Niobate-Lead Magnesium Niobate Solid Solution," *Materials Letters* (1998). [accepted]
11. Alberta, E.F., A.S. Bhalla, and T. Takenaka, "Large Hydrostatic Piezoelectric Constant and Temperature Dependence of the Piezoelectric Properties of Bi(NiTi)<sub>1/2</sub>O<sub>3</sub>:PbTiO<sub>3</sub> Ceramics," *Ferroelectrics Letters* (1998). [accepted]
12. Zhang, Q.M. and J. Zhao, "Electromechanical Properties of Lead Zirconate Titanate Piezoceramics Under the Influence of Mechanical Stress, *IEEE Trans. UFFFC* (accepted).
13. Kugel, V.D. and L.E. Cross, "Behavior of soft Piezoelectric Ceramics under High Sinusoidal Electric Fields," *J. Appl. Phys.* **84** (5), 2815-2830 (1998).

## VOLUME II

### 2.0 MATERIALS STUDIES

#### 2.1 *Polycrystal Perovskite Ceramics* (continued)

14. Du, X-H., Q.M. Wang, U. Belegundu, and K. Uchino, "Piezoelectric Property Enhancement in Polycrystalline Lead Zirconate Titanate by Changing Cutting Angle," J. Ceram. Soc. Jpn. (1999). [accepted]
15. Mueller, V. and Q.M. Zhang, "Nonlinearity and Scaling Behavior in Donor Doped Lead Zirconate Titanate Piezoceramic," Appl. Phys. Lett. **72**, 2692 (1998).
16. Uchino, K and H. Aburatani, "Field Induced Acoustic Emission in Ferroelectric Ceramics," Proc. IEEE Ultrasonic Symp., Sendai, Japan (October 1998). [in press]
17. Newnham, R.E. and S. Trolier-McKinstry, "Size Effects in Ferroics" Integrated Ferroelectrics **20**, 1-13, Gordon & Breach Science Publishers (March 1998).

#### 2.2 *Relaxor Ferroelectric Single Crystal Systems*

18. Uchino, K., "High Electromechanical Coupling Piezoelectrics: Relaxor and Normal Ferroelectric Solid Solutions," Solid State Ionics **108**, 43-52 (1998).
19. Wada, S. S.E. Park, L.E. Cross, and T.R. Shrout, "Domain Configuration and Ferroelectric Related Properties of Relaxor Based Single Crystals," J. Korean Phys. Soc. **32**, S1290-S1293 (1998).
20. Belegundu, U., X. H. Du, and K. Uchino, "In-Situ Observation of Domain Orientation in  $\text{Pb}(\text{Zn}_{1/3}\text{Nb}_{2/3})\text{O}_3\text{-PbTiO}_3$  Single Crystals," Proc. 5<sup>th</sup> Intl. Symp. Ferroic Domains and Mesoscopic Structures, University Park, PA (April 1998).
21. Du, X.H., J. Zheng, U. Belegundu, and K. Uchino, "Crystal Orientation Dependence of Piezoelectric Properties of Lead Zirconate Titanate Near the Morphotropic Phase Boundary," J. Appl. Phys. Ltrs. **72** (19), 2421-2423 (1998).
22. Rehrig, P.W., S.-E. Park, S. Trolier-McKinstry, G.L. Messing, B. Jones, and T.R. Shrout, "Piezoelectric Properties of Zirconium-Doped Barium Titanate Single Crystals Grown by Templated Grain Growth," submitted to J. Appl. Phys.
23. Du, X., Q.M. Wang, U. Belegundu, A. Bhalla, and K. Uchino, "Crystal Orientation Dependence of Piezoelectric Properties of Single Crystal Barium Titanate," Mat. Ltr. (1999) [accepted].
24. Guo, R., H.T. Evans, Jr., and A.S. Bhalla, "Crystal Structure Analysis and Polarization Mechanisms of Ferroelectric Tetragonal Tungsten Bronze Lead Barium Niobate," Ferroelectrics **206/207**, 123-132 (1998).

#### 2.3 *New High Strain Polymer Materials*

25. Zhao, X., V. Bharti, Q.M. Zhang, T. Ramotowski, F. Tito, and R. Ting, "Electromechanical Properties of Electrostrictive P(VDF-TrFE) Copolymer," Appl. Phys. Ltrs. **73**, 2054 (1998).
26. Bharti, V., G. Shanthi, H. Xu, Q.M. Zhang, and K. Liang, "Evolution of Transitional Behavior and Structure of Electron Irradiated Poly(vinylidene fluoride-trifluoroethylene) Copolymer Films," Appl. Phys. Ltrs. [accepted].
27. Cheng, Z.-Y., V. Bharti, T.B. Xu, S. Wang, and Q.M. Zhang, "Transverse Strain Responses in Electrostrictive Poly (vinylidene fluoride-trifluoroethylene) Films and Development of a Dilatometer for the Measurement," J. Appl. Phys. [accepted]

### VOLUME III

#### 2.0 MATERIALS STUDIES

##### 2.3 *New High Strain Polymer Materials* (continued)

28. Bharti, V., X.Z. Zhao, Q.M. Zhang, T. Ramotowaski, F. Tito, and R. Ting, "Ultrahigh Field Induced Strain and Polarized Response in Electron Irradiated Poly(vinylidene fluoride-trifluoroethylene) Copolymer," *Mat. Res. Innovat.* **2**, 57-63 (1998).
29. Su, J., P. Moses, and Q.M. Zhang, "A Bimorph Based Dilatometer for Field Induced Strain Measurement in Soft and Thin Free Standing Polymer Films," *Rev. Sci. Instruments* **69** (6), 2480 (1998).

#### 3.0 TRANSDUCER STUDIES

##### 3.1 *Composite Structures*

30. Hughes, W.J., "Transducers, Underwater Acoustic," *Encyclopedia of Applied Physics*, Vol. 22, 67 (1998).
31. Tressler, J.F., W.J. Hughes, W. Cao, K. Uchino, and R.E. Newnham, "Capped Ceramic Underwater Sound Projector."
32. Zhang, J., W.J. Hughes, A.C. Hladky-Hennion, and R.E. Newnham, "Concave Cymbal Transducers."
33. Wang, Q.M., X.-H. Du, B. Xu, and L.E. Cross, "Theoretical Analysis of the Sensor Effect of Cantilever Piezoelectric Benders," *J. Appl. Phys.* **85** (3), 1702-1712 (1998).
34. Fernandez, J.F., A. Dogan, J.T. Fielding, K. Uchino, and R.E. Newnham, "Tailoring the Performance of Ceramic-Metal Piezocomposite Actuators, 'Cymbals'," *Sensors and Actuator A65*, 228-237 (1998).
35. Wang, Q.M. and L.E. Cross, "A Piezoelectric Pseudoshear Multilayer Actuator," *Appl. Phys. Ltrs.* **72** (18), 2238 (1998).
36. Geng, X. and Q.M. Zhang, "Resonance Modes and Losses in 1-3 Composites for Ultrasonic Transducer Applications," *J. Appl. Phys.* **85** (3), 1342 (1999).

##### 3.2 *Frequency Agile Transducers*

37. Hebert, C.A. and G. A. Lesieutre, "Flexural Piezoelectric Transducers with Frequency Agility Obtained Via Membrane Loads," *J. Intel. Mat. Sys. & Str.* (1998). [accepted].
38. Davis, C.L. and G.A. Lesieutre, "An Actively Tuned Solid State Vibration Absorber Using Capacitive Shunting of Piezoelectric Stiffness," *J. Sound & Vibration* (1998). [accepted]
39. Bernard, J., G.A. Lesieutre, and G.H. Koopmann, "Active Broadband Force Isolation using a Flexural Piezoelectric Inertial Actuator," *J. Sound & Vibration* (1999). [submitted]

## VOLUME IV

### 3.0 TRANSDUCER STUDIES

#### 3.3 *3-D Acoustic Intensity Probes* (continued)

- 40. Lauchle, G.C. and A.R. Jones, "Unsteady Lift Force on a Towed Sphere," *J. Fluids and Structures* **112** (1998).
- 41. Lauchle, G.C., A.R. Jones, J.J. Dreyer, and J. Wang, "Flow-Induced Lift Forces on a Towed Sphere," *Proc. Of ASME Noise Control and Acoustics Division ASME 1998, NCA-28*, 103-111 (1998).
- 42. Brungart, T.A. G.C. Lauchle, S. Deutsch, and E. Riggs, "Outer-Flow Effects on Turbulent Boundary Layer Wall Pressure Fluctuations," *J. Acoust. Soc. Am.* **105** (4) (April 1999).
- 43. Brungart, T.A., G.C. Lauchle, and R.K. Ramanujam, "Installation Effects of Fan Acoustic and Aerodynamic Performance," *Noise Control Eng. J.* **47** (January/February 1999).

### 4.0 ACTUATOR STUDIES

#### 4.1 *Materials : Designs : Reliability*

- 44. Uchino, K., "New Trend in Ceramic Actuators," *Proc. 6<sup>th</sup> Intl. Aerospace Symp. '98*, Nagoya, Japan, p. S1-2, 1-10 (July 14-15, 1998).
- 45. Uchino, K., "Materials Issues in Design and Performance of Piezoelectric Actuators: An Overview," *Acta. Mater.* **46** (11), 3745-3753 (1998).
- 46. Yao, K., W. Zhu, K. Uchino, Z. Zhang, and L.C. Lim, "Design and Fabrication of a High Performance Multilayer Piezoelectric Actuator with Bending Deformation."
- 47. Aburatani, H. and K. Uchino, "Acoustic Emission in Damaged Ferroelectric Lead Zirconate Titanate Ceramics," *Jpn. J. Appl. Phys.* **37**, L553-L555 (1998).
- 48. Atherton, P.D. and K. Uchino, "New Developments in Piezo Motors and Mechanisms," *Proc. 6<sup>th</sup> Intl. Conf. On New Actuators (Actuator 98)*, Bremen, Germany, p. 164-169 (June 17-19, 1998).
- 49. Uchino, K. and B. Koc, "Compact Piezoelectric Ultrasonic Motors," *2<sup>nd</sup> Asian Meeting on Ferroelectrics (AMF-2)*, Singapore (December 7-11, 1998).
- 50. Koc, B., Y. Xu, and K. Uchino, "Ceramic/Metal Composite Piezoelectric Motors," *IEEE Ultrasonic Symposium*, Sendai, Japan (October 1998).
- 51. Koc, B., Y. Xu, and K. Uchino, "Roto-Linear Ultrasonic Motors," *Proc. 6<sup>th</sup> Intl. Conf. On New Actuators (Actuator 98)*, Bremen, Germany, p. 349-352 (June 17-19, 1998).
- 52. Koc, B., A. Dogan, Y. Xu, R.E. Newnham, and K. Uchino, "An Ultrasonic Motor Using a Metal-Ceramic Composite Actuator Generating Torsional Displacement," *Jpn. J. Appl. Phys.* **37**, 5659-5662 (1998).

#### 4.2 *Photostrictive Actuators*

- 53. Poosanaas, P. and K. Uchino, "Photostrictive Effect in Lanthanum-Modified Lead Zirconate Titanate Ceramics Near The Morphotropic Phase Boundary," *J. Mat. Chem. & Phys.* (October 1998). [submitted]
- 54. Uchino, K. and P. Poosanaas, "Photostriction in PLZT and Its Applications," *Proc. CIMTEC '98*, Florence, Italy (June 14-19, 1998).

## VOLUME V

### 4.0 ACTUATOR STUDIES

#### 4.3 *Torsional and High Force Actuators (continued)*

- 55. Glazounov, A.E., Q.M. Zhang, and C. Kim, "Torsional Actuator Based on Mechanically Amplified Shear Piezoelectric Response," *Sensors and Actuators* (1998). [submitted]
- 56. Frank, J., G.H. Koopmann, W. Chen, and G.A. Lesieutre, "Design and Performance of a High Force Piezoelectric Inchworm Motor."

### 5.0 MODELING and CHARACTERIZATION

#### 5.1 *Finite Element and Other Methods*

- 57. Qi, W. and W. Cao, "Finite Element and Experimental Study of Composite and 1-D Array Transducers," *SPIE* **3341** (1998).
- 58. Wang, H., W. Jiang, and W. Cao, "Characterization of Lead Zirconate Titanate Piezoceramic Using High Frequency Ultrasonic Spectroscopy," *J. Appl. Phys.* (1998). [accepted]
- 59. Zhu, S.N., B. Jiang, and W. Cao, "Characterization of Piezoelectric Materials Using Ultrasonic and Resonant Techniques," *Proceedings of SPIE Imaging '98*, **3341**, 154-162 (1998).
- 60. Cao, W., "Virtual Design of Medical Transducers," *Proceedings of SPIE Imaging '98*, **3341**, 56-63 (1998).
- 61. Cao, W., "Elastic Property Characterization in Thin Samples of Sub-Wavelength in Thickness," *Ferroelectrics* **206/207**, 355-363 (1998).
- 62. Cao, W., S.N. Zhu, and B. Jiang, "Analysis of Shear Modes in A Piezoelectric Resonator," *J. Appl. Phys.* **83**, 4415-4420 (1998).

#### 5.2 *Relaxor Ferroelectrics*

- 63. Giniewicz, J.R., A.S. Bhalla, and L.E. Cross, "Variable Structural Ordering in Lead Scandium Tantalate-Lead Titanate Materials," *Ferroelectrics* **211**, 281-297 (1998).
- 64. Pan, X., W.D. Kaplan, M. Rühle, and R.E. Newnham, "Quantitative Comparison of Transmission Electron Microscopy Techniques for the Study of Localized Ordering on a Nanoscale," *J. Am. Ceram. Soc.* **81** (3), 597-605 (1998).
- 65. Zhao, J., A.E. Glazounov, and Q.M. Zhang, "Change in Electromechanical Properties of 0.9PMN:0.1PT Relaxor Ferroelectric Induced by Uniaxial Compressive Stress Directed Perpendicular to the Electric Field," *Appl. Phys. Lett.* **74**, 436 (1999).
- 66. Zhao, J., V. Mueller, and Q.M. Zhang, "The Influence of the External Stress on the Electromechanical Response of Electrostrictive  $0.9\text{Pb}(\text{Mg}_{1/3}\text{Nb}_{2/3})\text{O}_3$ - $0.1\text{PbTiO}_3$  in the dc Electrical Field Biased State," *J. Mat. Res.* **14**, 3 (1999).

## VOLUME VI

### 5.0 MODELING and CHARACTERIZATION

#### 5.3 *Thin and Thick Thin Films*

67. Maria, J.P., W. Hackenberger, and S. Trolier-McKinstry, "Phase Development and Electrical Property Analysis of Pulsed Laser Deposited  $\text{Pb}(\text{Mg}_{1/3}\text{Nb}_{2/3})\text{O}_3$ - $\text{PbTiO}_3$  (70/30) Epitaxial Films," J. Appl. Phys. **84** (9), 5147-5154 (1998).
68. Shepard, J.F., Jr., P.J. Moses, and S. Trolier-McKinstry, "The Wafer Flexure Technique for the Determination of the Transverse Piezoelectric Coefficient ( $d_{31}$ ) of PZT Thin Films," Sensors and Actuators A **71**, 133-138 (1998).
69. Zavala, G. J.H. Fendler, and S. Trolier-McKinstry, "Stress Dependent Piezoelectric Properties of Ferroelectric Lead Zirconate Titanate Thin Films by Atomic Force Microscopy," J. Korean Phys. Soc. **32**, S1464-S467 (1998).
70. Wasa, K., Y. Haneda, T. Satoh, H. Adachi, I. Kanno, K. Setsune, D.G. Schlom, S. Trolier-McKinstry, C.-B. Eom, "Continuous Single Crystal  $\text{PbTiO}_3$  Thin Films Epitaxially Grown on Miscal (001)  $\text{SrTiO}_3$ ," J. Korean Phys. Soc. **32**, S1344-S1348 (1998).
71. Xu, B., Y. Ye, L.E. Cross, J.J. Bernstein, and R. Miller, "Dielectric Hysteresis from Transverse Electric Fields in Lead Zirconate Titanate Thin Films," Appl. Phys. Ltrs. (1998). [submitted]
72. Xu, B., N.G. Pai, Q.-M. Wang, and L.E. Cross, "Antiferroelectric Thin and Thick Films for High Strain Microactuators," Integrated Ferroelectrics **22**, 545-557 (1998).

#### 5.4 *Domain Studies*

73. Erhart, J. and W. Cao, "Effective Material Properties in Twinned Ferroelectric Crystals," J. Appl. Phys. (1999). [submitted]
74. Belegundu, U., M. Pastor, X.H. Du, L.E. Cross, and K. Uchino, "Domain Formation in  $0.90\text{Pb}(\text{Zn}_{1/3}\text{Nb}_{2/3})\text{O}_3$ - $0.10\text{PbTiO}_3$  Single Crystals under Electric Field along [111] Direction," IEEE '98, Sendai, Japan (1998).
75. Zhu, S.N. and W. Cao, "Pyroelectric and Piezoelectric Imaging of Ferroelectric Domains in  $\text{LiTaO}_3$  by Scanning Electron Microscopy," Phys. Status Solidi (1998). [submitted]
76. Hatch, D.M. and W. Cao., "Determination of Domain and Domain Wall Formation at Ferroic Transitions," Ferroelectric (1998). [submitted]
77. Mueller, V. and Q.M. Zhang, "Threshold of Irreversible Domain Wall Motion in Soft PZT-Piezoceramic. Ferroelectrics **206/207**, 113-122 (1998).
78. Aburatani, H., J.P. Witham, and K. Uchino, "A Fractal Analysis on Domain Related Electric Field Induced Acoustic Emission in Ferroelectric Ceramics," Jpn. J. Appl. Phys. **37**, 602-605 (1998).

### 5.5 Electrostriction

79. Newnham, R.E., V. Sundar, R. Yimnirun, J. Su, and Q.M. Zhang, "Electrostriction in Dielectric Materials," in *Advances in Dielectric Ceramic Materials*, eds. K. Nair and A. Bhalla. Ceramic Trans. **88**, 154-39 (1998).
80. Sundar, V., R. Yimnirun, B.G. Aitken, and R.E. Newnham, "Structure Property Relationships in the Electrostriction Response of Low Dielectric Permittivity Silicate Glasses," Mat. Res. Bull. **33**, 1307-1314 (1998).

# **APPENDIX 14**

# **Piezoelectric property enhancement in polycrystalline lead zirconate titanate by changing cutting angle**

Xiao-hong Du, Qing-ming Wang, Uma Belegundu and Kenji Uchino<sup>a)</sup>

International Center for Actuators and Transducers, Materials Research Laboratory

The Pennsylvania State University, University Park, Pennsylvania 16802

## **ABSTRACT**

The effective piezoelectric strain constant  $d_{33}$  and electromechanical coupling factor  $k_{33}$  of polycrystalline lead zirconate titanate (PZT) at different cutting angles have been measured by using the IEEE standard resonance method. It was found that for tetragonal PZT 48/52, the effective  $d_{33}$  and  $k_{33}$  monotonously decreases as the cutting angle canted from the poling direction increases. However, for rhombohedral PZT 54/46, the effective  $d_{33}$  has the maximum value along a direction which is canted about  $45^\circ$  away from the poling direction, while the effective electromechanical coupling factor is not sensitive to the cutting direction and remains almost constant in the cutting angle range from  $0^\circ$  to  $45^\circ$ .

<sup>a)</sup>Electronic mail: [kenjiuchino@psu.edu](mailto:kenjiuchino@psu.edu)

Lead zirconate titanate (PZT) ceramics have been widely used in transducers and actuators due to the large piezoelectric coefficients and high electromechanical coupling factors. In these applications, the ceramic is electrically driven along a direction either parallel to the poling direction ( $0^\circ$  cutting angle) to utilize the longitudinal extension deformation or perpendicular to the poling direction ( $90^\circ$  cutting angle) to utilize the shear deformation. To the author's knowledge, no systematic investigations have been done to enhance the piezoelectric properties by choosing an electrical driven direction which is canted between  $0^\circ$  and  $90^\circ$  away from the poling direction. This paper presents the experimental results about such enhancement.

In the previous papers,<sup>1, 2</sup> we reported the phenomenological calculations of the piezoelectric and dielectric constants of hypothetical single crystals of PZT in different crystal orientations. For a tetragonal PZT, the effective piezoelectric constant  $d_{33}$  monotonously decreases as the crystal cutting angle from the spontaneous polarization direction  $[001]$  increases. However, for a rhombohedral PZT, the effective piezoelectric constant  $d_{33[001]//}$  along the perovskite  $[001]$  direction was found to be much larger than those along the spontaneous polarization direction  $[111]$ . A similar tendency can be expected for polycrystalline samples, though the enhancement might be less significant than single crystals.

Tetragonal PZT 48/52 and rhombohedral PZT 54/46 ceramic plates with sizes  $10\text{mm} \times 10\text{mm} \times 1\text{mm}$  were poled along one of the large sides, as shown in Fig. 1. Then, the plate were cut into small bars along the directions canted  $0^\circ$ ,  $15^\circ$ ,  $30^\circ$ ,  $45^\circ$ ,  $60^\circ$ , and  $75^\circ$  away from the poling direction, respectively. The IEEE standard resonance method<sup>3</sup> was used to measure the longitudinal extensional piezoelectric constant  $d_{33}$  and electromechanical coupling factor  $k_{33}$  for each bar. Figure 2 shows the values of  $d_{33}$  with respect to the cutting angles away from the poling direction. The values of  $d_{33}$  have been normalized by  $d_{33//Ps}$ , the  $d_{33}$  along the poling direction. Figure 3 shows the results for  $k_{33}$ . For tetragonal PZT 48/52, both  $d_{33}$  and  $k_{33}$  monotonously decrease as the cutting angle increases. However, for rhombohedral PZT 54/46,  $d_{33}$  increases as

the cutting angle increases from  $0^\circ$  to  $45^\circ$ , leading 1.25 time enhancement at  $45^\circ$ ;  $k_{33}$  is not sensitive to the cutting direction and remains almost constant in this cutting angle range. Beyond this cutting angle range, both  $d_{33}$  and  $k_{33}$  decrease as the cutting angle increases. This maximum angle is little smaller than the calculated angle  $56^\circ - 59^\circ$  for the hypothetical PZT crystals.

In conclusion, for tetragonal PZT 48/52, the effective piezoelectric constant  $d_{33}$  and electromechanical coupling factor  $k_{33}$  have the maximum values along the poling direction and decrease monotonously as the cutting angle from the poling direction increases. However, for rhombohedral PZT,  $d_{33}$  has the maximum value at a cutting angle about  $45^\circ$  away from the poling direction. This shows us that the enhancement of piezoelectric properties by changing the cutting direction away from the polarization direction exists not only in single crystals, but also in polycrystalline solids. By choosing an appropriate cutting direction, the piezoelectric properties can be improved.

#### ACKNOWLEDGE

This work was supported by the Office of Naval Research under contract: N00014-91-J4145.

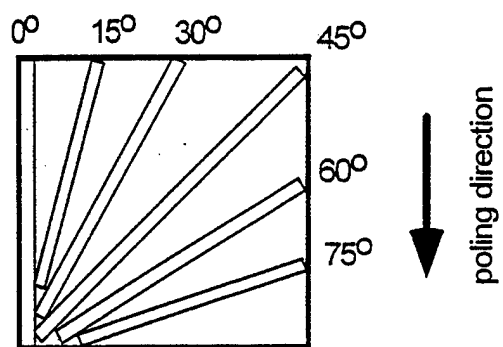
#### REFERENCES

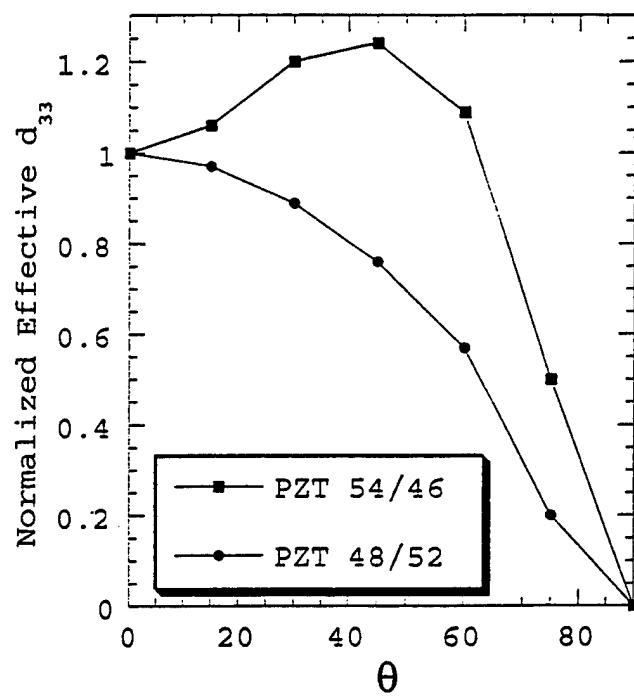
- <sup>1</sup>X. Du, U. Belegundu, and K. Uchino, Jpn. J. Appl. Phys., Part 1 **36**, 5580 (1997).
- <sup>2</sup>X. Du, J. Zheng, U. Belegundu and K. Uchino, Appl. Phys. Lett. **72**, 2421 (1998).
- <sup>3</sup>ANSI/IEEE, IEEE Standard on Piezoelectricity, Std 176-1987 (IEEE, New York, 1987).

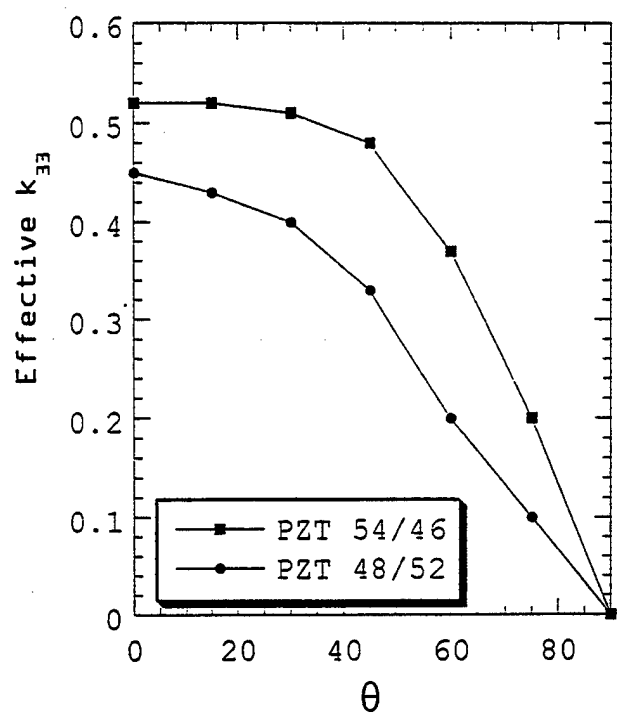
Fig. 1. Illustration of sample cutting.

Fig. 2. The effective  $d_{33}$  normalized by  $d_{33//P_s}$ , the  $d_{33}$  along the poling direction, with respect to cutting angles from the poling direction. For tetragonal PZT 48/52,  $d_{33//P_s}=98\text{pC/N}$ . For rhombohedral PZT 54/46,  $d_{33//P_s}=148\text{pC/N}$ .

Fig. 3. The effective  $k_{33}$  with respect to cutting angles from the poling direction.







# **APPENDIX 15**

# Nonlinearity and scaling behavior in donor-doped lead zirconate titanate piezoceramic

Volkmar Mueller<sup>a)</sup> and Q. M. Zhang

Materials Research Laboratory, The Pennsylvania State University, University Park, Pennsylvania 16802

(Received 1 October 1997; accepted for publication 22 March 1998)

Two different effective thresholds for the onset of nonlinearity in the dielectric and piezoelectric coefficients of donor-doped lead zirconate titanate (soft PZT) piezoceramics at electric ac fields  $E_{c1} \approx 100$  V/cm and  $E_{c2} \approx 1$  V/cm are found. Both are characterized by a scaling behavior  $x = x_0 - A[E - E_c]/E_c^\phi$  above the respective threshold, where  $x$  is the dielectric or piezoelectric coefficient. The values of the effective exponent  $\phi$  are apparently independent of the particular ceramic system which suggests a universal behavior in soft PZT. We suggest that the nonlinearity is dominated by the dynamics of domain walls in a randomly pinned medium. © 1998 American Institute of Physics. [S0003-6951(98)03521-9]

$\text{Pb}(\text{Zr}_{1-x}\text{Ti}_x)\text{O}_3$  (PZT) piezoceramics used in actuators, transducers, resonators, and motors are often subjected to high electric fields where the polarization-field and strain-field dependencies are strongly nonlinear.<sup>1</sup> For proper applications of the material, it is imperative to understand the nonlinear behavior. In PZT piezoceramics, it is well known that the dielectric and piezoelectric properties are influenced greatly by the motion of domain walls.<sup>2</sup> In donor-doped (soft) PZT [at compositions near the morphotropic phase boundary where  $x=0.52$  (MPB)], experimental results indicate a threshold for the onset of nonlinearity at  $E_c \approx 100$  V/cm (Refs. 3 and 4) which is believed to be due to the onset of irreversible domain wall motion. However, the mechanisms causing the domain-wall-related nonlinearity are not well understood.

In this letter, we present the results of a recent experimental investigation of the nonlinear dielectric and electro-mechanical response of soft PZT piezoceramics. We find, in addition to the threshold reported earlier, another threshold for the onset of nonlinearity at a much weaker field level. Above both thresholds, a nonanalytic scaling behavior,

$$x(E) = x_0 + A[(E - E_c)/E_c]^\phi, \quad (1)$$

of nonlinear responses is found characterized by an effective exponent  $\phi$  which is independent of the material investigated. Hence, this scaling behavior provides a convenient way of describing the nonlinear behavior of soft PZT piezoceramics. In addition, it also indicates a possible link of the nonlinearity with the depinning of ferroelectric domain walls as will be discussed.

A series of commercial soft PZT ceramics all at compositions near MPB with different dopants ( $\geq 1\%$ ) of valence compensated additions and donor dopants and hence, different Curie temperatures  $190^\circ\text{C} < T_c < 350^\circ\text{C}$  and different weak-signal dielectric and piezoelectric coefficients) was investigated.<sup>5</sup> The measuring field was applied both parallel ( $E_3$ ) and perpendicular ( $E_1$ ) to the poling direction of the

ceramic in order to investigate the influence of different symmetry conditions (i.e., different orientations to the poling axis).

Measurements were carried out at room temperature. In all the data presented, the amplitude  $E_{ac}$  of the applied ac-field was well below the depoling field of the material. The field-induced strain  $S$  and the dielectric displacement  $D$  were measured by a displacement sensor (MTI 2000) and a Sawyer-Tower circuit,<sup>6</sup> respectively, under stress-free (non-resonant) conditions at a frequency  $f = 100$  Hz. The output signals were analyzed using a digital oscilloscope and, in addition, by lock-in amplifiers to obtain their first harmonic components  $S^{(1f)}$  and  $D^{(1f)}$ . The effective dielectric ( $K_{33}$  and  $K_{11}$ ) and piezoelectric ( $d_{33}$  and  $d_{15}$ ) coefficients were determined by  $K = D^{(1f)}/\epsilon_0 E_{ac}$  and  $d = S^{(1f)}/E_{ac}$ , respectively. At weak fields ( $E < 50$  V/cm), because of the sensitivity limitation of the displacement sensor, only the dielectric constant was measured using a General Radio 1616 precision capacitance bridge.

A typical experimental result of the nonlinearity of the dielectric and piezoelectric coefficients is presented in Fig. 1(a). Both the dielectric and piezoelectric coefficients can be described by Eq. (1) [Fig. 1(b)] which supports the hypothesis of a finite threshold for domain wall motion in soft PZT.<sup>3-5</sup> The threshold field for the PZT examined is at  $E_{c1} = 100 \pm 50$  V/cm, consistent with early results. However, it is found that the effective exponent  $\phi = 1.2 \pm 0.1$  for the data perpendicular to the poling direction ( $K_{11}$  and  $d_{15}$ ) is quite different from  $\phi = 1.0 \pm 0.1$  for the data parallel to the poling direction ( $K_{33}$  and  $d_{33}$ ).

In order to understand the significance of the result, one can compare it with the expressions expected from the Taylor expansion in which  $y(E_1)$  and  $z(E_3)$  are expanded in terms of  $E_1$  and  $E_3$ , respectively. Here  $z$  stands for  $K_{33}$  and  $d_{33}$  and  $y$  represents  $K_{11}$  and  $d_{15}$ , respectively. From the symmetry consideration, the Taylor expansions of the two coefficients  $y(E_1)$  and  $z(E_3)$  are different:

<sup>a)</sup> Present address: FB Physik, Universität Halle, E.-Bach-Platz 6, D-06108 Halle, Germany.

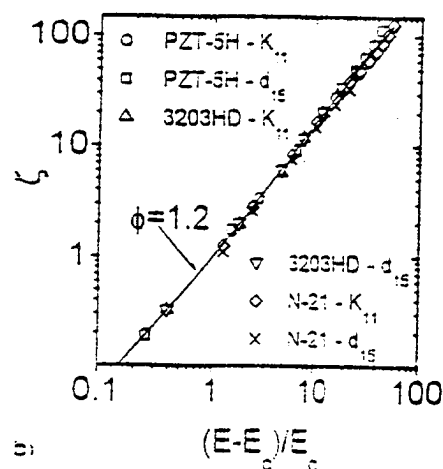
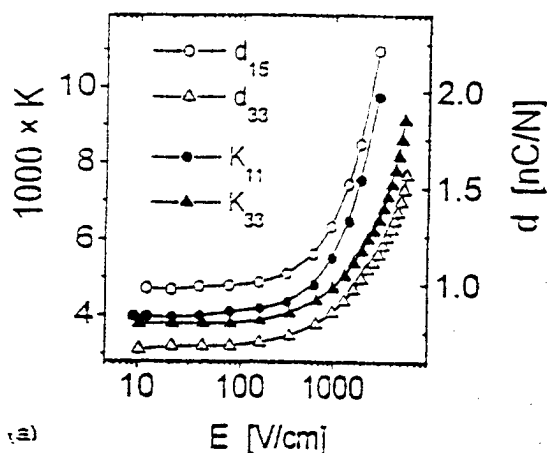


FIG. 1. (a) The nonlinear dielectric and piezoelectric response of Motorola 3203HD. (b) Scaling plot of  $\zeta = [(\epsilon(E) - \epsilon_0)/A]$  [see Eq. (1)] vs reduced field for the piezoceramics investigated. The quantity was evaluated above threshold  $E_{c1} = 100$  V/cm from both dielectric and piezoelectric data obtained perpendicular to the poing direction. The quoted exponent refers to the straight line shown in the figure.

$$\epsilon(E) = \epsilon_0 + \epsilon_{nl} = \epsilon_0 + \frac{\epsilon_1}{2} E^2 + \frac{\epsilon_2}{4} E^4 + \dots \quad (2)$$

In the expansions higher order terms are neglected. The effective exponent  $\phi = 1.0 \pm 0.1$  for  $K_{33}$  and  $d_{33}$  has been reported and is consistent with Eq. (2).<sup>6</sup> However,  $\phi = 1.2 \pm 0.1$  for  $K_{11}$  and  $d_{15}$  is apparently much smaller than  $\phi = 2$  as expected from Eq. (2) (the exponent of  $E^2$  term). To ensure that the exponents do not depend on frequency, measurement was also made at lower frequencies.

It should be pointed out that the weak field dielectric and piezoelectric coefficients and the Curie temperatures of the PZT ceramics investigated differ significantly, indicating the crucial role played by the amount and type of the dopants added.<sup>7</sup> However, for a given direction of the field, the scaling of data obtained on different ceramics yields the same value of the scaling exponent which moreover does not depend on whether it is the dielectric or piezoelectric data that are analyzed. In view of the different behavior of acceptor-doped PZT,<sup>7</sup> the results here suggest a universal behavior

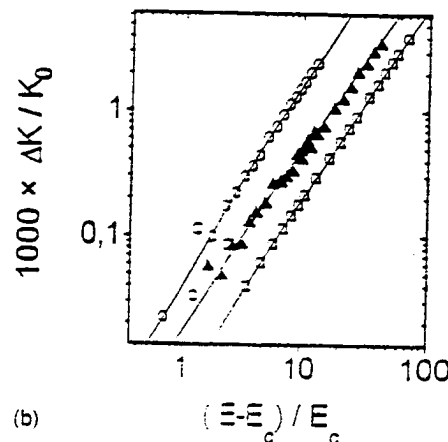
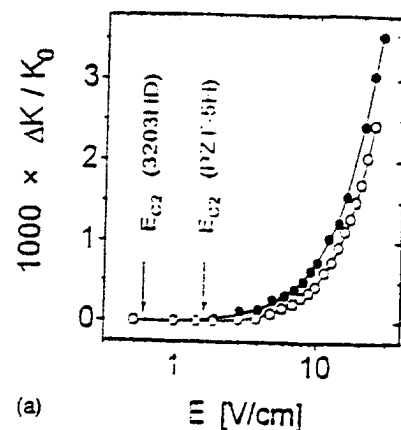


FIG. 2. (a) The ac-field dependence of the reversible excess part  $\Delta K/K_0$  of the dielectric constant (see text for details) around weak field threshold  $E_{c2}$ . The data were evaluated from the dielectric coefficient  $K_{33}$  obtained on Motorola 3203HD and  $K_{11}$  obtained on PZT-5H, respectively. The lines represent least square fits of the experimental data above threshold according to Eq. (1). (b) Scaling plot of  $\Delta K/K_0$  vs reduced field above weak field threshold  $E_{c2}$ . The quantities were evaluated from  $K_{33}$  Motorola 3203HD (open circles) and  $K_{11}$  from PZT-5H (open squares) and Tokin N-2 (triangles), respectively. The lines represent least square fits of the linear part of the curves.

related to the donor doping in soft PZT piezoceramics and provide a convenient way of describing the nonlinearity in these materials.

Moreover, in small fields  $E < E_{c1}$ , a weak but significant ac-field dependence of the dielectric constant is observed in both directions of the external field. In this field range, however, besides the reversible increase of dielectric constant with ac field, similar to those observed in strong fields, the sample properties are changed irreversibly due to the ac field which is related to a deaging effect. Therefore, in order to determine the reversible nonlinear effect, the change due to the deaging should be subtracted from the data. That is, the difference  $\Delta K(E_{ac}) = K(E_{ac}) - K(E_0)$  should be considered. Here,  $K(E_m)$  is the dielectric constant measured at a given field  $E_m$ , which has both the nonlinear and the deaging effect.  $K(E_0)$  is the dielectric constant determined immediately after the measurement at  $E_m$  is completed and measured with a small field  $E_0 \leq 0.4$  V/cm (below the threshold) which probes the change in the dielectric constant due to deaging. Although these two effects (nonlinear and deaging effect) in weak fields have the same order of magnitude, it is found that the difference is independent of the particular aging state of the ceramic (i.e., how the measurement is conducted) and

reproducible. The resulting function  $\Delta K(E_{ac})$  increases monotonically with  $E_{ac}$  [Fig. 2(a)]. In addition, it can be scaled according to Eq. (1) for both directions of the external field [Fig. 2(b)], i.e., the ac-field dependence in weak fields is analogous to that observed in large fields.

For the materials investigated, the threshold values are in the range  $0.4 \text{ V/cm} < E_{c2} < 2 \text{ V/cm}$  and seem to be associated with  $K_0$ , the linear dielectric constant of the ceramics, i.e., a material with a higher  $K_0$  has a lower  $E_{c2}$ .<sup>7</sup> The effective scaling exponent  $\phi$ , on the other hand, shows no significant dependence on the material. More interestingly, we find for both directions of the external field the value  $\phi = 1.5 \pm 0.1$ . By analogy with the results in the large field region, this result indicates that both  $K_{11}$  and  $K_{33}$  are nonanalytic functions of  $E_1$  and  $E_3$  and cannot be expanded using the simple Taylor expansion given in Eq. (2).

There are several works dealing with the nonlinear behavior related to interface motion. In one of the works, the anharmonic potential energy  $U(\Delta x)$  of the wall displaced by a distance  $\Delta x$  from the equilibrium position is believed to cause the nonlinear domain wall response.<sup>8</sup> However, any nonlinearity attributed to the potential energy of the wall has to meet the symmetry conditions and is therefore qualitatively inconsistent with the experimentally observed nonanalytic scaling behavior.

On the other hand, the field-driven ferroelectric domain wall represents an elastic interface with many degrees of freedom moving through a pinning medium with quenched disorder corresponding to the distribution of immobile defects. Theoretical models treating the depinning transition of such an interface as a dynamical critical phenomenon predict a scaling behavior similar to Eq. (1) between force and velocity above the onset of interface motion.<sup>9,10</sup>

It should be pointed out that experimental data obtained for a PZT piezoceramic is an average response over all

grains, different domain walls with different orientations to the external field. We are also aware that our experiments may not probe the critical region of a probable depinning transition in soft PZT. Therefore, the effective exponents describing the nonanalytic scaling behavior of the piezoceramics may not be mistaken with critical exponents of the theoretical models. Thus it is surprising that the value  $\phi = 1.5 \pm 0.1$  found experimentally in weak fields agrees well with the theoretical mean-field exponent  $\phi = 3/2$ .<sup>9</sup> Moreover, an effective exponent  $\phi = 1.45 \pm 0.03$  was determined recently for (nonferroelastic)  $180^\circ$  domain walls in improper ferroelectric lock-in phases.<sup>11</sup> Apparently, the dynamics of domain walls leads to a similar nonanalytic scaling in very different ferroelectric systems for which there seems to be no explanation at present.

The authors are grateful to Jayanth Banavar for stimulating discussions.

<sup>1</sup>L. E. Cross, *Ferroelectric Ceramics: Tailoring Properties for Specific Applications in Ferroelectric Ceramics*, edited by N. Setter and E. L. Colla (Birkhauser, Basel, 1993).

<sup>2</sup>M. E. Lines and A. M. Glass, *Principles and Applications of Ferroelectrics and Related Materials* (Clarendon, Oxford, 1977).

<sup>3</sup>Q. M. Zhang, W. Y. Pan, S. J. Jang, and L. E. Cross, *J. Appl. Phys.* **64**, 6115 (1988).

<sup>4</sup>Y. Saito, *Jpn. J. Appl. Phys. Part 1* **34**, 5313 (1995).

<sup>5</sup>We studied PZT 3203HD from Metcra Inc., NM, USA, PZT N-21 from Tokin Inc., Japan, and PZT-5H from Morgan-Matroc Inc., OH, USA. All are PZT-ceramics with different levels of donor doping. Results from other soft PZTs are consistent with those presented.

<sup>6</sup>D. Damjanovic and M. Demartin, *J. Phys. D* **29**, 2057 (1996).

<sup>7</sup>V. Mueller and Q. M. Zhang, *J. Appl. Phys.* **83**, 3754 (1998).

<sup>8</sup>S. Li, W. Cao, and L. E. Cross, *J. Appl. Phys.* **69**, 7219 (1991).

<sup>9</sup>D. S. Fisher, *Phys. Rev. B* **31**, 1396 (1985).

<sup>10</sup>P. B. Littlewood, in *Charge Density Waves in Solids*, edited by L. P. Gor'kov and G. Gruner (Elsevier, Amsterdam, 1989).

<sup>11</sup>T. Hauke, V. Mueller, H. Beige, and J. Fousek, *J. Appl. Phys.* **79**, 7958 (1996).

# **APPENDIX 16**

# Field Induced Acoustic Emission (AE) in Ferroelectric Ceramics

Kenji Uchino and Hideaki Aburatani

International Center for Actuators and Transducers (ICAT),  
Intercollege Materials Research Laboratory, The Pennsylvania State University,  
University Park, PA 16802, USA

**Abstract** -- Electric field induced acoustic emission (AE) in ferroelectric PZT ceramics has been studied. It was shown that the field induced AE originated from where the displacement was induced and ended when the applied field was being reduced during poling. A larger electric field than the previously applied maximum field was required for new AE generation (Kaiser effect). From the AE event rate and the AE signal amplitude distribution, it was assumed that there were two origins of the bipolar field induced AE in the ferroelectric ceramics: deformation related to domain reorientation and piezoelectric deformation without domain reorientation.

## §1. Introduction

In ferroelectric materials, the AE method has been used to determine phase change,<sup>1-3)</sup> to detect domain reorientation<sup>4-6)</sup> and to monitor crack propagation.<sup>7-9)</sup> It has been believed that ferroelectric domain motion is a dominant AE source in the ferroelectrics. However, our recent research has shown a significant measurement problem in the most of previous field induced AE studies.<sup>10)</sup> A mechanical vibration of sample is easily excited by an electrical coupling between the power supply feedback and the piezoelectricity of sample, resulting in a vibro-acoustic emission. The vibro-acoustic emission could vary with electric field, and was similar to the reported field induced AE results. The sample vibration could be eliminated by increasing the time constant  $\tau$  of the voltage (field) application system. It was shown that this modified voltage (field) application method makes the field induced AE measurements at high sensitivities possible without vibro-acoustic emissions. Considerably different AE results from the reported field induced AE were obtained using the modified method. The AE appeared to be observed from where the displacement was induced during poling. New AE will not be generated after sufficient poling.

This paper deals with the electric field induced AE generations in a ferroelectric lead zirconate

titanate  $\text{Pb}(\text{Zr}_{x}\text{Ti}_{1-x})\text{O}_3$  (PZT) ceramics. The field induced AE activities were analyzed by comparing them with obtained induced displacement. A fractal dimension analysis of the AE signal amplitude distribution was also applied.

## §2. Experimental Setup

Figure 1 shows the field induced AE and displacement measurement system. The sample was placed on the AE sensor (NF Corporation, AE-904E) with its resonant frequency of 450 kHz. The induced displacement was also observed using a L.V.D.T (Millitoron, Nr. 1301). The AE signal was amplified by 40 dB through a low noise pre-amplifier (NF Corporation, AE-9913) and again up to 60 dB with a main amplifier (NF Corporation, AE-922). The amplified AE signals were counted after passing through a high-pass filter ( $f > 100$  kHz) and a discriminator.

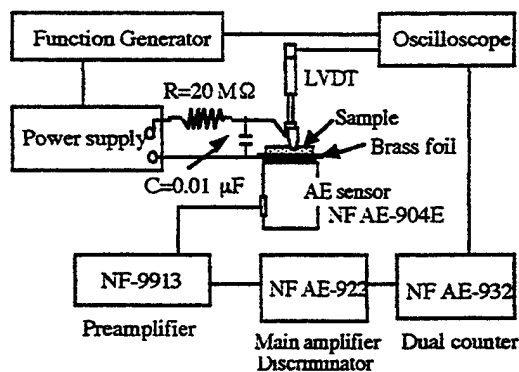


Figure 1 Field induced AE and displacement measurement system.

Disc specimens of commercialized ferroelectric lead zirconate titanate PZT ceramic (Morgan Matroc, PZT-5A) with 12.7 mm in diameter and 0.4 mm in thickness were employed for this study. Gold electrodes were

formed on both surfaces by sputtering. The AE sensor was attached to the sample through brass-foil with 0.025 mm in thickness. A silicone grease was used as a couplant to make a better acoustical contact. An external resistor  $R$  ( $R = 20 \text{ M}\Omega$ ) and a capacitor  $C$  ( $C = 0.01 \text{ }\mu\text{F}$ ) were installed to the power supply in order to eliminate the vibro-acoustic emission.

### §3. Results and Discussions

#### 3.1 The Kaiser Effect in Field Induced AE

Figure 2 shows the AE event, induced displacement and applied electric field as a function of time for a cyclic application of various electric fields. The threshold level of the AE signal were set to be 400 mV at 100 dB. An unpoled sample was employed for this measurement. At the first cycle (poling), an electric field of 20 kV/cm was applied to the sample. The amplitude of the field was increased to be 25 kV/cm at the second cycle, and again up to 30 kV/cm at the third cycle.

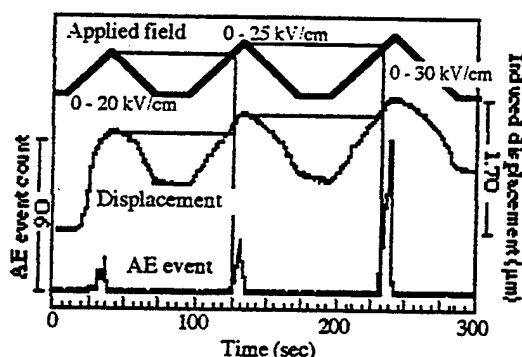


Figure 2 The AE event, induced displacement and applied electric field as a function of time for a cyclic application of various electric fields.

The sample was poled at the first cycle. The induced displacement and total residual displacement observed as a zero point shift increased with amplitude of applied field, because the higher degree of poling is achieved by the applications of the larger electric fields. At first cycle, the AE event occurred from where the displacement was induced and increased with field. The AE was not generated during the field was being reduced. In the second cycle, no AE events were observed until the electric field reached  $E = 20 \text{ kV/cm}$ . New AE generation was observed above  $E = 20 \text{ kV/cm}$ , and increased with the electric field. In the third cycle, this AE

onset field again shifted to be  $E = 25 \text{ kV/cm}$ . The AE was generated only when the applied field exceeded the previous maximum value. This pre-applied electric field (induced displacement) dependence of the AE generation implies a Kaiser effect in the electric field induced deformation of the PZT ceramics.

The domain motion has been believed to be origin of the field induced AE. However, it is shown that all domain motions can not be the origin of the field induced AE, because the field induced AE depends on the pre-applied electric field (Kaiser effect). Therefore, particular domain reorientation processes rather than domain motion should be considered to be the origins of the AE. Another possible AE source is a mechanical stress, since the mechanical stress is supposed to be induced in the sample at high strain (electric field) state.

#### 3.2 The Electric Field Induced AE

Figure 3 shows the AE event count rate and the induced displacement as a function of applied field at 0.0015 Hz with field of  $E = \pm 35 \text{ kV/cm}$ . The AE measurement conditions were set to be at 100 dB with a threshold level of 400 mV. A butterfly shape induced displacement due to the domain reorientation was obtained. The critical electric field, where the AE started to be generated, corresponded to the point of inflection of the displacement with respect to the field. (In Fig 3,  $d(\text{displacement})/dE$  is shown for the point of inflection.)

The maximum of AE event count rate was not observed at the maximum applied field. The maximum AE event rate was found to be around  $E = 27 \text{ kV/cm}$ . Considering that internal stress increases with the applied field in the ferroelectrics, this decrease in the AE event rate might imply that the internal stress could be the origin of the AE, but not only one source. The induced displacement in the ferroelectric ceramics consists of the deformation related to domain reorientation and piezoelectric deformation without the domain reorientation. Therefore, it was supposed that the field induced AE under bipolar electric fields in the PZT ceramics was generated first through deformation related to domain reorientation. After the domain reorientation was completed, the piezoelectric deformation unrelated to domain reorientation, which accompanied with the induced internal stress, was expected to be the origin of the AE. The decrease in the AE event rate might indicate the completion of the domain reorientation related deformation.

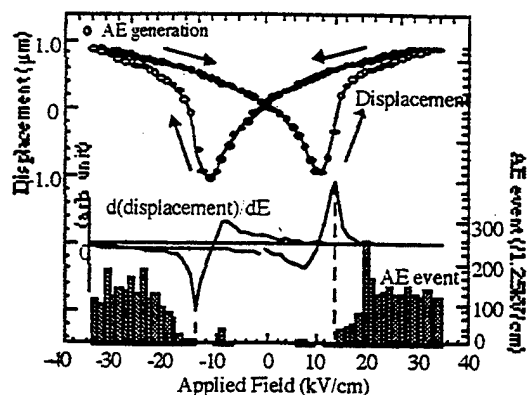


Figure 3 AE event count and the induced displacement as a function of applied field.

### 3.3 The Fractal Dimension of the Electric Field Induced AE

When the AE event rate  $f(x)$  is the minus  $m$ -th power of  $x$ , where  $x$  is the AE signal amplitude,

$$f(x) = cx^{-m} \quad (c: \text{constant}). \quad (1)$$

The number of  $m$  is defined as a fractal dimension.<sup>11)</sup> The fractal dimension  $m$  is used to estimate the damage in the materials.

The integrated AE event  $F(x)$ ,

$$F(x) = \int_x^\infty f(x) \cdot dx = \frac{1}{m-1} cx^{-(m-1)} \quad (m > 1) \quad (2)$$

was observed through changing the AE signal threshold level in the measurements.

Figure 4 shows the AE event count per cycle as a function of the AE signal threshold level. The observed AE event count logarithmically decreased with the AE signal threshold level when a field of  $E = \pm 25$  kV/cm was applied. Thus, a fractal dimension of  $m=1$

( $\frac{d}{dx}[c \log x + A] = cx^{-1}$ ) was obtained for the logarithmic decrease. In general, the fractal dimension is found to be more than 2 for the AE generated from the plastic deformation. The fractal dimension of  $m = 2$  is a critical number to evaluate the condition of materials. If there is a damage (i.e., crack) in the material, the fractal dimension becomes lower than 2. From this concept of the fractal dimension, the obtained dimension indicated that the sample had been

damaged. However, it is supposed that the lowered fractal dimension was due to the existence of ferroelectric domain and the effect of the deformation related to domain reorientation, instead of the crack in the material, since repeatable and stable field induced AE events were observed.<sup>12)</sup>

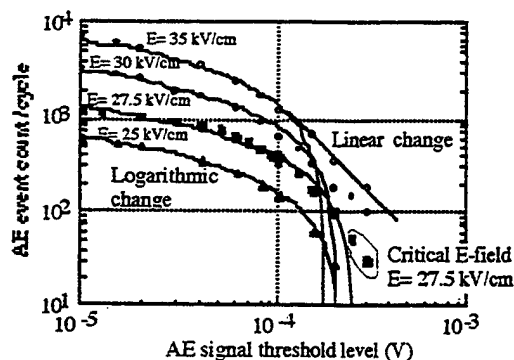


Figure 4 AE event count per cycle as a function of the AE signal threshold level for various bipolar electric field amplitudes.

When the amplitude of electric field was increased, the higher AE signal threshold level parts did not follow to the logarithmic change. A critical amplitude of the electric field, above which non-logarithmic AE distributions were observed, was found to be around  $E = 27$  kV/cm. The lower signal threshold level region still could be fitted to a logarithmic curve and the extended line also ended around the AE signal threshold level obtained for  $\pm 25$  kV/cm. The higher AE signal threshold level parts ( $>10^{-4}$  mV) showed a linear decrease with the threshold level. When an electric field of  $E = \pm 35$  kV/cm was applied, a fractal dimension of  $m = 2.8$  was obtained. Figure 5 shows the induced displacement under unipolar and bipolar fields. Although the butterfly shape induced displacement for the bipolar field is due to the domain reorientation, the bipolar field induced displacement coincided with the unipolar field induced displacement above the electric field  $E = 27$  kV/cm. Thus, it is assumed that the domain reorientation was completed at higher electric fields than the critical electric field  $E = 27$  kV/cm. The origin of the AE with the fractal dimension of 2.8 was assumed not to be the deformation related to domain reorientation, but the piezoelectric deformation without domain reorientation.

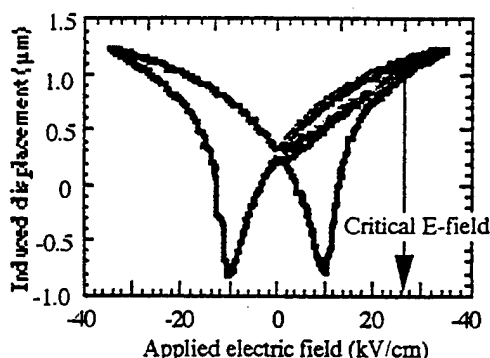


Figure 5 Field induced displacement under unipolar and bipolar fields.

It was shown that the fractal dimension of the field induced AE for the deformation related to domain reorientation ( $m = 1$ ) was lower than that for the piezoelectric deformation without domain reorientation ( $m = 2.8$ ). The fractal dimension greater than two corresponded to the plastic deformation. However, it was difficult to categorize the electrically induced deformation of ferroelectric ceramics as the plastic deformation, because the induced displacement recovers to the initial state after removing the field. Hence, it should be noted that the AE generation process in the ferroelectric ceramics could be different from that of reported AE in the materials such as metals and structural ceramics.

#### §4. Conclusion

The electric field induced acoustic emissions (AE) in the ferroelectric PZT ceramics were studied. It is shown that the Kaiser effect in terms of applied electric field (displacement) took place in the electric field induced deformation of ferroelectric PZT ceramics. The AE event rate as a function of applied field and AE signal threshold level distribution were employed to identify the origin of field induced AE. The AE event rate in ferroelectric PZT showed two origins: deformation related to

domain reorientation and piezoelectric deformation without domain reorientation. It is assumed that the fractal dimension of the ferroelectric PZT ceramics consisted of the domain reorientation related  $m = 1$  and the domain reorientation unrelated  $m = 2.8$ . A critical bipolar electric field for the domain reorientation unrelated AE generation was found to be  $E = 27$  kV/cm.

#### Acknowledgment

This work was partially supported by the Office of Naval Research through Contract No. N00014-92-J-1510

#### References

- 1) P. Buchman: Solid State Electronics. **15** (1972) 142.
- 2) I. J. Mohamad, E. F. Lambson, A. J. Miller and G. A. Saunders: Phys. Lett. **A 71** (1979) 115.
- 3) V. A. Kalitenko, V. M. Perga and I. N. Salivonov: Sov. Phys. Solid State **22** (1980) 1067.
- 4) H. Iwasaki and M. Izumi: Ferroelectrics **37** (1981) 563.
- 5) Y. Saito and S. Hori: Jpn. J. Appl. Phys **33** (1994) 5555.
- 6) W. Pan, H. Cao: Ferroelectrics, **129** (1992) 119.
- 7) D. G. Choi and S. K. Choi: J. Mat. Sci., **32** (1997) 421.
- 8) E. C. Subbarao, V. Srikanth, W. Cao, L. E. Cross: Ferroelectrics **145** (1993) 271.
- 9) H. Aburatani, S. Harada, K. Uchino, A. Furuta and Y. Fuda: Jpn. J. Appl. Phys. **33** (1994) 3091.
- 10) H. Aburatani and K. Uchino, Jpn. J. Appl. Phys. **35** (1996) L516.
- 11) H. Nakasa: *Theoretical Bases and Applications of Acoustic Emission*, (Chijin Shokan Co. Ltd., Tokyo, 1994) 1st ed. (in Japanese).
- 12) H. Aburatani, J. P. Witham and K. Uchino, Jpn. J. Appl. Phys. **37** (1998) 602.

# **APPENDIX 17**

## SIZE EFFECTS IN FERROICS

R. E. NEWNHAM\* and S. TROLIER-McKINSTRY

*Intercollege Materials Research Laboratory, The Pennsylvania State University,  
University Park, PA 16802, USA*

*(Received 25 September 1996; In final form 17 December 1996)*

Ferroic crystals have domain walls which can be moved by electric field (ferroelectrics), magnetic fields (ferromagnets), mechanical stress (ferroelastics) or a higher order phenomenon involving a combination of the three (secondary ferroics). Because of the large contribution movable domain walls make to piezoelectricity, permittivity, permeability, and to elastic compliance, these materials are used as transducers, capacitors, transformers, sensors and actuators. A basic understanding of size effects is critical to the development of these devices, which are being made in smaller and smaller sizes in the form of thin films, fiber-filled composites, and multilayer ceramics with submicron grain sizes.

Four regimes are observed when the particle size is made smaller: (1) crystals or large grains in ceramics contain *many domain* walls, but the number of walls, and the number of types of walls, grows smaller as grain size is reduced. (2) When the size is decreased sufficiently, the particles become single domain. The properties of *single domain* particles are quite different from those of multi-domain particles. (3) At yet smaller grain size, the particles exhibit *diffuse phase transformations*, nonlinear physical properties, and glass-like behavior. (4) The fourth regime is in the nanometer range where ferroic behavior disappears as surface effects begin to dominate.

*Keywords:*

### INTRODUCTION

Many phase transitions exhibit size effects. The melting point of bulk gold, for example is 1337 K, but this temperature drops rapidly for grain sizes below 100 Å (Fig. 1). This decrease in the phase transition temperature has been attributed to the change in the ratio of surface

---

\* Corresponding author,

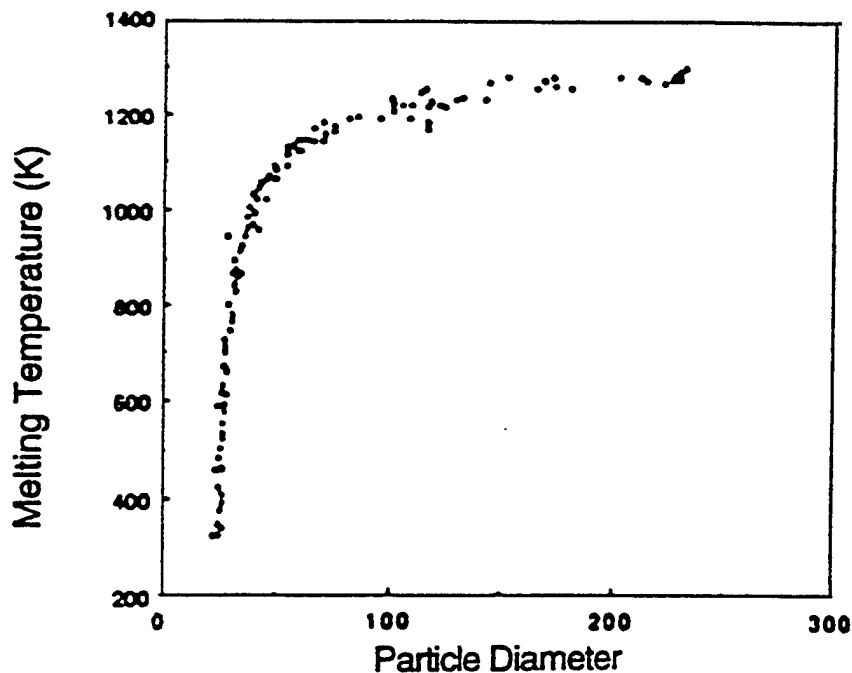


FIGURE 1 Melting temperature of gold particles as a function of size. Taken from Ref. [1].

energy to volume energy as a function of particle size. <sup>[1]</sup> Thus, for spherical particles of radius  $r$ , the melting temperature can be predicted from

$$\Delta U dV - \Delta S T_m dV - \sigma dA = 0. \quad (1)$$

where  $\Delta U$  and  $\Delta S$  are the changes in internal energy and entropy on melting,  $\sigma$  is the interfacial energy between the liquid and the solid, and  $T_m$  is the melting temperature of the particle. If  $\Delta S$  and  $\Delta U$  are temperature independent, then the difference between the bulk and small-particle melting temperatures is inversely proportional to the particle radius according to

$$\frac{T_o - T_m}{T_o} = \frac{2\sigma}{\rho L r} \quad (2)$$

where  $L$  is the heat of fusion,  $\rho$  the density, and  $T_o$  the bulk melting point. Many other equilibrium phase transitions display comparable size effects. In addition to the data on gold particles, the melting temperatures of copper, tin, indium, lead, and bismuth particles and thin films have all been shown to be size dependent. <sup>[2]</sup> Similarly, the

superconducting transition depends on size both intrinsically <sup>[3]</sup> and extrinsically, if the stress exerted on the superconducting phase is different at different sizes. Superfluid transitions in He-impregnated powder compacts and thin films also depend on either the film thickness or the size of the pore diameter. <sup>[4]</sup>

In ferroic materials, both the presence of domain walls and the ferroic transition itself are influenced by crystallite size. While this has not previously been critical to most applications, with the growing importance of thin-film- and small-particle-based devices, it is becoming important to understand the size effects expected in ferroic materials..

## FERROIC SOLIDS

Ferroic crystals have moveable domain walls which impart useful properties to a number of ceramics and metals. The useful properties of these materials are anomalously enhanced near the phase transformation temperature, where the ferroic domain structure is destabilized as the crystalline structure alters to a high-temperature, high-symmetry form. It is for this reason that the dielectric permittivity of ferroelectric capacitors is the largest near the Curie temperature, and the magnetic susceptibility of ferrite transformers peaks near  $T_c$ . Ferroic crystals can be classified into primary and secondary species according to the driving forces required to move domain walls and generate hysteretic behavior (Tab. I). Ferroelastic solids have orientation states or domains which differ in spontaneous strain. The domain walls separating these domains can be shifted with mechanical stress, leading to hysteresis between stress and strain. Analogous behavior between polarization and electric field is observed in ferroelectric crystals, and between magnetization and magnetic field in ferromagnetic materials.

In addition to the three types of primary ferroics, there are six types of secondaries which also have mobile domain walls. Some, like ferromagnetoelectric chromium oxide, require that two fields (E and H) be applied simultaneously, while others such as ferrobielastic quartz, are higher order primary effects in which the energy difference between domain states is proportional to the square of the applied stress.

TABLE 1 Primary and secondary ferroic crystals are classified by the differences in property coefficients for various orientation states. Domain walls can be driven by electric fields (E), magnetic fields (H), or mechanical stresses ( $\sigma$ )

	<i>Domain states difference</i>	<i>Driving force</i>	<i>Example</i>
Primary Ferroics			
Ferrimagnetism	Spontaneous Magnetization	H	Iron (Fe)
Ferroelectricity	Spontaneous Polarization	E	Barium Titanate BaTiO <sub>3</sub>
Ferroelasticity	Spontaneous Strain	$\sigma$	Zirconia ZrO <sub>2</sub>
Secondary Ferroics			
Ferroelastolectricity	Piezoelectric Coefficient	E $\sigma$	Ammonium Chloride NH <sub>4</sub> Cl
Ferromagnetoelasticity	Magnetoelectric Coefficient	EH	Chromium Oxide (Cr <sub>2</sub> O <sub>3</sub> )
Ferromagnetoelctric	Piezomagnetic Coefficient	H $\sigma$	Iron Carbonate (FeCO <sub>3</sub> )
Ferrobiclasticity	Elastic Compliance	$\sigma^2$	Quartz (SiO <sub>2</sub> )
Ferrobimagnetism	Magnetic Susceptibility	H <sup>2</sup>	Nickel Oxide (NiO)
Ferrobielectricity	Electric Permittivity	E <sup>2</sup>	Strontium Titanate (SrTiO <sub>3</sub> )

The study of single-phase and composite ferroics has resulted in several new families of devices with superior properties. Typically, the success of such composites can be traced to well-designed phase connectivity patterns, which can, for example, force desirable field concentrations in a single phase, enhance the anisotropy of property coefficients, and control the transport of heat or charge. Engineering of this type accounts for the rapid growth in composite biomedical transducers, thermistors, hydrophones, and chemical sensors. Research and development programs on thin-film ferroelectric memories, and on miniature sensors and actuators for "smart" systems are especially active at present.

However, the drive towards small-scale components has resulted in a new generation of devices in which not only the design, but the scale of the components also plays a remarkable role in the overall properties. This is especially important in the case of ferroic materials, where both the presence of domain walls and indeed, the ferroic transition itself, is controlled by the crystallite size. In order to predict what properties to expect from nanoscale ferroics, it is necessary to understand how factors like particle size, dimensionality, boundary conditions, and the origin of the phase transition affect size effects in ferroics.

It is anticipated that ferroic materials will undergo four changes in the phase transformations as the particle size is reduced (Fig. 2). While ferromagnetic materials are still by far the best studied, new experimental evidence is accumulating that small ferroelastic, ferroelectric and secondary ferroic particles will show similar behavior.

When prepared as large grain size, ceramics (typically microns or larger), ferroelectric and ferromagnetic oxides exhibit complex domain structures, often with several types of domain walls. As the grain size is reduced, however, the surface area grows in comparison with volume and it becomes increasingly difficult to recover the wall energy from the volume term. Consequently, the number of domains decreases as first one and then the other types of walls are eliminated. The transition from polydomain to single domain behavior is well-documented in a number of ferromagnets, occurring near 30 nm for many spherical metallic particles. For example, pure iron suspended in mercury shows a critical size for conversion to single domain behavior at ~23 nm and  $\text{Fe}_{0.4}\text{Co}_{0.6}$  a critical size of ~28 nm.<sup>[5]</sup> This is in good


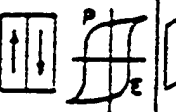
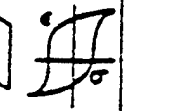



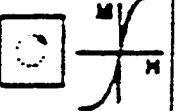
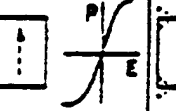
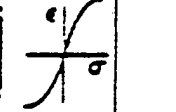
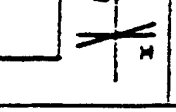
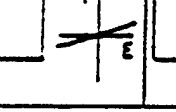
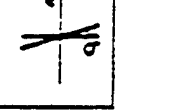
SIZE	FERROMAGNETIC	FERROELECTRIC	FERROELASTIC
$\sim 1 \mu\text{m}$ $10^3 \text{ nm}$	MULTIDOMAIN 	MULTIDOMAIN 	MULTIDOMAIN 
$\sim 0.1 \mu\text{m}$ $10^2 \text{ nm}$	SINGLE DOMAIN 	SINGLE DOMAIN 	SINGLE DOMAIN 
$\sim 10 \text{ nm}$ $\sim 10^1 \text{ \AA}$	SUPER-PARAMAGNETIC 	SUPER-PARAELECTRIC 	SUPER-PARAELASTIC 
$\sim 1 \text{ nm}$ $\sim 10^0 \text{ \AA}$	PARAMAGNETIC 	PARAELECTRIC 	PARAELASTIC 

FIGURE 2 Transitions in ferroic behavior as a function of size.

agreement with calculations by Kittel, who suggested a 20 nm minimum size for the appearance of ferromagnetism in particles. [6] Results for acicular agglomerates of  $\gamma\text{-Fe}_2\text{O}_3$  particles separated by non-magnetic grain boundaries are also consistent with these estimates: Berkowitz *et al.* [7] report that the stable single domain range at room temperature is centered at  $\sim 40$  nm.

Studies on  $\text{BaTiO}_3$  ceramics (which contain ferroelectric  $180^\circ$  walls and  $90^\circ$  walls which are both ferroelectric and ferroelastic) also show fewer  $90^\circ$  domains in small-grained samples than are observed for large grain sizes. An intermediate regime, centered at a grain size of  $0.7 \mu\text{m}$ , with an increased density of small  $90^\circ$  domains has also been reported by Arlt *et al.* [8] Explanation for the changes in the equilibrium number of domains as a function of grain size (and in particular, the effect of this on the dielectric properties) is complicated by the fact that in a ceramic where individual grains do not possess cubic symmetry, each grain is subjected to a complex set of stresses which arise when the body is cooled through the transition

temperature after firing. Because  $90^\circ$  walls are ferroelastic as well as ferroelectric, large stresses should be expected to greatly affect the number and type of domains. We observed similar behavior in lead zirconate titanate (PZT) ceramics, where a strong correlation between domain size and grain size leads to changes in elasto-dielectric properties.

For isolated  $\text{BaTiO}_3$  particles, though, the boundary conditions on each particle are much simpler than those existing in a polycrystalline ceramic. However, critical sizes for the disappearance of  $90^\circ$  domains and the transition to single domain in unconstrained ferroelectric powders have not been well established.

Although the loss of multidomain behavior in ferroelectric ceramics is known to occur for much larger grain sizes (approximately several tenths of a micrometer), it is also clear that the stress state in a monolithic body containing domains is considerably more complex than that for isolated particles. Consequently, the changes in ferroic properties as a function of size in ferroelectric powders are expected to follow the ferromagnetic analog more closely. This is born out in experiments on 0–3  $\text{PbTiO}_3$  polymer composites in which the filler particle size was varied. Lee *et al.* [9] reported that there is a significant drop in the ability to pole such composites for filler particles smaller than  $\sim 200$  nm. Assuming both that the small particles were well crystallized and that the particle size distribution were narrow, this implies that transition from multidomain to single domain occurs in  $\text{PbTiO}_3$  particles near 200 nm.

At still smaller sizes, ferroic particles undergo a phase change to the high temperature symmetry group and sometimes show the enhanced responsiveness of a superparamagnetic or superparaelectric solid. This state is characterized by zero spontaneous polarization, the disappearance of hysteresis and large electric permittivity. Pure  $\text{BaTiO}_3$  may not show the enhanced permittivity as the particle size is decreased, but certain modified barium titanates do. The transition from the single domain state to the high temperature symmetry may also be related to decrease in the Curie Temperature  $T_c$ . Previous reports have shown that the critical sizes at which the Curie Temperature drops below room temperature are  $\sim 80$ – $120$  nm for  $\text{BaTiO}_3$  [10] and  $\sim 20$  nm for  $\text{PbTiO}_3$ . [11] While  $\text{BaTiO}_3$  is the best studied ferroelectric system, it is clear that many of the observed size effects depend sensitively on the

material preparation conditions, and on the electrical and elastic boundary conditions of the sample. Consequently, the critical size for the ordinary paraelectric to superparaelectric transition is unknown. Because it is difficult to characterize the electrical properties of such small particles, it is not known if and when the high-symmetry particles actually become superparaelectric. On the other hand,  $\text{NaNO}_2$  shows only some broadening in the differential thermal analysis (DTA) characteristic for the ferroelectric phase transition with no change in the transition temperature for particle sizes down to 5 nm. While it is an order-disorder ferroelectric, and so might have different size dependence for the properties than would a displacive ferroelectric, it is interesting that there is no evidence for superparaelectricity even at particle sizes of 5 nm.

Other ferroic materials also undergo a phase change to the high-temperature prototype group at small sizes. In the case of ferromagnetic particles, this has been correlated with the size at which the decrease in volume free energy accompanying magnetization is on the order of the thermal energy. As a result, the spin direction is randomized with time, leading to an unmagnetized but highly orientable single-domain crystal. Thus, a magnet in this size regime is characterized by a zero net magnetization, the disappearance of a magnetic hysteresis loop, extremely high magnetic susceptibilities, and a symmetry that, on average, is higher than that of the ferromagnetic phase. Iron exhibits superparamagnetic behavior at particle sizes near 7 nm, <sup>[12]</sup>  $\gamma\text{-Fe}_2\text{O}_3$  at  $\sim 30$  nm <sup>[13]</sup> and  $\text{BaFe}_{12-2x}\text{Ti}_x\text{Co}_x\text{O}_{19}$  at 15–35 nm depending on the stoichiometry and the degree of particle shape anisotropy. <sup>[14]</sup> The loss of the ferroic hysteresis loop coupled with the ability to respond strongly to the presence of a magnetic field has been utilized in a variety of applications, including ferromagnetic fluids and high-frequency transformers where eddy current losses are a problem.

A similar mechanism has been proposed to explain the dielectric and elastic properties of relaxor ferroelectrics. <sup>[15]</sup> Compositions including many of the  $\text{A}(\text{B}'_{1/2}, \text{B}''_{1/2})\text{O}_3$  and  $\text{A}(\text{B}'_{2/3}, \text{B}''_{1/3})\text{O}_3$  perovskites exhibit microdomains (typically 2–30 nm in size) of 1:1 ordering on the B sublattice dispersed in a disordered matrix. It has been suggested that as a result of this nanostructure, the spontaneous polarization in these materials is also subdivided into very small local regions. Thus, a lead magnesium niobate ceramic can be regarded as a collection of

disordered but highly orientable dipoles. The result, much like the case of superparamagnetism, is a high dielectric permittivity over a broad temperature range even though the net spontaneous polarization is near zero. Because of the long range of the electric fields induced by the local dipoles, however, there is more interaction between the local electric dipoles than was present in the ideal superparamagnet. Consequently, the superparaelectric behavior in relaxor ferroelectrics is modulated by coupling between local moments, so that a spin glass model is necessary to describe the phase transition behavior. Evidence for the importance of the size of the microregions is given in experiments on materials that can be ordered by heat treatment. As a scale of the ordered regions grow beyond a certain size, the material reverts to ordinary ferroelectric (or antiferroelectric) behavior with a well-defined transition temperature and a nondispersive dielectric response.

### THIN FILMS

Although the general outline of size effects expected in films are similar to those demonstrated in ferromagnetic particles, it would not be surprising for the boundaries between different regions to shift along the size axis for different geometries. Kittel was one of the first to explore this possibility in ferromagnetic materials.<sup>[16]</sup> He calculated that in a film where the preferred magnetization is perpendicular to the major surface, the multidomain to single-domain transition should occur near 300 nm, an order of magnitude larger than the same transition in a particulate material. If however, there was either no anisotropy or the easy magnetization direction fell in the film plane, new types of domain walls may appear and persist down to very small sizes.

The transition to superparamagnetic behavior is apparently suppressed in comparatively perfect thin films produced in high-vacuum systems, probably because the large two-dimensional area raises the volume energy above the available thermal energy, even for very thin films. Consequently, regular ferromagnetic behavior persists in much thinner films (down to  $\sim 0.5$  nm for Ni films sandwiched between nonmagnetic layers<sup>[17]</sup>). In such samples, the ferromagnetic transition temperature also drops rapidly for films  $< 15$  nm thick.

Films that grow as discrete islands of magnetic material rather than continuous layers or that consists of magnetic particles isolated from each other by nonmagnetic hydride or oxide layers, on the other hand, should behave like particulate systems (undergoing superparamagnetic transitions appropriate for the primary magnetic particle size). This type of behavior has been confirmed in ferromagnetic films that became superparamagnetic at apparent thicknesses of 2.7 nm (where the film actually consisted of 5–10 nm islands). It is interesting that no change in the Curie temperature was noted before the onset of thermal randomization of the spins.

Given this information, what can be predicted about the behavior of ferroelectric thin films? First, for an unelectroded film it seems likely that ferroelectricity will remain stable at least down to thickness of  $\sim 100$  nm for  $\text{BaTiO}_3$  and possibly considerably lower for  $\text{PbTiO}_3$  films. This is in accord with several theoretical predictions for size effects in thin ferroelectric wafers in which, it was shown that when space charge effects (which will be considered in the following section) are discounted, the onset of intrinsic size effects is projected to fall in the range of 1–10 nm. <sup>[19]</sup>

Multidomain configurations should also remain stable down to very small sizes. Corroborating evidence for this is suggested by transmission electron microscopy (TEM) studies of thinned ferroelectric ceramics and single crystals where, provided the grain size is large enough, domains can be detected in foils below 100 nm thick. <sup>[20]</sup> When, however, the grain size in the film falls below some critical limit, the density of domains will probably decrease in a manner similar to that shown in ceramics.

Finally, as in the case of the magnetic films, unless there is some extrinsic mechanisms for forming discrete polar microregions, the onset of superparaelectricity should be depressed by the relatively large volume of ferroelectric.

The experimentally observed size effects reported in the ferroelectric thin-film literature fall into four major categories: an increase in the coercive field, a decrease in the remanent polarization, a depression in the dielectric constant, and a smearing of the paraelectric–ferroelectric transition over values expected from bulk materials of the same composition. One point that is apparent from a perusal of literature data is that deviations from bulk properties are nearly

universal, but the thickness at which the properties begin to diverge and the magnitude of the disparity are strongly dependent on the preparation conditions. Consequently, films produced at one laboratory may display marked size effects, while others of the same thickness and composition possess bulk properties.

The reason for this type of discrepancy lie in the variety of mechanisms causing the apparent size effect. Included among these are microstructural heterogeneities, variations in crystalline quality, mechanical stresses imposed on the film by the substrate, space charge effects, and finally intrinsic size effects. It is critical to note that the first two of these, which in the opinion of the authors account for the majority of the 'size effects' observed in thin-film properties, are in fact, size independent. Many film preparation techniques produce films that are defective and would remain defective even if macroscopic samples could be fabricated.

Inhomogeneity in the film microstructure can take the form of incorporated porosity, surface and interface roughness, or variations in the grain size. In particular, many ferroelectrics, grown by vapor deposition processes are columnar and should be expected to have low densities. This, in turn, could appreciably lower the dielectric constant than, if there was poor coupling between the grains, would increase the coercive field as well. Even in films that appear dense, Dudkevich *et al.*, have shown that the microstructure may change continuously as a function of film thickness.<sup>[21]</sup> Thus, for sputtered  $\text{Ba}_{0.85}\text{Sr}_{0.15}\text{TiO}_3$  films, thinner films tend to be composed of small particles (15 nm for a 4 nm thick film) where thicker films show a distribution of grain sizes ranging from the very fine particles deposited next to the substrate to larger grains at the film surface (200–300 nm for a film 2000 nm thick). Given this type of microstructural heterogeneity, it is no wonder that many properties appear to depend on film thickness. As the absolute grain size at any given thickness is expected to be a sensitive function of both the deposition conditions and any post-annealing, samples prepared at different laboratories should behave differently.

A second significant influence on thin-film properties is the crystalline quality of the ferroelectric material. It is known that the loss of clear X-ray diffraction peaks is coupled to the disappearance of the paraelectric–ferroelectric phase transition. Unfortunately, many film deposition techniques also result in poor crystallinity. During

sputtering, for example, the growing film is subjected to bombardment by high-energy ions. While this can be advantageous in terms of providing additional energy to the deposit and increasing the surface mobility, heavy bombardment, particularly at low substrate temperatures, can also introduce high defect concentrations. In chemically prepared thin films, on the other hand, low annealing temperatures can be insufficient to crystallize the ferroelectric phase fully.

Despite all of these opportunities for extrinsic size effects, there is evidence that films that are prepared carefully can display near bulk properties to very small thickness. In work on sol-gel PZT films, Udayakumar, for example, showed that room temperature dielectric constants of  $\sim 1300$  could be maintained for films exceeding 300 nm thick. The bulk remanent polarization was retained to 450 nm and remained finite, though reduced, in films 190 nm thick. The high breakdown strength of these films is also critical in device applications.

## CONCLUSIONS

As the field of ferroelectric thin film grows, it becomes increasingly important to examine the role of size effects on the expected properties. While intrinsic size effects similar to those demonstrated in ferromagnetic analogs will act as lower limits to the size of ferroelectric devices, in many cases extrinsic, processing-induced contributions overshadow the fundamental size restrictions. Consequently, careful characterization of films to determine the role of extrinsic effects (*i.e.*, internal microstructure, interface layers, and poor crystallinity) are necessary to understand relationships between processing and properties in ferroelectric films.

## Acknowledgements

We wish to acknowledge the National Science Foundation, contract No. DMR-9223847.

## References

- [1] Buffat, Ph. and Borel, J. P. (1976). *Phys. Rev. A*, 13(6), 2287–2298.
- [2] Takagi, M. (1954). *J. Phys. Soc. Jpn.*, 9(3), 359–363.

- [3] Hlasnik, I. *et al.* (1985). *Cryogenics*, **25**, 558–565.
- [4] Chainer, T., Morii, Y. and Kojima, H. (1980). *Phys. Rev. B*, **21**(9), 3941–3944.
- [5] Kneller, E. F. and Luborsky, F. E. (1963). *J. Appl. Phys.*, **34**(3), 656–658.
- [6] Kittel, C. (1946). *Phys. Rev.*, **70**(11,12), 965–971.
- [7] Berkowitz, A. E., Schuele, W. J. and Flanders, P. J. (1968). *J. Appl. Phys.*, **39**(2), 1261–1263.
- [8] Arlt, G., Hennings, D. and De With, G. (1985). *J. Appl. Phys.*, **58**(4), 1619–1625.
- [9] Lee, M. H., Halliyal, A. and Newnham, R. E. (1988). *Ferroelectrics*, (87), 71–80.
- [10] Uchino, K., Sadanaga, E., Oonishi, K., Morohashi, T. and Yamamura, H. (1990). *Ceram. Trans.*, (8), 107–115.
- [11] Ishikawa, K., Yoshikawa, K. and Okada, N. (1988). *Phys. Rev. B*, **37**(10), 5852–5855.
- [12] Kneller, E. F. and Luborsky, F. E. (1964). *J. Appl. Phys.*, **34**(3), 656–658.
- [13] Berkowitz, A. E., Schuele, W. J. and Flanders, P. J. (1968). *J. Appl. Phys.*, **39**(2), 1261–1263.
- [14] Kubo, O., Ido, T., Yokoyama, H. and Koike, Y. (1985). *J. Appl. Phys.*, **57**(1), 4280–4282.
- [15] Viehland, D., Jang, S.-J., Cross, L. E. and Wuttig, M. (1990). *J. Appl. Phys.*, **68**(6), 2918–2921.
- [16] Kittel, C. (1946). *Phys. Rev.*, **70**(11,12), 965–971.
- [17] Beauvillain, P., Chapert, C., Renard, J. P., Marliere, C. and Renard, D. (1986). *Magnetic Thin Films*, Krishnan, R. Ed., les Editions de physique, France.
- [18] Prutlon, M. (1964). *Thin Ferromagnetic Films*, Butlorworth and Co. Ltd, WA.
- [19] Binder, K. (1981). *Ferroelectrics*, (35), 99–104.
- [20] Tanaka, M. and Honjo, G. (1964). *J. Phys. Soc. Jpn.*, **19**(6), 954–970.
- [21] Dudkevich, V. P., Bukreev, V. A., Mukhortov, VI. M., Golovko, Yu. I., Sindeev, Yu. G., Mukhortov, V. M. and Fesenko, E. G. (1981). *Phys. Stat. Sol. (a)*, **65**, 463–467.

# **MATERIALS STUDIES**

**Relaxor Ferroelectric  
Single Crystal Systems**

# **APPENDIX 18**

# High electromechanical coupling piezoelectrics: relaxor and normal ferroelectric solid solutions

Kenji Uchino

*International Center for Actuators and Transducers, Materials Research Laboratory, The Pennsylvania State University, University Park, PA 16802, USA*

## Abstract

A new category of piezoelectric ceramics with very high electromechanical coupling was discovered in a lead zinc niobate–lead titanate solid solution in a single crystal form. The maximum coupling factor  $k_{33}$  reaches 95%, which corresponds to the energy conversion rate twice as high as the conventional lead zirconate titanate ceramics. This paper reviews the previous studies on superior piezoelectricity in relaxor ferroelectric: lead titanate solid solutions and on the possible mechanisms of this high electromechanical coupling. © 1998 Elsevier Science B.V. All rights reserved.

**Keywords:** Electromechanical coupling; Piezoelectric; Relaxor ferroelectric; Domain motion

## 1. Introduction

Lead zirconate–titanate (PZT) ceramics are well known piezoelectrics widely used in many transducers. Their applications include gas igniters, force/acceleration sensors, microphones, buzzers, speakers, surface acoustic wave filters, piezoelectric transformers, actuators, ultrasonic motors, ultrasonic underwater transducers, and acoustic scanners [1,2]. Particularly in recent medical acoustic imaging, higher electromechanical coupling materials are eagerly required to improve the image resolution. Under these circumstances, relaxor ferroelectric: lead titanate solid solution systems with superior electromechanical coupling factors to the conventional PZT have been refocused, which were initially discovered in a lead zinc niobate:lead titanate system by the author's group in 1981 [3].

This paper reviews the previous studies on superior piezoelectricity in relaxor ferroelectric: lead

titanate solid solutions, then on peculiar domain motions in these materials, finally possible mechanisms are considered for this extremely high electromechanical coupling.

## 2. Electromechanical coupling factors

The electromechanical coupling factor  $k$  of a piezoelectric element is defined as

$$k^2 = \frac{\text{Stored mechanical energy}}{\text{Input electrical energy}} \quad (1)$$

When an electric field  $E$  is applied to a piezoelectric transducer, since the input electrical energy is  $(1/2)\epsilon_0 \epsilon E^2$  per unit volume and the stored mechanical energy per unit volume under zero external stress is given by  $(1/2)\tau^2/s = (1/2)(dE)^2/s$ ,  $k^2$  can be calculated as

$$k^2 = [(1/2)(dE)^2/s]/[(1/2)\epsilon_0\epsilon E^2] = d^2/\epsilon_0\epsilon \cdot s. \quad (2)$$

This  $k^2$  must be distinguished from the terminology, efficiency  $\eta$ . In a work cycle (e.g. an electric field cycle), the input electrical energy is transformed partially into mechanical energy and the remaining is stored as electrical energy (electrostatic energy like a capacitor) in a transducer. Then, this ineffective energy can be returned to the power source, leading to near 97–99% efficiency, if the loss is small. Typical values of loss in PZT are about 1–3%.

The electromechanical coupling factor is different according to the sample geometry. In this paper, we will discuss two longitudinal vibration modes through longitudinal and transverse piezoelectric

effects,  $k_{33}$  and  $k_{31}$ . In some particular applications such as Non-Destructive Testing, large piezoelectric anisotropy, i.e. a large value of the ratio  $k_{33}/k_{31}$ , is required to improve the image quality in addition to a large value of  $k_{33}$  itself. However, the empirical rule suggests that these two requirements are contradictory to each other. In Fig. 1, we plotted the  $k_{33}$  versus  $k_{31}$  relation for various perovskite oxide piezoelectric polycrystal and single crystal samples such as  $\text{Pb}(\text{Zr}, \text{Ti})\text{O}_3$ ,  $\text{PbTiO}_3$ ,  $\text{Pb}(\text{Zn}_{1/3}\text{Nb}_{2/3})\text{O}_3$  and  $\text{Pb}(\text{Mg}_{1/3}\text{Nb}_{2/3})\text{O}_3$  based compositions [4]. It is obvious from this convex tendency that the piezoelectricity becomes isotropic (i.e. the  $k_{33}/k_{31}$  ratio approaches to 1) with increasing the electromechanical coupling factor (i.e. the  $k_{33}$  value).

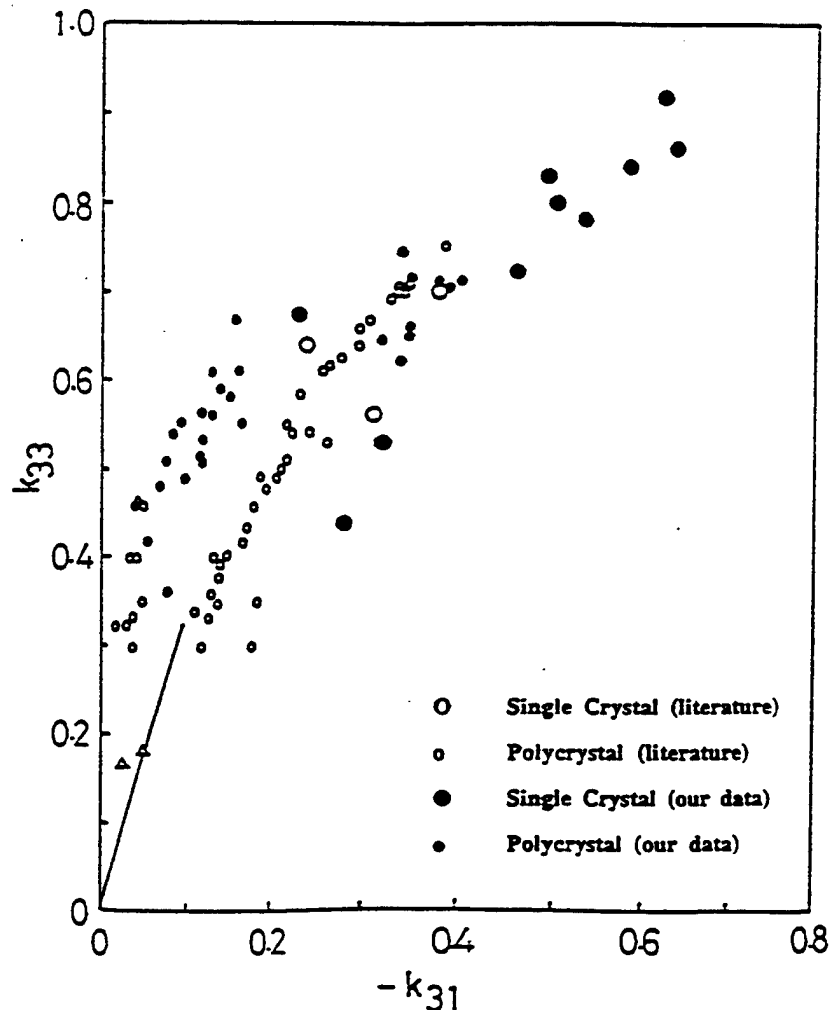


Fig. 1. Relation between  $k_{33}$  and  $k_{31}$  for various perovskite oxide piezoelectrics.

### 3. High electromechanical coupling materials

#### 3.1. Morphotropic phase boundary composition

Conventionally,  $\text{Pb}(\text{Zr}, \text{Ti})\text{O}_3$  (PZT),  $\text{PbTiO}_3$  (PT) and PZT based ternary ceramics with a small amount of a relaxor ferroelectric have been utilized for piezoelectric applications. In the PZT system, it is notable that the morphotropic phase boundary (MPB) composition between the rhombohedral and tetragonal phases exhibits the maximum enhancement in dielectric and piezoelectric properties; this is explained in terms of a phenomenological theory [5,6]. The physical properties of a perovskite solid solution between A and B,  $(1-x)\text{A}-x\text{B}$ , can be estimated through the Gibbs elastic energy of a solid solution, if we suppose a linear combination of the Gibbs elastic energy of each component:

$$G_i(P, X, T) = (1/2)[(1-x)\alpha_A + x\alpha_B]P^2 + (1/4)[(1-x)\beta_A + x\beta_B]P^4 + (1/6)[(1-x)\gamma_A + x\gamma_B]P^6 - (1/2)[(1-x)s_A + xs_B]X^2 - [(1-x)Q_A + xQ_B]P^2X, \quad (3)$$

where  $\alpha_A = (T - T_{0,A})/\epsilon_0 C_A$  and  $\alpha_B = (T - T_{0,B})/\epsilon_0 C_B$ .

The solution provides reasonable first-order estimates of the Curie temperature, spontaneous polarization and strain, as well as the enhancement of the permittivity, piezoelectric constant and electromechanical coupling at the MPB composition.

Note that in virgin samples of piezoelectric ceramics, the polarizations of grains are randomly oriented (or domains are oriented randomly even in each grain, if the grain size is large enough for a multi-domain state) so as to cancel the net polarization in total. In a similar fashion, the net strain is negligibly small under an external electric field. Hence, before use, it is necessary to apply a relatively large electric field ( $>3$  kV/mm) to align the polarization direction of each grain as much as possible (i.e. electric poling).

#### 3.2. Relaxor ferroelectric based composition

On the other hand, relaxor ferroelectrics such as  $\text{Pb}(\text{Mg}_{1/3}\text{Nb}_{2/3})\text{O}_3$ : $\text{PbTiO}_3$  compositions have been

focused due to their giant electrostriction [7]. Few work has been conducted on piezoelectric properties at the MPB region before the trial by the author's group.

We focused on single crystals of  $(1-x)\text{Pb}(\text{Zn}_{1/3}\text{Nb}_{2/3})\text{O}_3-x\text{PbTiO}_3$  (PZN-PT) which are relatively easily grown by a flux method over the whole composition range, compared with the case in the  $\text{Pb}(\text{Zr}, \text{Ti})\text{O}_3$  (PZT) system. This system exhibits a drastic change from a diffuse phase transition to a sharp transition with an increase of the PT content,  $x$ , correlating to the existence of a morphotropic phase boundary from a rhombohedral to a tetragonal phase around  $x=0.1$  [8]. Fig. 2 shows the phase diagram of this system near the MPB region.

The most intriguing piezoelectric characteristics have been found in the MPB compositions with

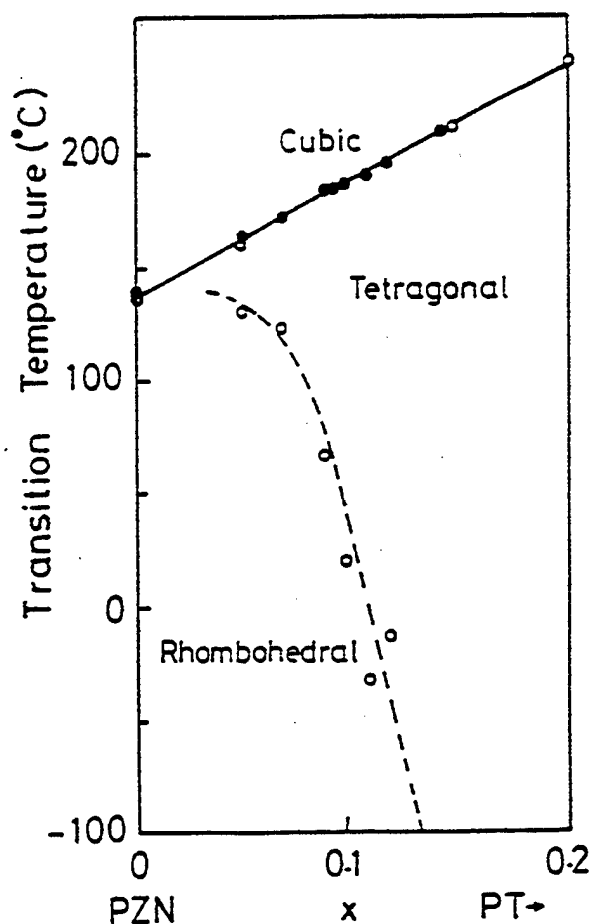


Fig. 2. Phase diagram of  $(1-x)\text{Pb}(\text{Zn}_{1/3}\text{Nb}_{2/3})\text{O}_3-x\text{PbTiO}_3$  (PZN-PT).

$0.05 < x < 0.143$ , which exhibit two multiple phase transitions, changing the crystal symmetry from rhombohedral to tetragonal, then to cubic during heating [3]. Fig. 3 shows the composition depen-

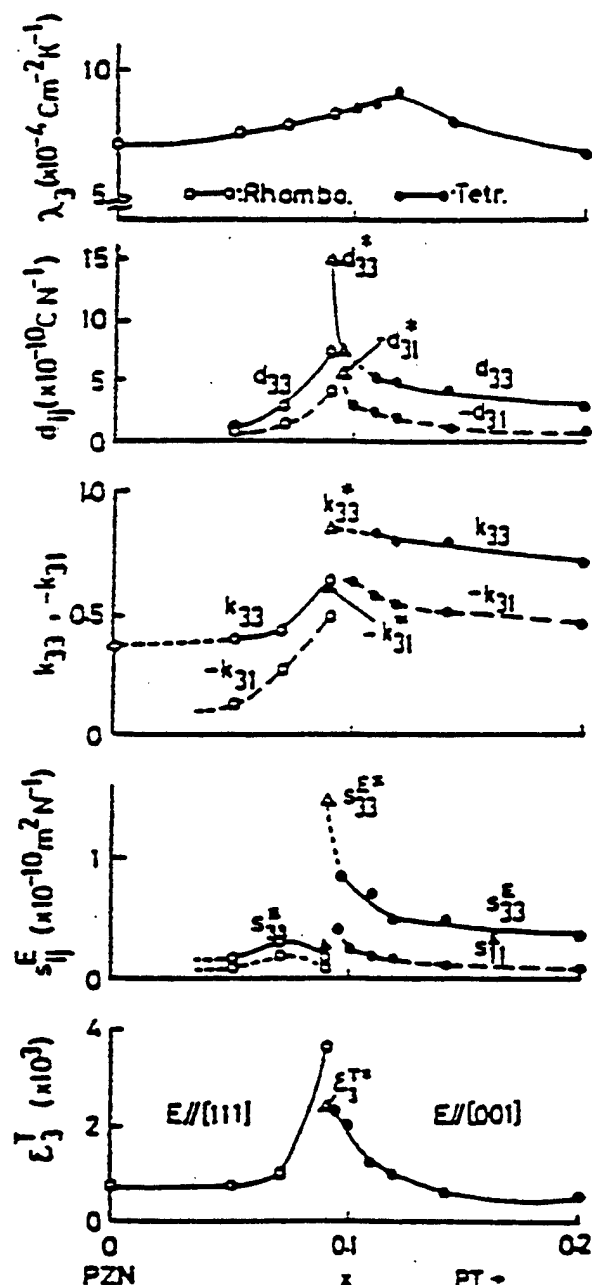


Fig. 3. Composition dependence of the pyroelectric coefficient  $\lambda_3^T$ , piezoelectric constants  $d_{ij}$ , electromechanical coupling factors  $k_{ij}$ , elastic compliances  $s_{ij}^E$  and dielectric constant  $\epsilon_3^T$  measured in  $(1-x)\text{Pb}(\text{Zn}_{1/3}\text{Nb}_{2/3})\text{O}_3-x\text{PbTiO}_3$  at room temperature.

dence of the pyroelectric coefficient  $\lambda_3^T$ , piezoelectric constants  $d_{ij}$ , electromechanical coupling factors  $k_{ij}$ , elastic compliances  $s_{ij}^E$  and dielectric constant  $\epsilon_3^T$  measured at room temperature [3]. The superscript \* is for the crystal with the rhombohedral symmetry at room temperature poled along the pseudocubic [001] direction. Fig. 4 shows the temperature dependence of electromechanical coupling factors  $k_{33}$  and  $k_{31}$  measured with bar-shaped specimens of 0.91PZN–0.09PT [9]. Special notations have been introduced to describe the elastic and electromechanical constants for a sample poled in a certain direction. The  $s_{[001]//}^E$  or  $s_{[111]//}^E$  are defined from the resonance frequency of a bar sample elongated and poled in the pseudocubic [001] or [111] axes, respectively. The [001] and [111] axes are the principle axes of the tetragonal and rhombohedral phases and also the poling directions for each sample. The coupling coefficients  $k_{[001]//}$  and  $k_{[111]//}$  are consequently

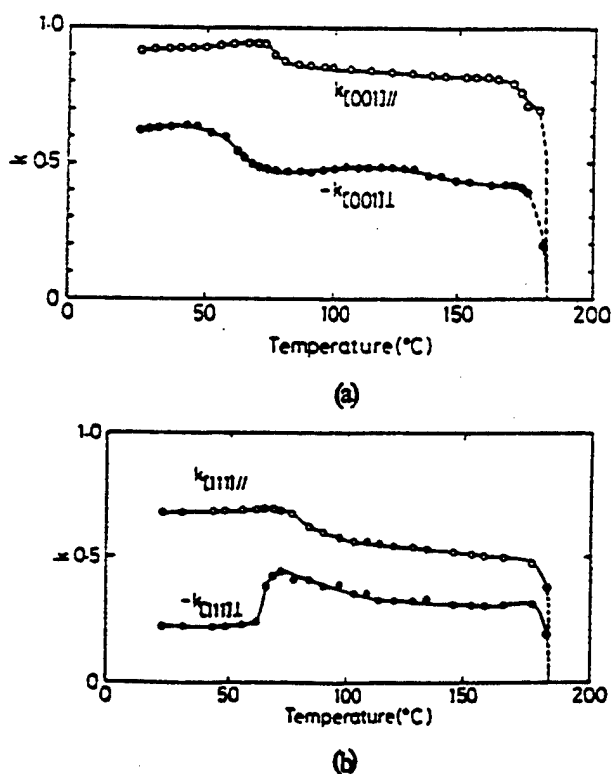


Fig. 4. Temperature dependence of electromechanical coupling factors  $k_{33}$  and  $k_{31}$  measured with bar-shaped specimens of 0.91PZN–0.09PT.

calculated from the resonance and anti-resonance frequencies of the same sample. All the electromechanical components show a very large kink anomaly at the rhombohedral–tetragonal transition temperature, and a rapid decrease in  $k$  or an increase in  $d$  and  $s^E$  on approaching the Curie point. These components vanish just above the Curie point.

It is important that the sample electrically poled along the pseudocubic [001] axis (not the principal axis in the rhombohedral phase!) reveals a very large piezoelectric constant  $d_{[001]//} = 1.5 \times 10^{-9}$  C/N and a high electromechanical coupling factor  $k_{[001]//} = 0.92$  at room temperature, both of which are much larger than  $d_{[111]//}$  and  $k_{[111]//}$ , respectively. Also these are the highest values among all perovskite piezoelectric materials reported so far. It is indicated that such a high electromechanical coupling factor can be explained in terms of a combination effect of crystal orientation dependence of piezoelectric properties in a mono-domain single crystal with phase transition-related complicated domain dynamical motion. The details of this model will be described in the next section.

Recently, two groups of Yamashita (Toshiba) and Shrout (Penn State) reconfirmed the author's original work, and extended the investigation to a wide range of relaxor ferroelectrics such as  $\text{Pb}(\text{Mg}_{1/3}\text{Nb}_{2/3})\text{O}_3$ –PT,  $\text{Pb}(\text{Sc}_{1/2}\text{Ta}_{1/2})\text{O}_3$ –PT and  $\text{Pb}(\text{Sc}_{1/2}\text{Nb}_{1/2})\text{O}_3$ –PT. Large electromechanical coupling factors  $k_p$ ,  $k_{33}$  and piezoelectric constant  $d_{33}$  of these binary systems are listed in Table 1.

Intriguing measurements on electric field-induced polarization and strain were carried out on a pure PZN single crystal by Shrout et al. [16]. The polarization and strain curves are plotted for the

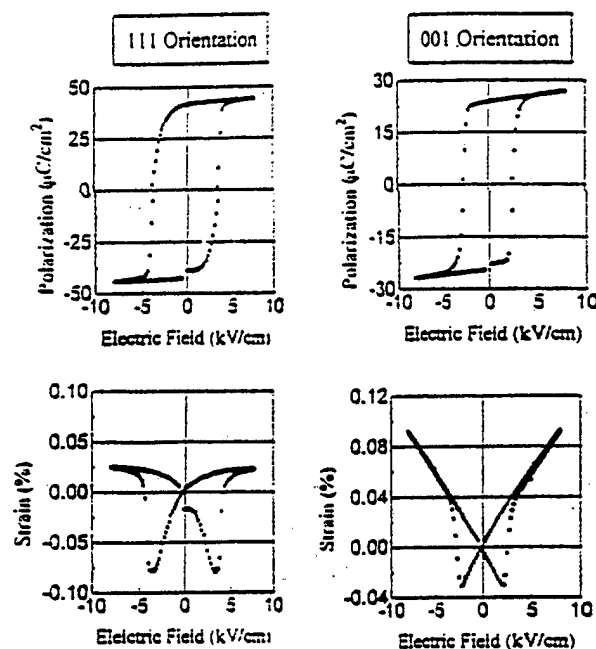


Fig. 5. Polarization and strain curves plotted for the (111) and (001) orientations in pure PZN [cited from Ref. [16]].

(111) (the spontaneous polarization direction!) and (001) orientations in Fig. 5. Even though the [001] plate sample showed the 'ideal'  $P$  vs.  $E$  or strain vs.  $E$  behaviors of a mono-domain crystal, notice that the absolute value of  $P$  is much larger in the [111] plate sample: this indicates again the spontaneous polarization along the (111) axis. He also reported the poling direction-dependent electromechanical coupling factors in PZN:  $k_{[001]//} = 0.85$  was much larger than  $k_{[111]//} = 0.38$ , in a similar fashion to 0.91PZN–0.09PT. Fig. 6 shows a large field induced strain curve measured for a 0.92PZN–0.08PT (001)

Table 1

Large electromechanical coupling factors  $k_p$ ,  $k_{33}$  and piezoelectric constant  $d_{33}$  of relaxor ferroelectric binary systems

Material	Feature	$k_p$ (%)	$k_{33}$ (%)	$d_{33}$ (pC/N)	Reference
PZT 53/47	Polycrystal	52	67	220	[10]
		67	76	400	[11]
PZN:PT 91/9	Single crystal		92	1500	[9]
PMN:PT 67/33	Polycrystal	63	73	690	[12]
	Single crystal			1500	[13]
PST:PT 55/45	Polycrystal	61	73	655	[14]
PSN:PT 58/42	Polycrystal	71	77	450	[15]

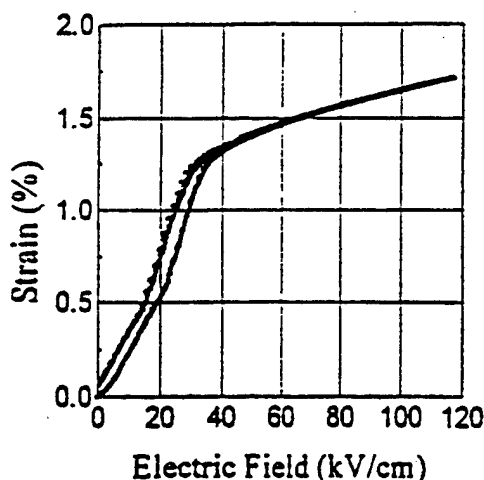


Fig. 6. Strain vs. electric field curve for the (001) plate 0.92PZN-0.08PT crystal [cited from Ref. [17]].

plate sample [17]. Notice a strain level more than 1% and a significant bend anomaly on the curve, which suggests a field-induced transition from the rhombohedral to tetragonal phase.

#### 4. Origins of the high electromechanical coupling

As we have mentioned, in addition to the MPB composition, a high electromechanical coupling factor can be attributed to crystal orientation dependence of piezoelectric properties in a mono-domain single crystal and phase transition-related complicated domain dynamical motion. We will consider these two aspects.

##### 4.1. Crystal orientation dependence of piezoelectric properties

Crystal orientation dependence of piezoelectric properties can be calculated phenomenologically in the 3-dimensional space, if all the necessary parameters are known. Since some of elastic constants in the PZN-PT have not been measured, we tried to calculate for a hypothetical PZT single crystal [18]. The calculation has been made for tetragonal PZT 40/60 and rhombohedral 60/40 compositions.

Fig. 7 shows the orientation dependence of the longitudinal piezoelectric constant  $d_{33}$  (the  $k_{33}$  ten-

dency is also similar) for the tetragonal (a) and rhombohedral composition (b). The maximum value occurs along the spontaneous polarization direction in the tetragonal composition. However, the result for the rhombohedral crystal is very different; i.e. the maximum value of  $d_{33}$  can be obtained in the direction  $56.7^\circ$  away from the polarization direction. Roughly speaking, along the perovskite [001] direction,  $d_{33}$  and  $k_{33}$  values are most enhance in rhombohedral PZT 60/40. Some interesting parallels can be drawn with PZN-PT. The ratios  $d_{[111]}/d_{33(\max)}=0.395$  and  $k_{[111]}/k_{33(\max)}=0.69$  calculated for PZT 60/40 are very close to the experimental values  $d_{[111]}/d_{[100]}=625(\text{pC/N})/1570(\text{pC/N})=0.398$  and  $k_{[111]}/k_{[100]}=0.68/0.92=0.74$  in 0.91PZN-0.09PT [9].

##### 4.2. Domain motion in relaxor ferroelectrics

Historically, most of the studies on ferroelectric single crystals and polycrystalline materials have aimed to simulate the mono-domain state, desiring to derive the better characteristics from the specimens: ceramics as well as single crystals were poled electrically and/or mechanically to reorient the domains along one direction. Researches on controlling domains intentionally can be found in electrooptic devices and ferroelectric memory devices in particular. However, the intentional domain control has not been utilized or applied occasionally in the actuator and transducer areas. Recent requirements for the higher performance transducers encourages the investigation on the possibility of domain-related effect usage.

Developments in high resolution CCD optical microscope systems and in single crystal growth techniques are also accelerating these domain-controlled piezoelectric devices. We used a high resolution CCD (Charge Coupled Device) camera attached to a Nikon Transmission Petrographic Microscope which was connected to a monitor and VCR [19,20].

Let us review the relation between domain configurations and physical properties in relaxor ferroelectrics. The static domain configurations for the  $(1-x)\text{PZN}-x\text{PT}$  samples have been reported [21]; rhombohedral domains can be described as having an ambiguous spindle-like morphology. With increasing

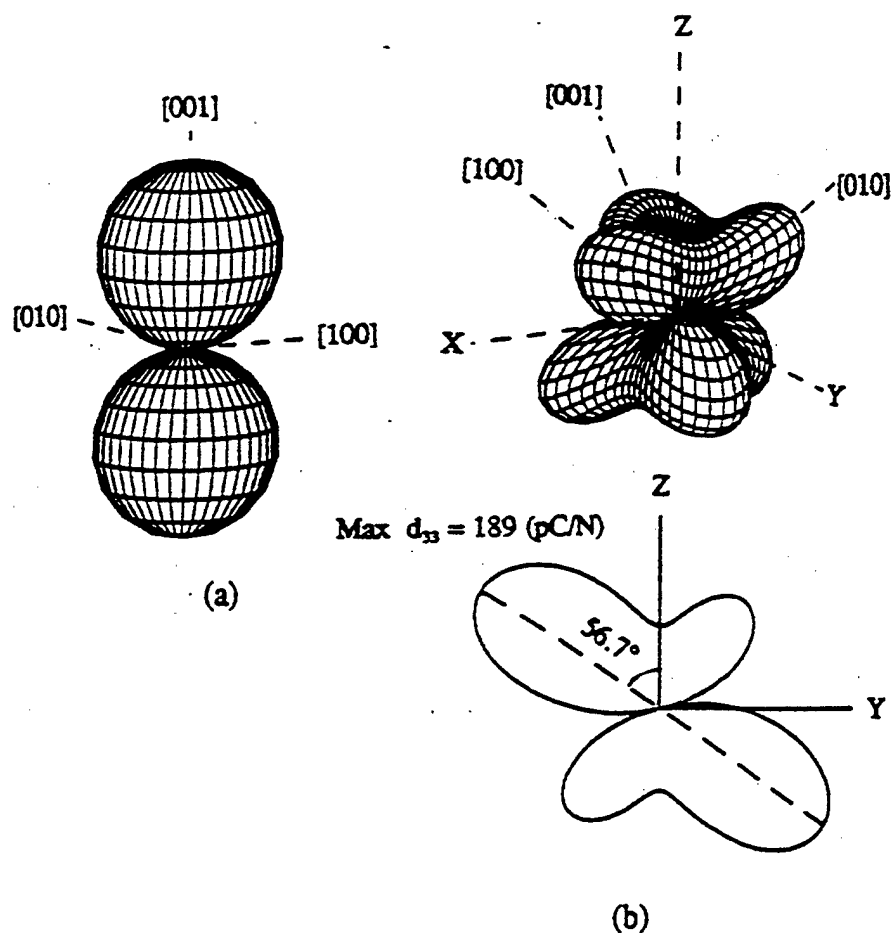


Fig. 7. Crystal orientation dependence of piezoelectric constant  $d_{33}$  for tetragonal PZT 40/60 (a), and for rhombohedral PZT 60/40 (b).

the PT content, this small spindle-like domain is enlarged and the domain wall becomes sharp. Tetragonal domains appear to have a well defined lamellar morphology, and are either at right angles or antiparallel. Therefore, even though the widths and lengths of the tetragonal domains vary, the divisions between the domains are well defined and no interpenetrating structure is observable. The morphotropic phase boundary (MPB) composition ( $x = 0.095$ ) shows the coexistence of both rhombohedral (spindle-like) and tetragonal domains (sharp straight line): the two-phase coexistence can not be found statically in normal ferroelectric materials such as  $\text{BaTiO}_3$ .

Fig. 8 shows the domain reversal processes under an applied electric field [22]. Sharp  $90^\circ$  domain walls corresponding to the tetragonal symmetry in the sample with  $x = 0.2$  move abruptly and rather in-

dependently each other above a coercive field of 1 kV/mm. The situation resembles to the case in normal ferroelectrics. On the contrary, pure PZN ( $x = 0.0$ ) reveals very different domain motion. During electric field cycles, micro- to macro-domain growth occurs, and long narrow spindle-like domains (aspect ratio = 10) are arranged rather perpendicularly to the electric field ( $18^\circ$  canted). When a field above 0.5 kV/mm is applied, the ambiguous domain walls ripple simultaneously in a certain size region, so that each domain should change synchronously like cooperative phenomena. The domain reversal front ( $180^\circ$  domain wall) move rather slower than in the sample of  $x = 0.2$ . It is noteworthy that the stripe period of the dark and bright domains (probably corresponding to up and down polarizations) is not changed by the domain reversal, and that each domain area changes under an AC external field with

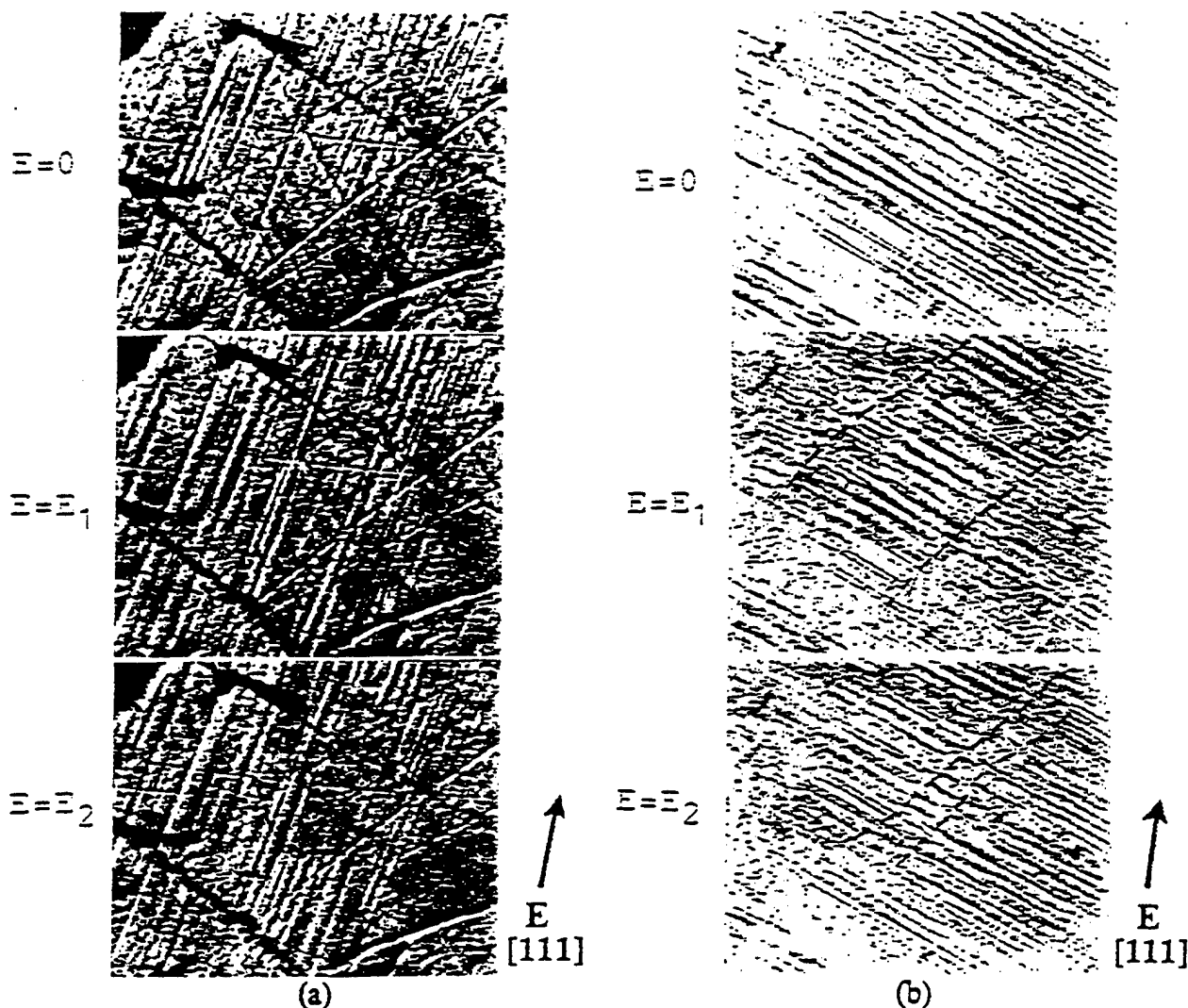


Fig. 8. Actual domain reversal processes under an applied electric field for the samples of  $x=0.2$  (a) and  $x=0$  (b) of  $(1-x)\text{Pb}(\text{Zn}_{1/2}\text{Nb}_{1/2})\text{O}_3-x\text{PbTiO}_3$ .

zero net polarization at zero field. Thus, the relaxor crystal is electrically-poled easily when an electric field is applied around the transition temperature, and depoled completely without any remnant polarization. This can explain large apparent secondary non-linear effects in physical properties such as electrostrictive and electrooptic phenomena, without exhibiting any hysteresis.

Fig. 9 shows the domain structures observed in a 0.89PZN–0.11PT crystal, which exists on the morphotropic phase boundary and has a tetragonal symmetry at room temperature. The typical tetragonal stripe domain pattern is observed without an

external electric field at room temperature, while the spindle-like rhombohedral domain pattern appears as overlapped on the stripe pattern, when the electric field is applied along the perovskite pseudo-cubic [111] direction. This domain hierarchy suggests that the morphotropic phase boundary composition may easily change the domain configuration and the crystal symmetry according to the applied electric field direction, from tetragonal to rhombohedral and vice versa, much easily than in the normal ferroelectric PZT (see Fig. 6 measured by Park et al.). Future work will include the dynamic domain observation in the 0.91PZN–0.09PT sample (rhombohedral phase is

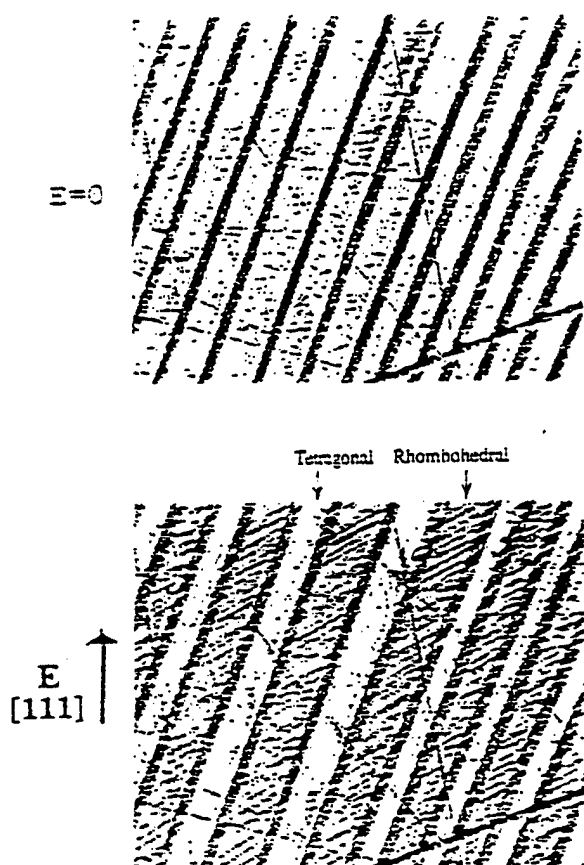


Fig. 9. Domain structures observed in an MPB composition crystal 0.39PZN-0.11PT.

stable at room temperature) poled along the perovskite [001] axis: this may contribute partly to the high electromechanical coupling factor  $k$  up to 92–95%.

## 5. Conclusions

1. The electromechanical coupling factor  $k_{33}$  of more than 90% can be obtained in the solid solutions between the relaxor and normal ferroelectrics. Promising compositions include:  $\text{Pb}(\text{Zn}_{1/3}\text{Nb}_{2/3})\text{O}_3$ – $\text{PbTiO}_3$ ,  $\text{Pb}(\text{Mg}_{1/3}\text{Nb}_{2/3})\text{O}_3$ – $\text{PbTiO}_3$  and  $\text{Pb}(\text{Sc}_{1/2}\text{Nb}_{1/2})\text{O}_3$ – $\text{PbTiO}_3$ .
2. The maximum  $k$  can be obtained around the morphotropic phase boundary composition between the tetragonal and rhombohedral phases.
3. The highest  $k$  in a single crystal form can be obtained when a rhombohedral composition is

electrically-poled along a different axis from the spontaneous polarization direction, i.e., pseudo-cubic [001] direction.

A high electromechanical coupling factor can be attributed to crystal orientation dependence of piezoelectric properties in a mono-domain single crystal and phase transition-related complicated domain dynamical motion. Domain controlled single crystals (not in the monodomain state!) may be the key for obtaining the highest electromechanical coupling, and relaxor ferroelectrics may be suitable to demonstrate this model.

## Acknowledgements

This work was supported by the Office of Naval Research under Grant No. N00014-91-J-1145.

## References

- [1] K. Uchino, Proceedings 4th International Conference on Electronic Ceramics and Applications, Vol. 1, Aachen, Germany, Sept. 5–7, 1994, p. 179.
- [2] K. Uchino, Piezoelectric Actuators and Ultrasonic Motors, Kluwer Academic Publishers, Boston, 1996.
- [3] J. Kuwata, K. Uchino, S. Nomura, *Ferroelectrics* 37 (1981) 579.
- [4] K.H. Hellwege et al., Landolt-Bornstein, Group III, Vol. 11, Springer-Verlag, New York, 1979.
- [5] K. Uchino, S. Nomura, *Jpn. J. Appl. Phys.* 18 (1979) 1493.
- [6] K. Abe, O. Furukawa, H. Inagawa, *Ferroelectrics* 87 (1988) 55.
- [7] K. Uchino, *Bull. Am. Ceram. Soc.* 65(4) (1986) 647.
- [8] S. Nomura, T. Takahashi, Y. Yokomizo, *J. Phys. Soc. Jpn.* 27 (1969) 262.
- [9] J. Kuwata, K. Uchino, S. Nomura, *Jpn. J. Appl. Phys.* 21(9) (1982) 1298.
- [10] B. Jaffe, R.S. Roth, S. Marzullo, *J. Res. Natl. Bur. Stand.* 55 (1955) 239.
- [11] H. Igarashi, *Mem. Natl. Def. Acad.* 22 (1982) 27.
- [12] S.W. Choi, T.R. Shrout, S.J. Jang, A.S. Bhalla, *Ferroelectrics* 100 (1989) 29.
- [13] T.R. Shrout, Z.P. Chang, N. Kim, S. Markgraf, *Ferroelectrics Lett.* 12 (1990) 63.
- [14] J.F. Wang, J.R. Giniewicz, A.S. Bhalla, *Ferroelectrics Lett.* 16 (1993) 113.
- [15] Y. Yamashita, *Jpn. J. Appl. Phys.* 33 (1994) 4652.
- [16] T.R. Shrout, ONR Transducer Workshop, State College, March, 1996.

- [17] S.E. Park, T.R. Shrout, *J. Mater. Res. Innovations* 1 (1997) 20.
- [18] X.H. Du, U. Belegundu, K. Uchino, *Jpn. J. Appl. Phys.* 36 (1997) 5580.
- [19] M.L. Mulvihill, L.E. Cross, K. Uchino, *J. Am. Ceram. Soc.* 78 (1996) 3345.
- [20] M.L. Mulvihill, L.E. Cross, K. Uchino, *Proc. 8th European Mtg. on Ferroelectrics, Ferroelectrics* 186 (1996) 325.
- [21] K. Kato, K. Suzuki, K. Uchino, *J. Jpn. Ceram. Soc.* 98(8) (1990) 840.
- [22] R. Ujiie, K. Uchino, *Proc. IEEE Ultrasonic Symp. '90, Hawaii*, vol. 2, 1991, p. 725.

# **APPENDIX 19**

## Domain Configuration and Ferroelectric Related Properties of Relaxor Based Single Crystals

S. WADA\*, S. -E. PARK, L. E. CROSS and T. R. SHROUT

Materials Research Laboratory, The Pennsylvania State University, University Park, PA 16802, USA

\*Visiting Scholar, current address

Department of Applied Chemistry, Tokyo University of Agriculture & Technology, Tokyo 184, Japan

Domain configuration and ferroelectric related properties of rhombohedral  $\text{Pb}(\text{Zn}_{1/3}\text{Nb}_{2/3})\text{O}_3$  and its solid solution with  $\text{PbTiO}_3$  were investigated as a function of E-field and crystallographic orientation. Although a single domain state could be achieved by applying an E-field along the rhombohedral polar direction [111], a multidomain state was recovered with the removal of the E-field. This domain instability resulted in hysteresis of the strain vs. E-field behavior. In contrast, an engineered domain configuration of [001] oriented rhombohedral crystals was found to be stable with no domain motion detectable under DC-bias, resulting in hysteresis minimized strain vs. E-field behavior. Crystallographically, this domain stability could be ascribed to the macroscopically tetragonal symmetry (4mm), resulting from the engineering of domains with rhombohedral symmetry (3m).

### I. INTRODUCTION

Recent crystallographic engineering of relaxor ferroelectric single crystals of  $\text{Pb}(\text{Zn}_{1/3}\text{Nb}_{2/3})\text{O}_3$  (PZN),  $\text{Pb}(\text{Mg}_{1/3}\text{Nb}_{2/3})\text{O}_3$  (PMN) and their solid solutions with the normal ferroelectric  $\text{PbTiO}_3$  (PT) revealed piezoelectric properties much superior to morphotropic phase boundary (MPB) ceramics such as PZT. [1-4] Ultrahigh piezoelectric properties ( $d_{33} \sim 2500$  pC/N) and large E-field induced strain values (1.7%) were achievable from rhombohedral PZN-PT, PMN-PT, and  $\text{Pb}(\text{Sc}_{1/3}\text{Nb}_{2/3})\text{O}_3$ -PT crystals oriented along [001]. As [001] is not the polar direction, [001] poled crystals must be comprised of a multidomain state. However, it should be noted that strain values as high as 0.6% were realized with minimized hysteresis, indicating little domain motion under bias, a phenomena not expected for multidomain ferroelectric crystals. In contrast, crystals oriented along [111], the polar direction of rhombohedral crystals, exhibited inferior properties such as  $d_{33} \sim 82$  pC/N, significantly smaller than PZT's. Furthermore, the E-field induced strain was also accompanied by large hysteresis, which was believed to be originated from domain instability and subsequent domain motion under bias. [2,3] To further evaluate the origin of the apparent anisotropy, in-situ domain observations were proposed to further substantiate the concept of domain instability. In this study, in-situ domain observations were carried out as a function of E-field and crystallographic orientation. Based on the commonalities inherent to relaxor-PT systems [5,6], our research was limited to a rhombohedral PZN and PZN-8% PT crystals oriented along [111] and [001]. The

concept of macroscopic symmetry, resulting from crystallographic domain engineering, will be discussed in conjunction with the observed hysteresis minimized strain behavior and associated static domain configuration in multidomain crystals.

### II. EXPERIMENTAL

PZN and PZN-8% PT single crystals were grown by a flux method. Further details on the crystal growth were reported elsewhere [2,7]. Flux grown crystals were oriented along [111] or [001] direction using a back reflection Laue camera. Samples were heat-treated at 250 °C for 16 hours in air before domain observations, in order to remove residual stress that might result in the formation of ferroelastic domains. For in-situ domain observation under DC-bias, the sample surface was mirror-polished with the sample thickness approximately 200–300  $\mu\text{m}$  along the transmittance direction of polarized light. Gold electrodes were sputtered on both sides parallel to the polarized light. Sample width between sputtered Au electrodes was approximately 500–600  $\mu\text{m}$ . Thin samples ( $\sim 50$   $\mu\text{m}$ ) with mirror-finished (111) or (001) surfaces were also prepared to observe domain walls more clearly before and after E-field exposure under no bias, for crystallographic interpretation. The domain configuration, or state of the crystals, was observed under cross-nicol condition using a Polarized microscopy (Carl Zeiss, D-7082). The application of an E-field was along the [001] or [111] direction, being normal to polarized light, using a Trek 610A HV Amplifier.

### III. RESULTS AND DISCUSSION

#### 1. Domain Configuration - No Bias Before and After E-field Exposure

As grown PZN crystals were previously reported to be optically isotropic [8,9] with ferroelectric domains observed in PZN crystals only upon exposure with an applied E-field, resulting from the microdomain-macrodomain transition. However, stripe-shaped domain patterns were observed for both [111] and [001] oriented PZN crystals upon heat treatment at 250 °C for 16 hours. Surprisingly, this stripe pattern did not disappear even at temperatures above  $T_{max}$  (145 °C). Therefore, the stripe patterns may have resulted from another origin, such as residual stress associated with lattice defects.

Domain configurations of [111] and [001] oriented PZN crystals, respectively, after E-field ( $\sim 40$  kV/cm) exposure were observed. The [111] oriented PZN crystals consisted of band-shaped domains with three equivalent polar vectors ( $[\bar{1}\bar{1}1]$ ,  $[1\bar{1}1]$  and  $[\bar{1}1\bar{1}]$ ). All domain boundaries could be interpreted as 109° domain walls on {110} planes, consistent with crystallographic domain wall relationships [10,11]. Fiber-like domains with sharp edges on both ends were observed for [001] oriented PZN crystals. Although crystallographic interpretation was limited by the depth of focus of optical microscopy, each domain must have one of four possible polar vectors,  $[111]$ ,  $[\bar{1}\bar{1}\bar{1}]$ ,  $[1\bar{1}1]$  and  $[\bar{1}1\bar{1}]$ . Similar domain configuration and behavior was found for PZN-8% PT to that of PZN, except for the ferroelectric domains initially observed from as-grown crystals.

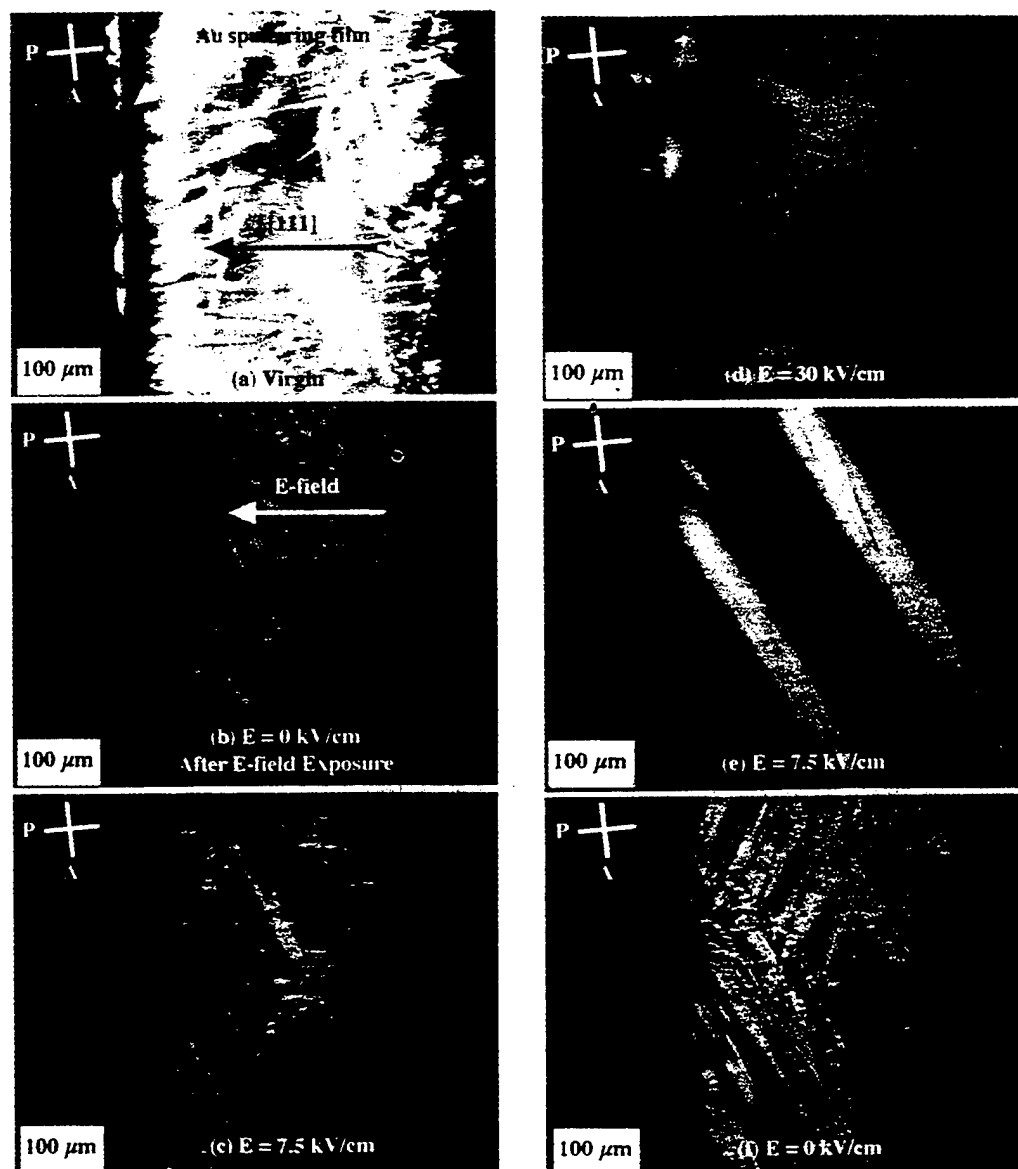


Fig. 1. Domain structure of pure PZN single crystal oriented along [111] under DC-bias.

## 2. In-situ Domain Observations

Figs. 1(a), (b) and (c) exemplify the domain configuration for  $[111]$  oriented PZN crystals as a function of E-field, increased incrementally to 30 kV/cm. The Domain wall density in the crystals was found to decrease with increased E-field, implying the increased domain size with domain reorientation. At approximately 30 kV/cm, the PZN crystals became almost single domain, with some domain walls observed near the electrode due to crystal-electrode interfacial stress. However, upon removal of the E-field, a multidomain state was observed as presented in Figs. 1(e) and (f). Domain reorientation was found to occur at 7.5 kV/cm (Fig. 1(d)), starting near the electrode. The initial multidomain state of Fig. 1(a) was completely recovered as shown in Fig. 1(f). However, it should be noted that the domain configuration exhibited hysteresis. The domain wall density was observed to be lower for an equivalent E-field upon removing the E-field, the origin of hysteresis in strain vs. E-field curve. Hence, to achieve single domain PZN crystals at 0 E-field, the application of an elastic force, as used to fabricate single domain  $\text{BaTiO}_3$  crystal, may be required [12]. In contrast to the domain instability observed with  $[111]$  oriented PZN crystals,  $[001]$  oriented crystals exhibited stable domain configurations as shown in Fig. 2. Domain configuration did not change under bias, being further evidenced by hysteresis minimized strain vs. E-field behavior. Similar domain behavior was found in PZN-8%PT but at differ-

ent E-fields, i.e., a single domain state was observed for PZN-8% PT at 13 kV/cm.

## 3. Domain Engineering and Macroscopic Symmetry

Based on the domain observations presented in previous sections, the ability to engineer a macroscopic symmetry different from the local symmetry (lattice symmetry) is suggested, as can be found for the case of poled piezoelectric ceramics, i.e., the macroscopic symmetry being com regardless of the lattice symmetry resulting from randomly orientated grains. For ferroelectric single crystals, only single domain crystals possess macroscopic symmetry identical to the lattice symmetry. For example, unpoled tetragonal ferroelectric crystals are macroscopically  $m3m$ , if the number of each domain is equivalently distributed. Each domain in  $[001]$  oriented crystals must have four possible polarization directions,  $[111]$ ,  $[\bar{1}11]$ ,  $[1\bar{1}1]$  and  $[\bar{1}\bar{1}1]$ . For  $[001]$  oriented crystals to exhibit a static domain configuration under bias, each domain must be distributed equivalently. As a result, each domain experiences the same driving force for reorientation with respect to an applied E-field, otherwise domain reorientation under bias would occur resulting in hysteresis in strain vs. E-field behavior. Therefore, the coexistence of domains with four equivalent polar vectors results in a 4-fold axis along  $[001]$ , consequently resulting

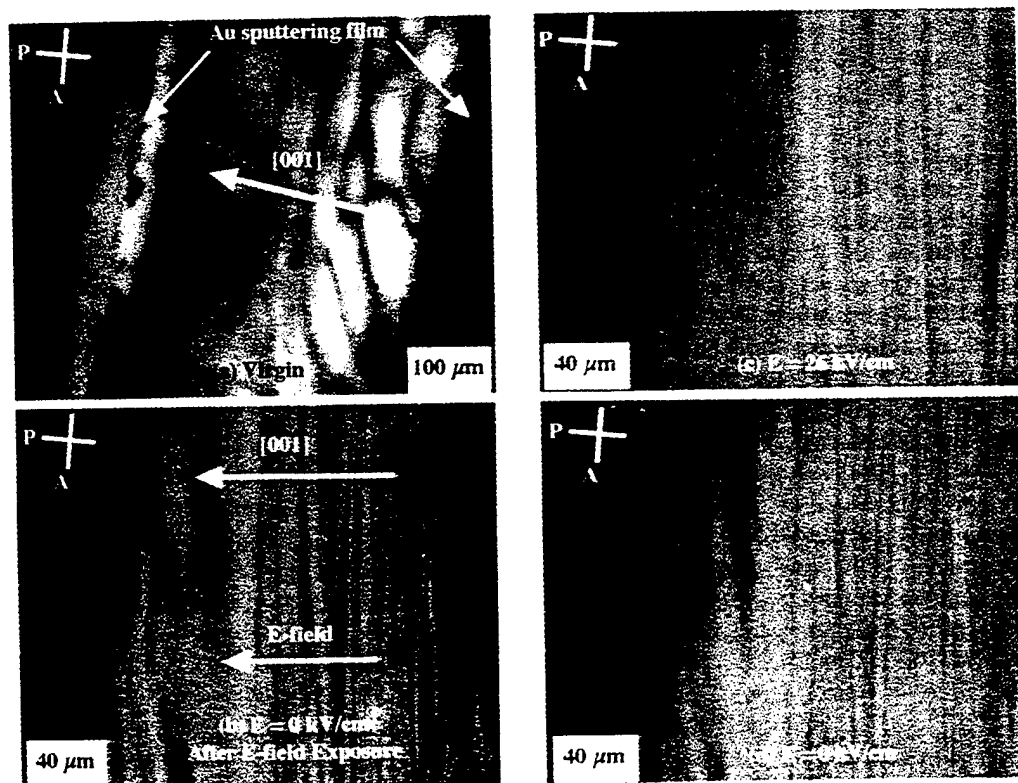


Fig. 2. Domain structure of pure PZN single crystal oriented along  $[001]$  under DC-bias.

in the macroscopic symmetry 4mm arising from the local 3m symmetry. gestions.

#### IV. SUMMARY

Domain configuration and ferroelectric related properties of rhombohedral PZN, and PZN-8% PT crystals were investigated as a function of E-field and crystallographic orientation. In-situ domain observations revealed the domain instability for [111] oriented rhombohedral crystals, resulting in hysteresis of the strain vs. E-field behavior. In contrast, an engineered domain configuration of [001] oriented rhombohedral crystals was found to be stable. No domain motion was detectable under DC-bias, resulting in hysteresis minimized strain vs. E-field behavior. Crystallographically, the macroscopic tetragonal symmetry (4mm) arising from local rhombohedral 3m symmetry resulting from the four equivalent domain state was suggested. Further studies such as TEM observations are required to understand the stripe patterns observed in as-grown PZN crystals.

#### ACKNOWLEDGMENTS

Authors would like to thank Mrs. Lei for her help with sample preparation. We also thank Dr. Fousek, Dr. Newnham, Dr. Randall and Dr. Cao for their helpful sug-

#### REFERENCES

- [1] J. Kuwata, K. Uchino and S. Nomura, *Jpn. J. Appl. Phys.* 21, 1298 (1982).
- [2] S. -E. Park, M. L. Mulvihill, P. D. Lopath, M. Zipparo and T. R. Shrout, *Proceedings of the 10th IEEE International Symposium on Applications of Ferroelectrics*, Vol. I (1996), p. 79.
- [3] S. -E. Park and T. R. Shrout, *J. Appl. Phys.*, in press.
- [4] S. -E. Park and T. R. Shrout, unpublished.
- [5] T. R. Shrout and J. Fielding, Jr., *Proceedings of the 1990 IEEE Ultrasonics Symposium* (1990), p. 711.
- [6] C. A. Randall, A. S. Bhalla, T. R. Shrout and L. E. Cross, *J. Mater. Res.* 5, 829 (1990).
- [7] S. -E. Park, M. L. Mulvihill, G. Risch and T. R. Shrout, *Jpn. J. Appl. Phys.* 36, 1154 (1997).
- [8] S. Nomura, M. Endo and F. Kojima, *Jpn. J. Appl. Phys.* 13, 2004 (1974).
- [9] M. L. Mulvihill, Doctor thesis (Pennsylvania State University, 1996).
- [10] J. Fousek, *Czech. J. Phys.* B21, 955 (1971).
- [11] E. I. Eknadiousiants, V. Z. Borodin, V. G. Smotrakov, V. V. Eremkin and A. N. Pinskaya, *Ferroelectrics* 111, 283 (1990).
- [12] A. Kurosaka, K. Tomomatsu, O. Nakao, S. Ajimura, H. Tominaga and H. Osanai, *J. Soc. Mater. Eng. Res.* 5, 74 (1992).

# **APPENDIX 20**

**IN SITU OBSERVATION OF DOMAINS IN  $0.9\text{Pb}(\text{Zn}_{1/3}\text{Nb}_{2/3})\text{O}_3$  -  $0.1\text{PbTiO}_3$  SINGLE CRYSTALS**

UMA BELEGUNDU, X. H. DU, L. E. CROSS AND KENJI UCHINO  
International Center for Actuators and Transducers  
Materials Research Laboratories, The Pennsylvania State University,  
University Park, PA 16802

*Abstract:* Domains in  $0.9\text{Pb}(\text{Zn}_{1/3}\text{Nb}_{2/3})\text{O}_3$  -  $0.1\text{PbTiO}_3$  or 'PZN-PT' single crystals under the application of electric field were investigated with an optical microscope. The dynamic response of the domains was studied under an electric field on PZNPT crystals is reported. In this study, electric field applied along [001]. The domain formation with the changing temperature showed the successive phase transitions from cubic to tetragonal and then to rhombohedral with decreasing temperature. The room temperature configuration showed the co-existence of both rhombohedral and tetragonal domains. Under the given experimental conditions we found that a single domain state could be induced only in the tetragonal state. Even though the temperature was lowered to  $-100^\circ\text{C}$ , complete transformation to the rhombohedral state was not observed.

Keywords: Relaxor Ferroelectric; Domain studies; Single crystals;

## INTRODUCTION

Relaxor materials such as  $\text{Pb}(\text{Zn}_{1/3}\text{Nb}_{2/3})\text{O}_3$  (PZN) and their solid solutions with  $\text{PbTiO}_3$  (PT) have come into prominence due to their very high electromechanical coupling factors  $k^{1,2}$ . In 1982, Kuwata, Uchino and Nomura discovered that poling along the [001] direction for rhombohedral crystals led to a very high value of  $k_{33}$  of 92%. Since the spontaneous polarization direction for the rhombohedral symmetry is along [111] direction, some hierarchical domain configuration is expected in the [001] poled sample. In general, the properties such as permittivity and piezoelectric properties are significantly affected by the domain motion. It is well known that the relative volume of domain orientation can be changed by the application of electric field in ferroelectrics and that these relative volumes affect the properties. In the present experiment, we have tried to understand and identify the various domains formed in the crystal under the influence of electric field. For this purpose, single crystals  $0.9\text{PZN}-0.1\text{PT}$  composition were grown in the laboratory. The domain motion due to

temperature variation with field applied along [001] direction is reported herein.

PZN, is a relaxor ferroelectric<sup>3</sup> with a broad and frequency dependent phase transition near 140 °C and PT is a regular ferroelectric with a sharp phase transition at 490 °C. PZN has rhombohedral symmetry and PT has tetragonal symmetry. The composition chosen lies at the morphotropic phase boundary of the solid solution of these two systems.

## PREPARATION OF THE SINGLE CRYSTAL SAMPLE

Single crystals of 0.9PZN- 0.1PT composition were grown by the conventional flux method. The crystallographic directions [011], [001] and [111] were determined by Laue Back Reflection method. The plate of the crystal lies in (110) plane so as to apply the field along [001] direction. The sample was then ground to a thickness of 100  $\mu\text{m}$  using SiC powder and polished to mirror finish using diamond paste. Sputtered gold electrodes were deposited and silver lead wires were connected to the sample using air dry silver paste. The surface electrode gap was 400  $\mu\text{m}$ .

The domain observation was carried out using Nikon Transmission Microscope under crossed polarizers. A temperature controlled sample stage ( Linkam ) was used to observe the domains as a function of the temperature. A VCR with the monitor connected to the microscope allowed the data to be recorded dynamically. A function generator was used to apply a triangular wave type with a frequency of 0.05 Hz ( 20 sec period ) and the maximum value of 7 kV/cm to the sample. The temperature of the crystal was changed from  $-100^{\circ}\text{C}$  to  $+250^{\circ}\text{C}$  at the rate of  $10^{\circ}\text{C}/\text{min}$ . In the figures given, the electrodes are located at top and bottom of the pictures. The plane of the picture ( plane of the crystal ) is perpendicular to [110] and [001] lies along top to bottom of the picture.

## RESULTS

The 0.9PZN-0.1PT crystal showed the co-existence of both the rhombohedral and tetragonal domains at room temperature. "Needle shaped" domains are associated with rhombohedral symmetry and the "stripe pattern" with the tetragonal domains. As the temperature was lowered to  $-37^{\circ}\text{C}$ , the needle shaped domains associated with rhombohedral symmetry emerged more clearly. Some tetragonal distortion remained at  $-100^{\circ}\text{C}$  and complete transformation to rhombohedral state was not observed probably due to spatial

## OBSERVATION OF DOMAINS IN 0.9PZN-0.1PT SINGLE CRYSTALS

composition variation in the crystal. As the sample was heated, the transition from rhombohedral to tetragonal occurred over a wide temperature range and complete tetragonal state was observed at 90° C. With increasing temperature, these tetragonal domains increased in width to 40  $\mu\text{m}$  finally disappearing at 228°C. On cooling, these domains appeared around 225°C, finally having a mixture of both tetragonal and rhombohedral domains at room temperature. The domain patterns at different temperatures, while heating are shown in Fig. 1a, 1b, 1c.

On application of the field  $\pm 7\text{kV/cm}$ , the color changes associated with the birefringence occurred at 220°C. As the temperature was reduced, no clear stripe pattern associated with tetragonal domains was observed. Rather, the whole region between the electrodes switched in uniform manner. A small number of stripes were observed near the electrodes possibly due to electrode effect. Figure 1f shows the domain pattern at 148°C with the application of the field. Figure 1c shows the clear tetragonal pattern obtained at the same temperature without field. This temperature corresponds to stable tetragonal state with the polarization direction along [001]. Since in our experiment, the field is along [001] almost monodomain tetragonal phase was achieved, providing a few number of domain walls.

On further cooling near 135° C, some interesting results were observed. As mentioned above, complete tetragonal state was observed above 90° C without the electric field. Figure 2 shows the domain formation at zero field and maximum applied field at 125° C and 85° C. Figures a and c correspond to zero field, where a domain resembling a "needle" needle shape was induced. These disappeared for the maximum value of the field (Fig 2. b and d ). The switching of these speculated rhombohedral domains took place in wave like motion. It appears that the rhombohedral phase is being induced at this temperature. Also the reduction in tetragonal domain width and the increase in their number began at this temperature. As the temperature was reduced further, these rhombohedral domains split into smaller needle shape microdomains<sup>4</sup>. This is shown in Fig. 1d. The switching of the domains continues till -25°C and freezes thereafter. Below this temperature, the rhombohedral domains increase in number.

### ACKNOWLEDGEMENTS:

The support provided by Office of Naval Research, fund N00014-91-J-4145 is gratefully acknowledged

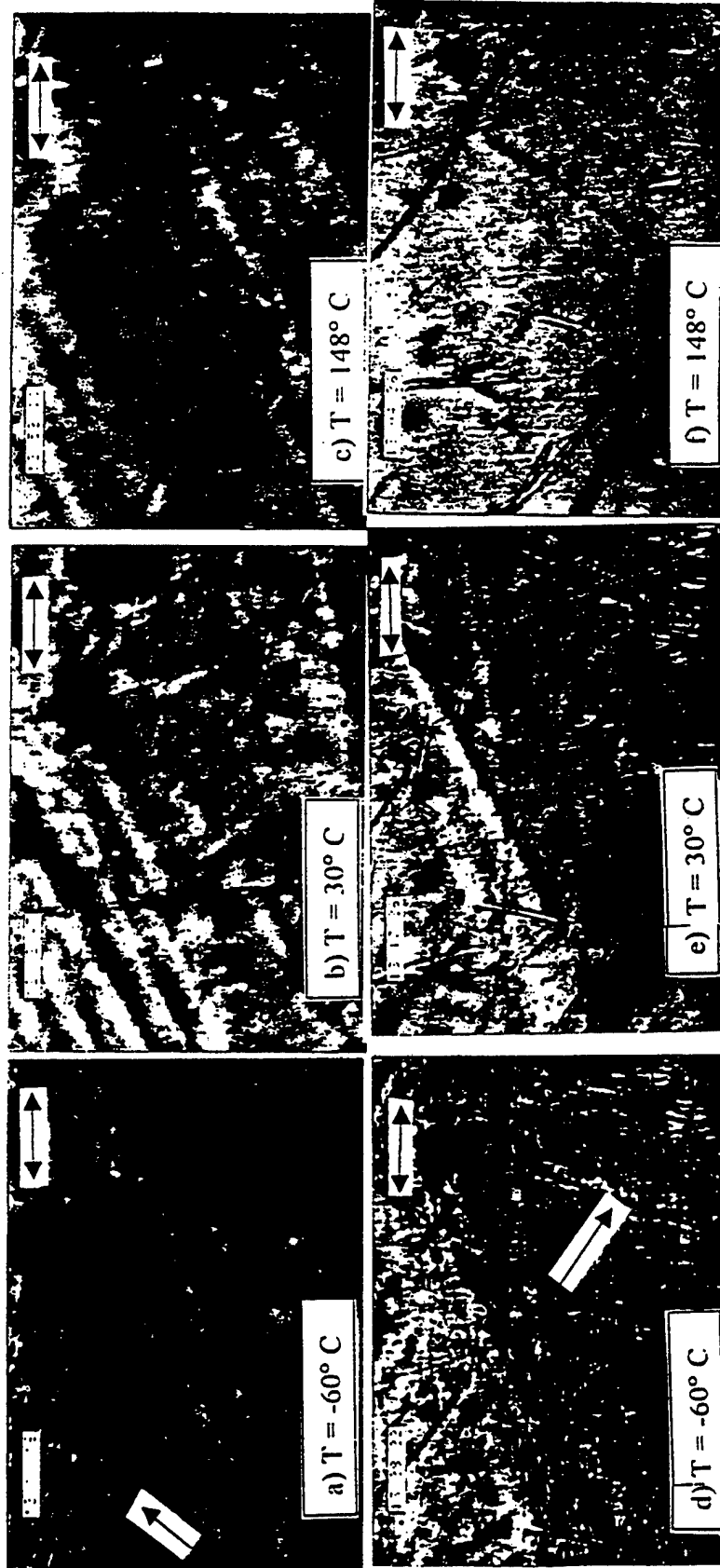


Fig. 1 Domain patterns formed with varying temperature and applied electric field. The electrodes are located at the top and bottom of the figures. Figures a), b) and c) show the domains at different without the application of the field. The rhombohedral domains are indicated by the arrow. Figures d), e) and f) show the effect of field + 7kV/cm. Monodomain state obtained by the application of field is clear in f). The bar on right top corner represents  $20\text{ }\mu\text{m}$  length. ( $\longleftrightarrow$ )

# OBSERVATION OF DOMAINS IN 0.9PZN-0.1PT SINGLE CRYSTALS

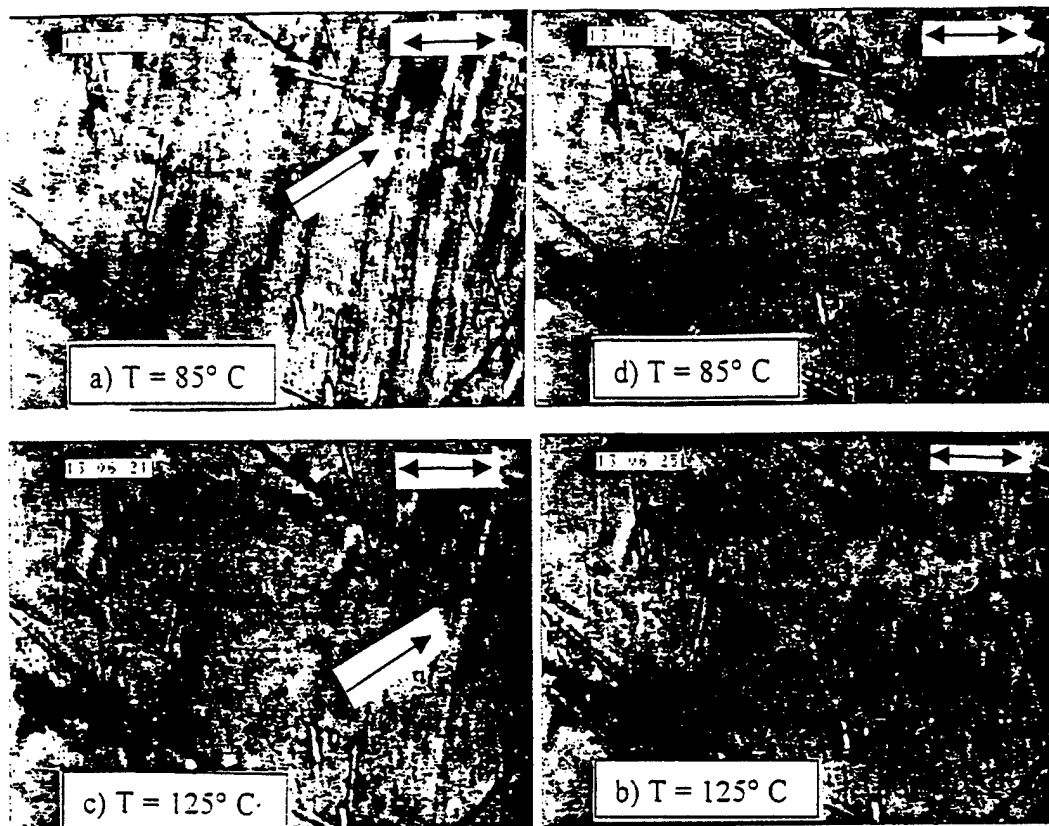


Fig. 2 Domain formation at zero field and maximum applied field of 7 kV/cm at 125° C and 85° C. Figures a) and c) correspond to zero field, where a domain resembling a "needle" needle shape was induced. ( indicated by the arrow.

## REFERENCES

- [1.] J. Kuwata, K. Uchino and S. Nomura, Ferroelectrics, v37, (1981) p579
- [2.] S. E. Park and T. R. Shrout, IEEE Transactions on Ultrasonics, Ferroelectrics and Frequency Control, (1997)
- [3.] G. A. Smolenski and A. I. Agranovskya, Sov. Phys. Sol.-State, v1, (1959) p1429
- [4.] M. L. Mulvihill, L. E. Cross and K. Uchino, J. Am Ceram. Soc., v78 (1995) p3345

# **APPENDIX 21**

# Crystal orientation dependence of piezoelectric properties of lead zirconate titanate near the morphotropic phase boundary

Xiao-hong Du, Jiehui Zheng, Uma Belegundu, and Kenji Uchino<sup>a)</sup>  
*International Center for Actuators and Transducers, Materials Research Laboratory,  
 The Pennsylvania State University, University Park, Pennsylvania 16802*

(Received 20 January 1998; accepted for publication 12 March 1998)

The piezoelectric and dielectric constants in different crystal orientations of the lead zirconate titanate (PZT) have been phenomenologically calculated for the compositions near the morphotropic phase boundary at room temperature. For a tetragonal PZT, the effective piezoelectric constant  $d_{33}$  monotonously decreases as the crystal cutting angle from the spontaneous polarization direction [001] increases. However, for a rhombohedral PZT, the effective piezoelectric constant  $d_{33[001]//}$  along the perovskite [001] direction was found to be much larger than those along the spontaneous polarization direction [111]. This crystal orientation-related enhancement is emphasized as the composition approaches the morphotropic phase boundary. This suggests that by adopting the perovskite [001] orientation with a rhombohedral composition near the morphotropic phase boundary, the piezoelectric constant  $d_{33}$  for PZT can be greatly enhanced. © 1998 American Institute of Physics. [S0003-6951(98)03619-5]

Lead zirconate titanate (PZT) thin films have high potential for microactuators, sensors, and memories.<sup>1-5</sup> In the acoustic applications, large piezoelectric constants and electromechanical coupling factors are preferred.<sup>4</sup> The preferential orientations of PZT thin films can be obtained by choosing appropriate substrate, deposition method, drying temperature, etc.<sup>6,7</sup> It was reported that the electrical properties such as dielectric constants, pyroelectric coefficient, and the P-E hysteresis could be improved by preferentially controlling the orientations.<sup>6,7</sup> The orientation dependence of piezoelectric and dielectric properties for PZT was phenomenologically calculated in our previous letter.<sup>8</sup> It was found that for tetragonal PZT 40/60 (40% PZ and 60% PT), the effective piezoelectric constant  $d_{33}$  has the maximum value in the spontaneous polarization direction [001]. However, for rhombohedral PZT 60/40, the maximum values of  $d_{33}$  and  $k_{33}$  can be obtained in the directions 56.7° and 51.3°, respectively, canted from the polarization direction [111], which are very close to perovskite [001] directions. For this composition, the  $d_{33}$  constant in the [001] orientation is about 2.5 times larger than the  $d_{33}$  in the [111] orientation (i.e., the spontaneous polarization direction). The dielectric constants have maximum values in the directions perpendicular to the spontaneous polarization for both rhombohedral and tetragonal PZT.

In this study, similar calculations to Ref. 8 have been applied for PZT, but for various compositions near the morphotropic phase boundary. The piezoelectric constants in the perovskite cubic coordinate system were calculated by using the phenomenological method developed in Ref. 9. The piezoelectric constants in any other orientations can be obtained by applying the corresponding tensor operations.<sup>8</sup> Figure 1 shows the piezoelectric constants  $d_{33}$  in the [001] and [111] orientations with respect to compositions. For tetrago-

nal PZT, the piezoelectric constant  $d_{33[001]//}$  with [001] orientation is larger than the piezoelectric constant  $d_{33[111]//}$  with [111] orientation. However, the difference between  $d_{33[001]//}$  and  $d_{33[111]//}$  is remarkably large for rhombohedral PZT. Near the morphotropic phase boundary on the rhombohedral side, the  $d_{33[001]//}$  rapidly increases while the  $d_{33[111]//}$  increases only moderately, leading to a large enhancement of  $d_{33[001]//}/d_{33[111]//}$  more than four. As a comparison, the experimental values of  $d_{33}$  for PZT ceramics from Ref. 10 are also plotted in Fig. 1. The experimental  $d_{33}$  values in the tetragonal phase are roughly half of the single crystal  $d_{33[001]//}$ , which seems to be reasonable by taking account of a random arrangement of ceramic grains in a sample as suggested by Uchida and Ikeda.<sup>11</sup> An interesting behavior can be

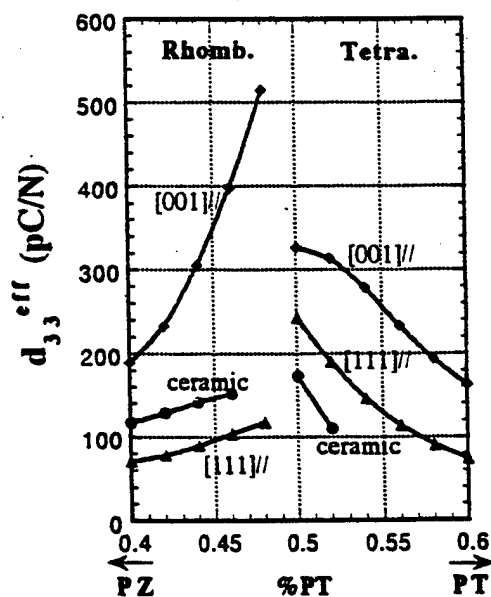


FIG. 1. Effective piezoelectric constants  $d_{33}$  of PZT with various compositions.

<sup>a)</sup>Electronic mail: kenjiuchino@psu.edu

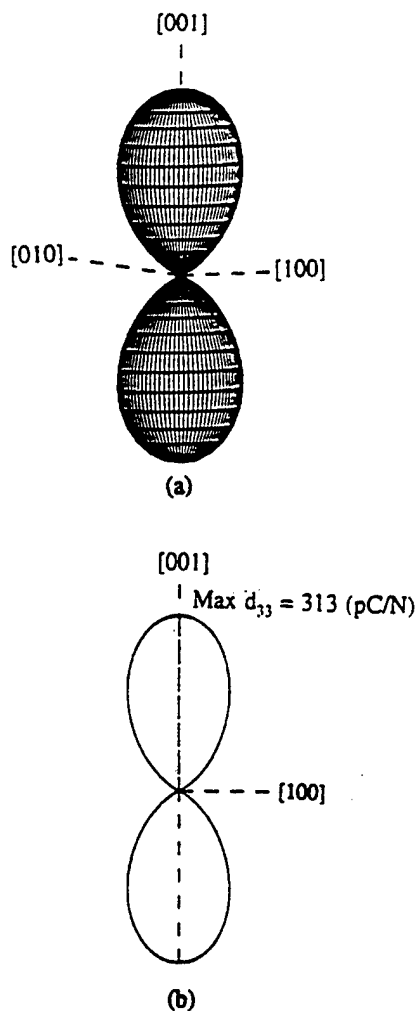


FIG. 2. (a) Effective piezoelectric constants  $d_{33}$  of tetragonal PZT 48/52. (b) The cross section curve when the figure in (a) is cut by the (010) plane.

found also in the rhombohedral phase; that is, the experimental  $d_{33}$  values are larger than the theoretical  $d_{33}[111]_{//}$ . In the rhombohedral phase, crystal orientation away from the spontaneous polarization direction  $[111]$  will enhance the effective  $d_{33}$ . Thus, even in a fully poled ceramic sample, some PZT grains canted away from the poling direction will enhance the effective  $d_{33}$ . This may explain that the experimental  $d_{33}$  values are larger than the theoretical values of  $d_{33}[111]_{//}$  that were calculated by assuming a single domain oriented along  $[111]$  in a single crystal.

To visualize the orientation dependence of  $d_{33}$ , we take tetragonal PZT 48/52 and rhombohedral PZT 52/48 as examples and plot the values of  $d_{33}$  in each orientation in Figs. 2 and 3. In these figures, the distance between the surface of the graph and the origin represents the value of  $d_{33}$  in that orientation. For tetragonal PZT,  $d_{33}$  has the maximum value in the spontaneous polarization direction  $[001]$  and monotonously decreases as the crystal cutting angle from direction  $[001]$  increases, as shown in Fig. 2. However, for rhombohedral PZT,  $d_{33}$  has the maximum value in a direction  $59.4^\circ$  away from the polarization direction  $[111]$ , as shown in Fig. 3. Similar to the PZT 60/40 as shown in Ref. 8, the directions with maximum  $d_{33}$  are very close to the perovskite  $[001]$  directions, but the ratio  $d_{33}/[001]/d_{33}/[111]$  increases to about 4 for PZT 52/48. Although we have not calculated the elec-

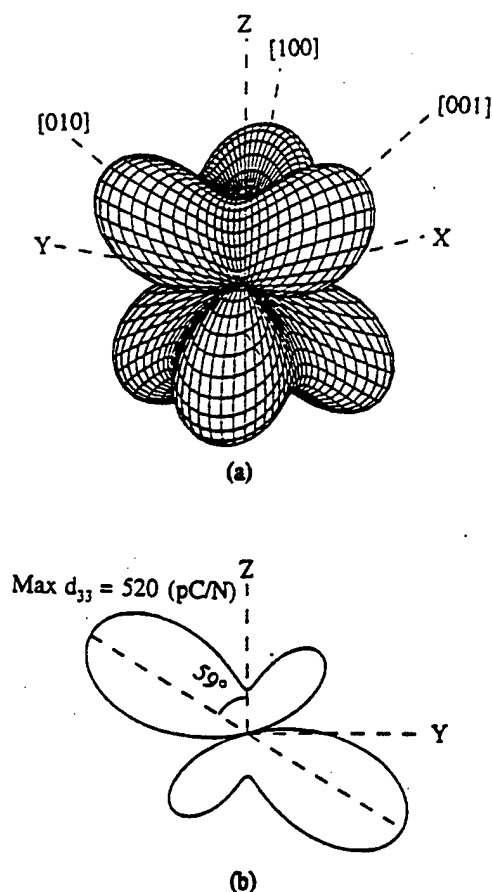


FIG. 3. (a) Effective piezoelectric constants  $d_{33}$  of rhombohedral PZT 52/48. (b) The cross section curve when the figure in (a) is cut by the Y-Z plane. The maximum value of  $d_{33}$  is on the Y-Z plane and  $59.4^\circ$  away from the Z axis.

tromechanical coupling factors  $k_{33}$  in different orientations because a complete set of elastic constant data are not available right now, we believe that the drastic increase of  $d_{33}/[001]$  will greatly enhance the values of  $k_{33}/[001]$  which should have a similar trend to  $d_{33}/[001]$ .

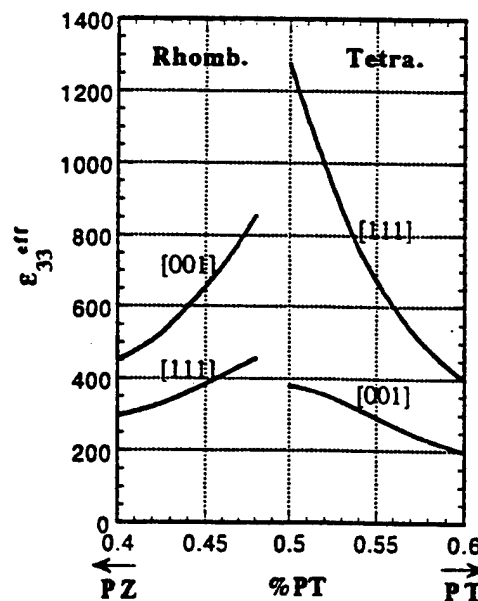


FIG. 4. Dielectric constants of PZT with various compositions.

For both tetragonal and rhombohedral phases, the dielectric constant monotonously increases as the crystal cutting angle from the spontaneous polarization direction increases.<sup>8</sup> Permittivity change ( $\epsilon_{[001]//}$  and  $\epsilon_{[111]//}$ ) with PZT composition is illustrated in Fig. 4. The dielectric constants are enhanced around the morphotropic phase boundary.

In conclusion, for tetragonal PZT, the effective piezoelectric constant  $d_{33}$  has the maximum value in the spontaneous polarization direction [001] and decreases monotonously with the crystal cutting angle from direction [001]; however, for rhombohedral PZT,  $d_{33}$  has the maximum value in a direction 59.4° away from the polarization direction [111]. As the composition approaches the morphotropic phase boundary on the rhombohedral region,  $d_{33}/\epsilon_{[001]}$  increases drastically. This suggests that PZT epitaxial thin films used for actuators and sensors should adopt rhombohedral compositions near the morphotropic phase boundary with perovskite [001] orientation. In this case, an enhancement of the effective  $d_{33}$  more than four times of the reported experimental values for the PZT films may be obtained.

The authors would like to thank the Office of Naval Research for supporting this work through Contract No. N00014-91-J-4145.

- <sup>1</sup>D. L. Polla and L. F. Francis, MRS Bull. 21, No. 7, 59 (1996).
- <sup>2</sup>M. Sakata, S. Wakabayashi, H. Goto, H. Totani, M. Takeuchi, and T. Yada, Proceedings of IEEE Micro Electro Mechanical Systems Workshop (1996) (unpublished), p. 263.
- <sup>3</sup>P. Muralt, A. Kholkin, M. Kohli, and T. Maeder, Sens. Actuators A 53, 398 (1996).
- <sup>4</sup>Y. Yamashita, Jpn. J. Appl. Phys., Part 1 33, 5328 (1994).
- <sup>5</sup>S. J. F. Scott, C. A. Araujo, H. Brett Meadows, L. D. McMillan, and A. Shawabkeh, J. Appl. Phys. 66, 1444 (1989).
- <sup>6</sup>K. Aoki, Y. Fukuda, K. Numata, and A. Nishimura, Jpn. J. Appl. Phys., Part 1 33, 5155 (1994).
- <sup>7</sup>C. J. Kim, D. S. Yoon, J. S. Lee, and C. G. Choi, J. Appl. Phys. 76, 7478 (1994).
- <sup>8</sup>X. Du, U. Belegundu, and K. Uchino, Jpn. J. Appl. Phys., Part 1 36, 5580 (1997).
- <sup>9</sup>M. J. Haun, E. Furman, S. J. Jang, and L. E. Cross, Ferroelectrics 99, 13 (1989).
- <sup>10</sup>D. A. Berlincourt, C. Cmelik, and H. Jaffe, Proc. IRE 48, 220 (1960).
- <sup>11</sup>N. Uchida and T. Ikeda, Jpn. J. Appl. Phys. 6, 1079 (1967).

# **APPENDIX 22**

# PIEZOELECTRIC PROPERTIES OF ZIRCONIUM-DOPED BARIUM TITANATE SINGLE CRYSTALS GROWN BY TEMPLATED GRAIN GROWTH

Paul W. Rehrig,\* Seung-Eek Park,\* Susan Trolier-McKinstry,\* and Gary L. Messing\*  
Beth Jones, Thomas R. Shrout\*

Materials Research Laboratory, The Pennsylvania State University, University Park, Pennsylvania 16802

Single crystals of  $\text{Ba}(\text{Zr}_x\text{Ti}_{1-x})\text{O}_3$  were grown by templated grain growth (TGG). Millimeter size single crystals of  $\text{Ba}(\text{Zr}_x\text{Ti}_{1-x})\text{O}_3$  were produced by heating a  $\text{BaTiO}_3$  crystal in contact with a sintered polycrystalline matrix of 4.5, 5.0 or 8.5 mol% Zr-doped barium titanate for 30 hours at 1350°C. To facilitate boundary migration, the ceramic compact was made 3 mol%  $\text{TiO}_2$  excess. The 4.5 and 5.0 mol% Zr-doped crystals were orthorhombic at room temperature, and for a pseudocubic (001) orientation, they showed remanent polarizations of 13  $\mu\text{C}/\text{cm}^2$  and a high field  $d_{33}$  of 340-355 pC/N. The 8.5 mol% Zr-doped crystal (again oriented along the pseudocubic (001)) was rhombohedral at room temperature with a remanent polarization of 10  $\mu\text{C}/\text{cm}^2$ . A  $k_{33}$  value of 0.74 from resonance measurements was observed for the 4.5 mol% Zr-doped crystal.

---

Based in part on the thesis submitted by Paul W. Rehrig for the Ph.D. degree in Materials Science and Engineering, Pennsylvania State University, University Park, PA 1998.

\* Membership in the American Ceramic Society

## I. Introduction

Ultrahigh electrically-induced strain levels (up to 1.7 %) were recently discovered in lead-based relaxor ferroelectric single crystals.<sup>1</sup> The composition of these perovskite crystals lies near a morphotropic phase boundary (MPB) between tetragonal and rhombohedral phases. It was found that lead zinc niobate – lead titanate and lead magnesium niobate – lead titanate rhombohedral crystals oriented and poled along the pseudocubic [001] axis had an enhanced piezoelectric response compared to [111] oriented crystals (which is the polar axis direction), which was related to an engineered domain state.<sup>1,2</sup> These enormous strain levels, coupled with the large piezoelectric constants and electromechanical coupling coefficients are extremely attractive for a variety of sensor and actuator applications. Another important result of the engineered domain state is a low level of hysteresis in the strain, at least to strain levels on the order of 0.6%. This is believed to be due to the fact that the four domain states in a poled crystal are equally favored by an applied electric field, so that there is no driving force for extensive domain wall motion. Hence, the question arises, “Is this concept of engineered domain state applicable to other ferroelectric crystals?”

Initial work on BaTiO<sub>3</sub> indicates that the concept of an engineered domain state can be applied to this system as well.<sup>3</sup> Piezoelectric coefficient,  $d_{33}$ , values up to 420 pC/N and 300 pC/N observed in orthorhombic (0°C) and rhombohedral (-100°C) crystals poled along the pseudocubic [001], appreciably higher than those measured for the tetragonal phase at room temperature (~125 pC/N), are the result of crystallographic engineering. This suggests that improved piezoelectric properties can be achieved in

non-lead based perovskite crystals if the orthorhombic or rhombohedral phase is shifted to room temperature.

It is well known that the phase transition temperatures in  $\text{BaTiO}_3$  can be altered by doping with either A or B-site substitutions.<sup>4</sup> Zirconium is one element that pinches the transition temperatures so that the rhombohedral-orthorhombic and orthorhombic-tetragonal phase transition temperatures are raised while the Curie temperature is lowered.<sup>4-6</sup> By varying the amount of dopant it is possible to stabilize either the rhombohedral and orthorhombic phases at room temperature.<sup>5,6</sup> In this work Zr-doped  $\text{BaTiO}_3$  crystals were produced and the properties of resultant crystals poled along the pseudocubic [001] direction were investigated.

Preparation of single crystals is difficult and time-consuming for many systems, including  $\text{BaTiO}_3$ . In this work, templated grain growth was used to produce crystals with Zr concentrations between 4.5 and 8.5 mol% for rapid assessment of crystals of varying composition. This chapter describes the synthesis and piezoelectric properties of Zr-doped  $\text{BaTiO}_3$  single crystals grown by TGG.

## II. Experimental Procedure

Single crystal  $\text{BaTiO}_3$  cut-offs (Lockheed Sanders Inc., Nashua, NH) were used as template crystals for TGG. The orientation of the crystals was determined by four-circle X-ray or backscattered X-ray Laue techniques. The crystals were sectioned along {001} faces using a diamond saw to sizes in the range of a few mm in size  $\times$  0.3 mm thick. One side of the template was polished with 1  $\mu\text{m}$  diamond paste.

In prior research, it was demonstrated that  $\text{BaTiO}_3$  crystals could be grown using TGG at  $1350^\circ\text{C}$ , above the eutectic temperature, with a Ti-rich initial powder.<sup>11</sup> This resulted in the formation of a liquid phase at the growth temperature that was found to accelerate the growth process. Therefore, a titanium-rich  $\text{BaTiO}_3$  powder with a proper amount of Zr was used for TGG. The powder was obtained by mixing  $\text{BaCO}_3$  ( $0.1\ \mu\text{m}$ , Sakai Chemical Co., Sakai, Japan),  $\text{TiO}_2$  ( $0.5\ \mu\text{m}$ , Ishihara Chemical Co., Kobe, Japan), and  $\text{ZrO}_2$  ( $0.05\ \mu\text{m}$ , TAM Ceramics Inc., Niagara Falls, NY) powders in a Nalgene bottle with an aqueous dispersant (Tamol, T963), and high density  $\text{ZrO}_2$  media at a pH of 10 in  $\text{DI-H}_2\text{O}$ . The slurry was milled overnight and then dried in a Pyrex pan. The powder was calcined in  $\text{O}_2$  at  $1150^\circ\text{C}$  for 4 h, followed by further heating in air at  $1200^\circ\text{C}$  for 2 h. The final powder was attrition milled for 16 h and then sieved to less than  $45\ \mu\text{m}$  (-325 mesh) prior to being mixed with an organic binder (Acryloid B-7 MEK, Rohm & Haas, Philadelphia, PA). Pellets were pressed uniaxially at 140 MPa followed by cold isostatic pressing at 276 MPa and sintering at  $1300^\circ\text{C}$ -  $1350^\circ\text{C}$  for 2 h in air. The grain size of the 4.5 and 5.0 mol% Zr-doped  $\text{BaTiO}_3$  sintered ceramics was  $\sim 15\ \mu\text{m}$  and the samples were approximately 98% of theoretical density. The grain size of the 8.5 mol% Zr-doped  $\text{BaTiO}_3$  sintered ceramics was  $\sim 25\ \mu\text{m}$  and the sample was approximately 92% of theoretical density. One side of the sintered polycrystalline matrix was polished with  $1\ \mu\text{m}$  diamond paste.

For TGG, a {100} surface of the  $\text{BaTiO}_3$  crystal was contacted, without pressure, with the sintered polycrystalline matrix and the assemblage was heated in air to  $1350^\circ\text{C}$  for 8 to 30 h. Cross sections of the growing crystal in the polycrystalline matrix were

examined by scanning electron microscopy (SEM) (ISI Model DS 130) after polishing to 1  $\mu\text{m}$  diamond paste and then thermal etching at 1300°C for 30 min.

Grown crystals were sectioned from the template and polycrystalline matrix so that dielectric measurements were performed on the grown crystals alone (i.e. none of the original  $\text{BaTiO}_3$  crystal remained). The pseudocubic  $\{001\}$  faces of grown crystals were oriented via X-ray Laue techniques and polished with 1  $\mu\text{m}$  diamond paste followed by gold-sputtering to form electrodes. A multifrequency meter (HP 4284A LCR meter) was used in conjunction with a computer controlled temperature chamber (Delta Design Inc., Model MK 9023) to measure the dielectric constant as a function of temperature on cooling (175°C to -100°C) at frequencies between 100 Hz and 100 kHz. Samples were poled either by field cooling (10 kV/cm) from temperatures above the dielectric maximum temperature ( $T_{\text{max}}$ ) or by applying 40 kV/cm at room temperature. High field measurements (1-50 kV/cm) included simultaneous polarization (P) and strain (S) hysteresis curves obtained using a computer-controlled modified Sawyer Tower system and a linear variable displacement transducer (LVDT) sensor driven by a lock in amplifier (Stanford Research Systems, Model SR830). The voltage was supplied using either a Trek 609C-6 high voltage DC amplifier or a Kepco BOP 1000M amplifier. The same system was used to measure unipolar strain curves on poled crystals oriented along the pseudocubic  $\langle 001 \rangle$ . The value for  $d_{33}$  was estimated from the slope of the unipolar strain vs. electric field (E) curve. Electromechanical coupling was measured using the IEEE resonance technique (ANSI/IEEE Std. 176-1978) on samples poled by field cooling above the Curie temperature and 10 kV/cm.

### III. Results and Discussion

Figure 1 shows a scanning electron micrograph of a cross-sectional view of the  $\text{Ba}(\text{Zr}_{0.05}\text{Ti}_{0.95})\text{O}_3$  crystal (BZT-O5.0), the template crystal, and the polycrystalline matrix after 30 h at 1350°C. The boundary migrated as much as 825  $\mu\text{m}$  into the polycrystalline matrix. Note that the crystal growth front is no longer parallel to the initial template surface, but has grown to a habit plane, as was shown previously for growth into pure  $\text{BaTiO}_3$  matrices.<sup>9,11</sup> The grown crystal also incorporated approximately 2 vol% of the matrix porosity. The average growth rate from a  $\langle 001 \rangle$  oriented template crystal after 30 h was 28  $\mu\text{m}/\text{h}$ . However, the initial growth rate may have been faster when the matrix grain size was 15  $\mu\text{m}$ . The final matrix grain size was  $22 \pm 17$   $\mu\text{m}$ , with a significant number (~10-15 vol%) with a grain size > 40  $\mu\text{m}$ . Coarsening of matrix grains is known to decrease the driving force associated with boundary migration during TGG. As indicated by the variable porosity entrapped in the crystal, the rate of growth continuously decreased with time. In the top layer of the grown crystal the pores remain abundant and ~ 5-10  $\mu\text{m}$  in size. After the growth rate slowed, fewer pores are trapped and those that remain coalesced before entrapment.

Figure 2 shows the dielectric constant (a) and dielectric loss (b) as a function of temperature and mol% zirconium at 1 kHz. The samples showed very little dispersion as a function of frequency and therefore only the 1kHz values are shown. As seen in polycrystalline Zr-doped  $\text{BaTiO}_3$ , the transition temperatures are pinched with increasing mol% zirconium.<sup>4-6,12</sup> The 4.5 (BZT-O4.5) and 5.0 (BZT-O5.0) mol% Zr samples show distinct transition temperatures with both the rhombohedral-orthorhombic and orthorhombic-tetragonal transition temperatures shifted up by approximately 80°C ( $T_{\text{R-O}}$

= 0°C) and 45°C ( $T_{O-T} = 50^\circ\text{C}$ ), respectively. The amount of shift is similar to the amount of shift (75 and 49°C, respectively) predicted by Jaffe *et al.*<sup>4</sup> for these compositions. The result of this shift is that the orthorhombic phase is stabilized at room temperature. The Curie temperature for the 4.5 and 5.0 mol% Zr samples shifted down by approximately 20°C ( $T_C = 110^\circ\text{C}$ ), also similar to the shift (21°C) shown by Jaffe *et al.*<sup>4</sup> The room temperature dielectric constants are approximately 3200 and 3500 for unpoled BZT-O4.5 and BZT-O5.0, respectively. The room temperature dielectric loss is approximately 0.013- 0.016 for both materials. What is also important to note, as clearly observed in Figure 2, is the effect of a small change of 0.5 mol% Zr doping on the pinching behavior. This shows that the small change in matrix composition was reflected in the grown crystal. Above the dielectric maximum temperature,  $T_{\max}$ , the Curie-Weiss law is obeyed with Curie constants and Curie-Weiss temperatures of  $1.4 \times 10^5^\circ\text{C}$  and  $104^\circ\text{C}$  for BZT-O4.5 and  $1.3 \times 10^5^\circ\text{C}$  and  $102^\circ\text{C}$  for BZT-O5.0, respectively; i.e.  $\epsilon_{R(BZT-04.5)} = 1.4 \times 10^5^\circ\text{C}/(T - 104^\circ\text{C})$  and  $\epsilon_{R(BZT-05.0)} = 1.3 \times 10^5^\circ\text{C}/(T - 102^\circ\text{C})$ .

Figure 3 shows the dielectric constant as a function of temperature and frequency for the crystal with 8.5 (BZT-R8.5) mol% Zr. The room temperature dielectric loss was ~0.05. The dielectric response is pinched even more than for BZT-O4.5 and BZT-O5.0 and the transition behaviors are more diffuse. The rhombohedral-orthorhombic and orthorhombic-tetragonal transition temperatures shifted up by  $135^\circ\text{C}$  ( $T_{R-O} = 55^\circ\text{C}$ ) and  $65^\circ\text{C}$  ( $T_{O-T} = 70^\circ\text{C}$ ), respectively. The rhombohedral phase is stabilized at room temperature as a result of these shifts.  $T_{\max}$  is shifted down by approximately  $43^\circ\text{C}$  ( $T_{\max} = 90^\circ\text{C}$ ). These shifts in temperature are also similar to the shifts ( $106^\circ\text{C}$ ,  $59^\circ\text{C}$ , and  $40^\circ\text{C}$ , respectively) given by Jaffe, Cook, and Jaffe.<sup>4</sup>

Figure 4 shows the polarization and strain behavior for BZT-O4.5 and BZT-O5.0 crystals oriented along the pseudocubic  $\langle 001 \rangle$  as a function of electric field at room temperature. Orthorhombic BZT-O4.5 and BZT-O5.0 crystals have remanent polarizations ( $P_r$ ) and coercive fields ( $E_c$ ) of approximately  $13 \mu\text{C}/\text{cm}^2$  and  $1 \text{ kV}/\text{cm}$ , respectively. The coercive field is lower and remanent polarizations higher<sup>5,12</sup> than reported for ceramics with similar composition, which is expected for a single crystal of this orientation. In the orthorhombic phase, the polarization vector is oriented along the pseudocubic  $\langle 110 \rangle$  direction, the magnitude of this vector is obtained by multiplying the  $P_r$  value from Figure 4 with  $\sqrt{2}$ , which results in a value of  $18 \mu\text{C}/\text{cm}^2$ .

For the Zr-doped crystals measured here, an engineered domain state with macrosymmetry  $4\text{mm}$  is expected for poling along the pseudocubic  $\langle 001 \rangle$  axis, similar to the case of rhombohedral relaxor-PT crystals<sup>1</sup>. As shown in Figure 4a, the top of the hysteresis loop is more rounded than in the case of relaxor-PT crystals. This indicates that the crystal partially depoles near zero field. The stability of the domain state was not studied.

Figure 5 shows the unipolar strain behavior at room temperature for BZT-O4.5 and BZT-O5.0 crystals poled and excited along the pseudocubic  $\langle 001 \rangle$  as a function of electric field. Both crystals show maximum strain levels of approximately  $0.48\%$  at a maximum field of  $\sim 60 \text{ kV}/\text{cm}$ , which includes  $\sim 0.35\%$  strain associated with domain reorientation. After saturation, the strain behavior from  $30\text{--}60 \text{ kV}/\text{cm}$  corresponds to a  $d_{33}$  of  $355$  and  $340 \text{ pC}/\text{N}$  for BZT-O4.5 and BZT-O5.0, respectively.

Figure 6 shows the polarization and strain behavior for  $\langle 001 \rangle$  oriented BZT-R8.5 as a function of electric field at room temperature. The larger hysteresis in the P vs. E curve (Figure 6a) relative to that for the orthorhombic crystals may be a result of inferior crystal quality, i.e. a greater volume of pores (BZT-R8.5 ~ 8 vol%, BZT-O4.5 ~ 2 vol%) and/or a higher space charge contribution to the dielectric displacement. Although  $P_r \sim 10 \mu\text{C}/\text{cm}^2$  in Figure 6a, the top of the hysteresis loop is more rounded than for orthorhombic crystals. In the rhombohedral phase, the polarization vector is oriented along the pseudocubic  $\langle 111 \rangle$  direction, the magnitude of this vector is obtained by multiplying the  $P_r$  value from Figure 6 with  $\sqrt{3}$ , which results in a value of  $17 \mu\text{C}/\text{cm}^2$ .

The unipolar strain behavior at room temperature for a  $\langle 001 \rangle$  poled rhombohedral crystal is shown in Figure 7.  $d_{33}$  calculated from the slopes of unipolar strain vs. E curves were a function of electric field, i.e.  $d_{33}$  became a maximum ( $\sim 480 \text{ pC}/\text{N}$ ) at  $\sim 10 \text{ kV}/\text{cm}$ , but decreases and subsequently saturates to  $160 \text{ pC}/\text{N}$  at  $E > 30 \text{ kV}/\text{cm}$ . The high initial value is due, at least in part, to domain reorientation. Beyond that point, as an electric field along  $\langle 001 \rangle$  prefers the tetragonal polar phase, it is possible that a modest bias field results in the transition from rhombohedral to tetragonal phase. It is noteworthy to mention that the high field  $d_{33} \sim 160 \text{ pC}/\text{N}$  is similar to that of a single domain tetragonal  $\text{BaTiO}_3$  crystal. This field-induced phase transition may be ascribed to the pinching effect, that is, the consequent decrease in free energy difference among polymorphic rhombohedral, orthorhombic, tetragonal, and cubic phases.

The electromechanical coupling data for 4.5 mol% Zr-doped orthorhombic  $\text{BaTiO}_3$  single crystal (BZT-O4.5) grown by TGG is shown in Table 1. After poling, no

resonance was observed for electromechanical coupling measurements. Under application of a 950V DC bias during the measurement the values as shown in Table 1 were obtained, showing  $k_{33}$  and  $d_{33}$  values of 0.74 and 340 pC/N, respectively. During removal of the field the values remained essentially constant down to 200V (1.0 kV/cm), also shown in Table 1. However, upon removal of all electric field, once again no resonance was detected after a few seconds. Therefore it was necessary to apply a DC bias to stabilize a domain state. The value for  $d_{33}$  is in close agreement with the value for  $d_{33}$  determined by unipolar strain data. The values for the dielectric constant and elastic compliances,  $S_{ij}^D$  (open circuited sample) and  $S_{ij}^E$  (close circuited sample), are higher than found for pure BaTiO<sub>3</sub> single crystals.

#### IV. Conclusions

In this work, single crystals of Zr-doped BaTiO<sub>3</sub> were prepared using TGG for 30 h at 1350°C. It is encouraging that TGG can be applied even in doped systems, so that the composition of the grown crystal has the same composition as the ceramic matrix. Room temperature orthorhombic (BZT-O4.5, BZT-O5.0) and rhombohedral (BZT-R8.5) crystals were successfully stabilized using 4.5-5.0 and 8.5 mol% Zr, respectively. Orthorhombic crystals exhibited a room temperature dielectric constant and dielectric loss of approximately 3500 and 0.01, as well as a remanent polarizations and coercive fields of 13  $\mu\text{C}/\text{cm}^2$  and 1 kV/cm, respectively. High field  $d_{33}$  values up to 355 pC/N were observed. This value was supported by resonance measurements, where a  $d_{33}$  value of 340 pC/N was observed. A  $k_{33}$  value of 0.74 was obtained under DC bias. The  $d_{33}$  and  $k_{33}$  values calculated for BZT-O4.5 (340-355 pC/N and 0.74, respectively) are almost

twice the value of most non-lead materials with similar  $T_{\max}$  and approaching polycrystalline PZT-5A's (DOD-type II).<sup>1</sup> Although the maximum  $d_{33}$ , as high as 480 pC/N (calculated from the S vs. E curves) for BZT-R8.5 is observed at low electric field due to domain reorientation, under additional increase in bias, the rhombohedral phase is probably converted to tetragonal due to the small energy difference between the two associated with the pinching effect. When the orthorhombic or rhombohedral phase is stabilized to room temperature to utilize crystallographic engineering for piezoelectric performance enhancement, the phase relationships and  $T_{\max}$  must be properly engineered to ensure phase stability, i.e. due to the field-induced phase transition in the rhombohedral crystals the high field measurements (field induced tetragonal phase) may not correlate well with low field measurements (rhombohedral phase). Both BZT-O and BZT-R samples show high piezoelectric coefficients and an improvement in piezoelectric properties over what is currently available for non-lead systems, as a result of crystallographic engineering.

It is possible that the properties of these crystals may be improved further. In particular, better understanding of the role of crystal orientation and phase relationships on the stability of the domain state is necessary and could lead to improved composition selection. In addition, it is possible that eliminating the porosity from the crystals would result in improved electromechanical properties.

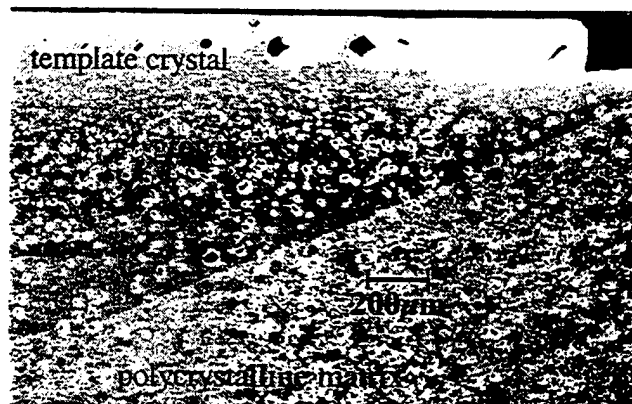
**Acknowledgement:** Financial support from the Defense Advanced Research Projects Agency on AFSOR Grant No. F49620-94-1-0428 and on ONR Grant No. N00014-98-1-0527 are gratefully acknowledged.

## References

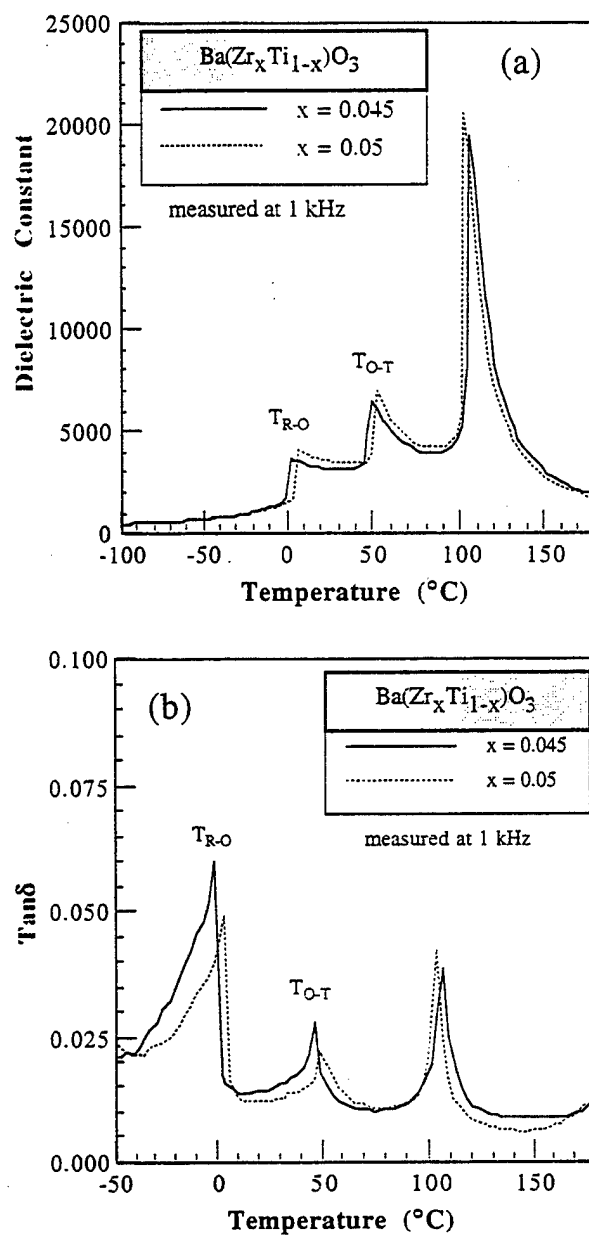
- 1) S.-E. Park and T. R. Shrout, "Ultrahigh strain and piezoelectric behavior in relaxor based ferroelectric single crystals," *J. Appl. Phys.*, **82** [4] 1804-11 (1997).
- 2) S. Wada, S.-E. Park, L. E. Cross and T. R. Shrout, "Domain Configuration and Ferroelectric Related Properties of Relaxor Based Single Crystals," *J. Kor. Phys. Soc.*, **32** [2] S1290-3 (1998).
- 3) S.-E. Park and S. Wada, "Properties of Engineered Domain State Barium Titanate Single Crystals," *In Preparation*, (1998).
- 4) B. Jaffe, W. R. Cook and H. L. Jaffe, "The Perovskite Structure"; pp. 49-114 in *Piezoelectric Ceramics*, Vol. 3, *Non-Metallic Solids*, Academic Press Ltd., New York, 1971.
- 5) D. Hennings and A. Schnell, "Diffuse Ferroelectric Phase Transitions in  $\text{Ba}(\text{Ti}_{1-y}\text{Zr}_y)\text{O}_3$  Ceramics," *J. Am. Ceram. Soc.*, **65** [11] 539-44 (1982).
- 6) R. C. Kell and N. J. Hellicar, "Structural Transitions in Barium Titanate-Zirconate Transducer Materials," *Acustica*, **6** 235-8 (1956).
- 7) S. Matsuzawa and S. Mase, "Method for Producing a Single Crystal of Ferrite," *U.S. Patent 4339301* (Jul. 13, 1982).
- 8) M. Imaeda and S. Matsuzawa, "Growth of Yttrium Iron Garnet Single Crystal by Solid-Solid Reaction," *1st Japan International SAMPE Symposium*, 419-24 (Nov. 28-Dec. 1, 1989).
- 9) T. Yamamoto and T. Sakuma, "Fabrication of Barium Titanate Single Crystals by Solid-State Grain Growth," *J. Am. Ceram. Soc.*, **77** [4] 1107-9 (1994).
- 10) T. Li, A. M. Scotch, H. M. Chan, M. P. Harmer, S. Park and T. R. Shrout, "Single Crystals of  $\text{Pb}(\text{Mg}_{1/3}\text{Nb}_{2/3})\text{O}_3$ -35 mol%  $\text{PbTiO}_3$  from Polycrystalline Precursors," *J. Am. Ceram. Soc.*, **81** [1] 244-8 (1998).
- 11) P. W. Rehrig, G. L. Messing and S. Trolier-McKinstry, "Templated Grain Growth of Barium Titanate Single Crystals," *In Preparation*, (1998).
- 12) T. R. Armstrong, L. E. Morgens, A. K. Maurice and R. C. Buchanan, "Effects of Zirconia on Microstructure and Dielectric Properties of Barium Titanate Ceramics," *J. Am. Ceram. Soc.*, **72** [4] 605-11 (1989).

## List of Figures

- Fig. 1.** Scanning electron micrograph of BaTiO<sub>3</sub> template crystal, Ba(Zr<sub>0.05</sub>Ti<sub>0.95</sub>)O<sub>3</sub> grown crystal, and the Ti-rich polycrystalline matrix Ba(Zr<sub>0.05</sub>Ti<sub>0.95</sub>)O<sub>3</sub> + 3 mole% TiO<sub>2</sub> after 30 h at 1350°C.
- Fig. 2.** Dielectric constant (a) and dielectric loss (b) as a function of temperature at 1 kHz for TGG grown Ba(Zr<sub>x</sub>Ti<sub>1-x</sub>)O<sub>3</sub> single crystals, where x = 0.045 and 0.05. (T<sub>R-O</sub> = rhombohedral to orthorhombic transition, T<sub>O-T</sub> = orthorhombic to tetragonal transition)
- Fig. 3.** Dielectric constant as a function of temperature and frequency for TGG grown Ba(Zr<sub>0.085</sub>Ti<sub>0.915</sub>)O<sub>3</sub> single crystal.
- Fig. 4.** Polarization (a) and strain hysteresis (b) as a function of electric field for <001> oriented TGG Ba(Zr<sub>x</sub>Ti<sub>1-x</sub>)O<sub>3</sub> single crystals, where x = 0.045 and 0.05.
- Fig. 5.** Unipolar strain hysteresis as a function of electric field for <001> oriented TGG Ba(Zr<sub>x</sub>Ti<sub>1-x</sub>)O<sub>3</sub> single crystals, where x = 0.045 and 0.05.
- Fig. 6.** Polarization (a) and strain hysteresis (b) as a function of electric field for <001> oriented TGG Ba(Zr<sub>0.085</sub>Ti<sub>0.915</sub>)O<sub>3</sub> single crystal.
- Fig. 7.** Unipolar strain hysteresis as a function of electric field for <001> oriented TGG Ba(Zr<sub>0.085</sub>Ti<sub>0.915</sub>)O<sub>3</sub> single crystal.
- Table 1.** Effective electromechanical coupling data for 4.5 mol% Zr-doped orthorhombic BaTiO<sub>3</sub> single crystal, oriented along the pseudocubic <001>, grown by TGG.

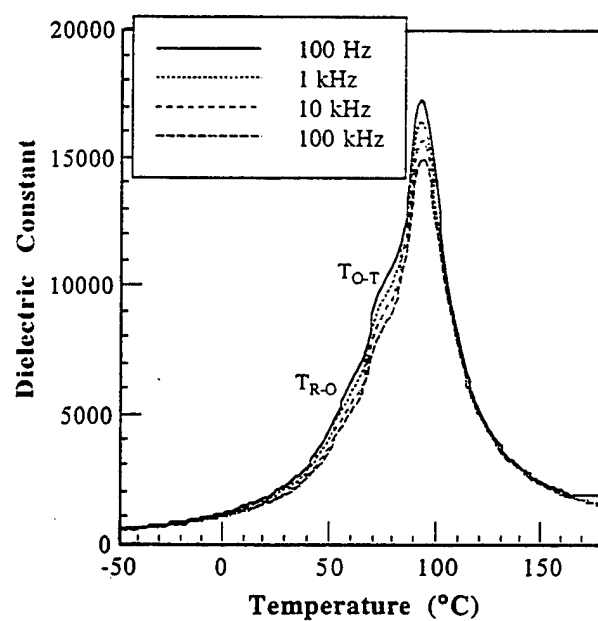


**Fig. 1** Scanning electron micrograph of  $\text{BaTiO}_3$  template crystal,  $\text{Ba}(\text{Zr}_{0.05}\text{Ti}_{0.95})\text{O}_3$  grown crystal, and the Ti-rich polycrystalline matrix  $\text{Ba}(\text{Zr}_{0.05}\text{Ti}_{0.95})\text{O}_3 + 3 \text{ mole } \% \text{ TiO}_2$  after 30 h at  $1350^\circ\text{C}$ .

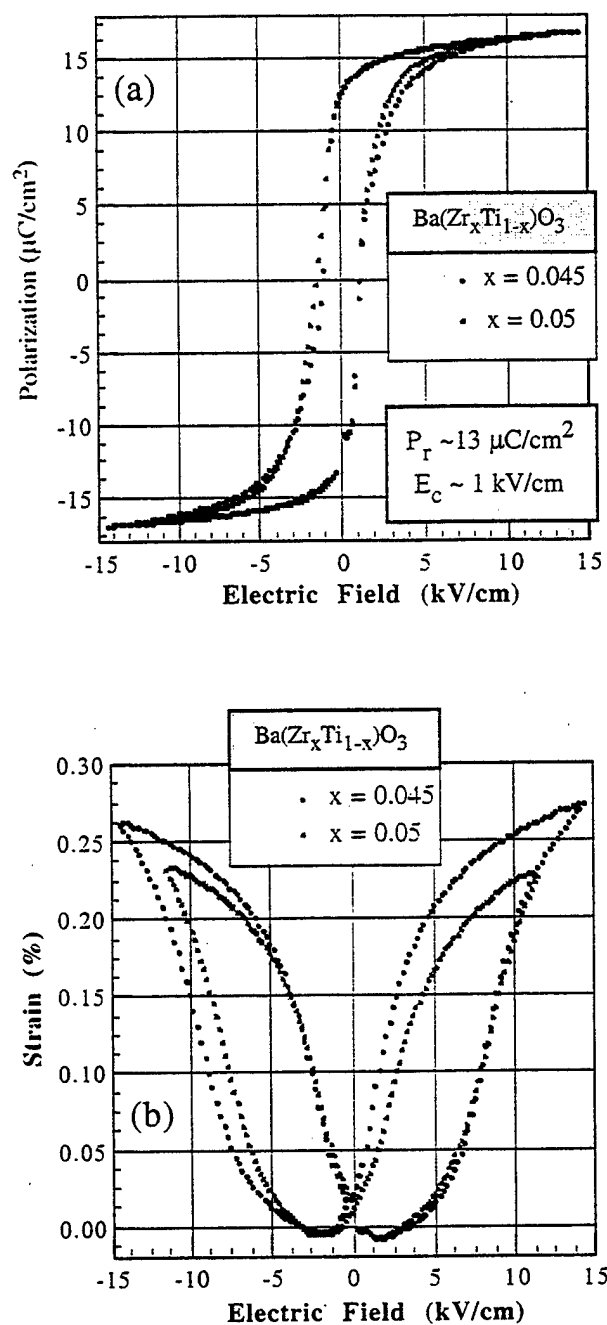


**Fig. 2**

Dielectric constant (a) and dielectric loss (b) as a function of temperature at 1 kHz for TGG grown  $\text{Ba}(\text{Zr}_x\text{Ti}_{1-x})\text{O}_3$  single crystals, where  $x = 0.045$  and  $0.05$ . ( $T_{\text{R-O}}$  = rhombohedral to orthorhombic transition,  $T_{\text{O-T}}$  = orthorhombic to tetragonal transition)

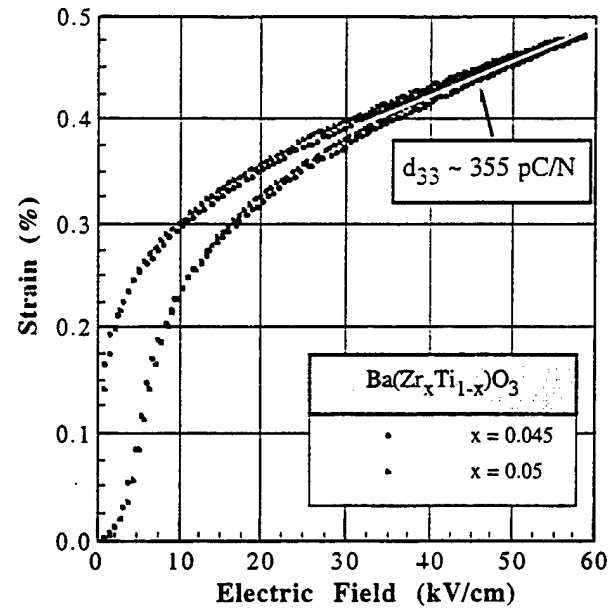


**Fig. 3** Dielectric constant as a function of temperature and frequency for TGG grown Ba(Zr<sub>0.085</sub>Ti<sub>0.915</sub>)O<sub>3</sub> single crystal.

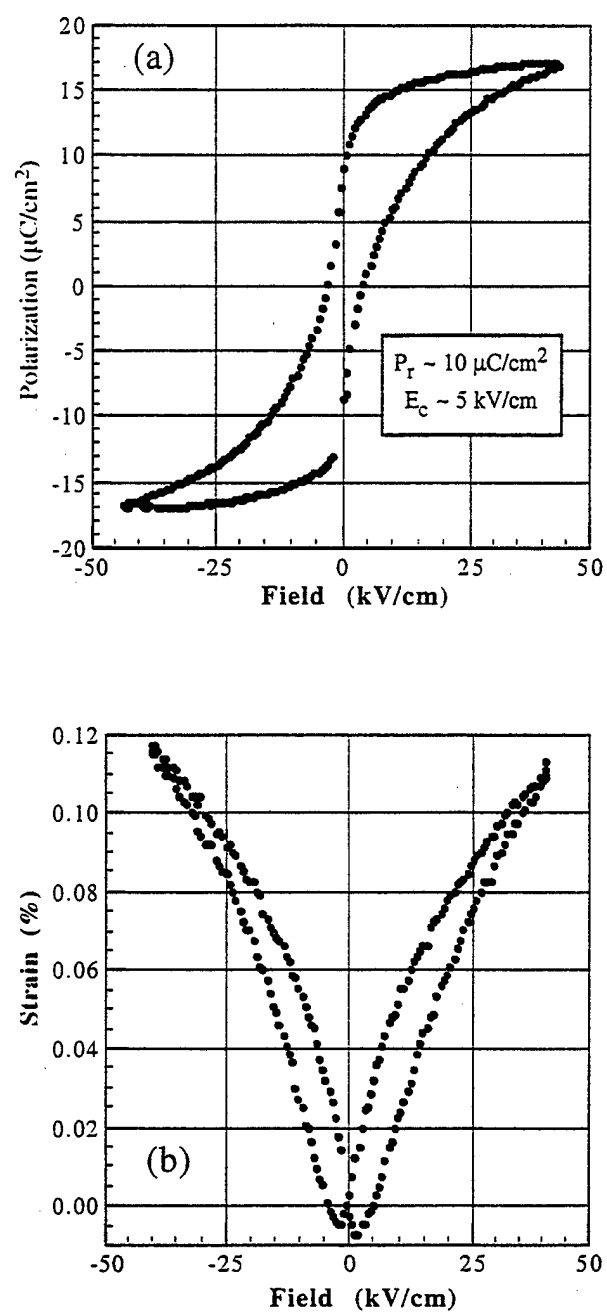


**Fig. 4**

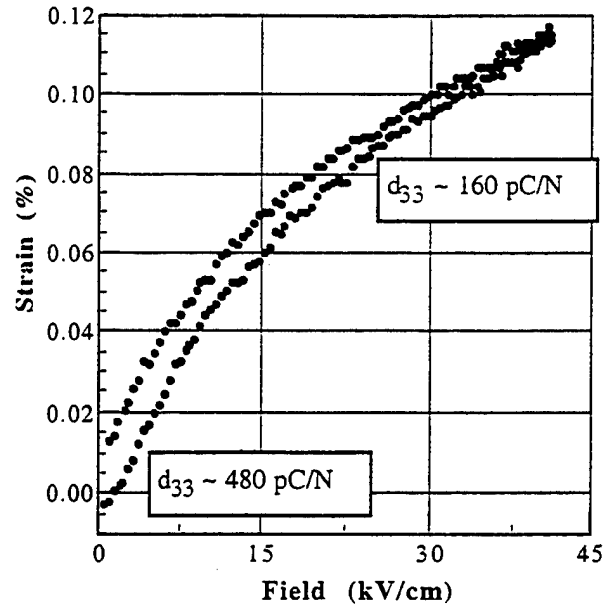
Polarization (a) and strain hysteresis (b) as a function of electric field for  $\langle 001 \rangle$  oriented TGG  $\text{Ba}(\text{Zr}_x\text{Ti}_{1-x})\text{O}_3$  single crystals, where  $x = 0.045$  and  $0.05$ .



**Fig. 5.** Unipolar strain hysteresis as a function of electric field for  $\langle 001 \rangle$  oriented TGG  $\text{Ba}(\text{Zr}_x\text{Ti}_{1-x})\text{O}_3$  single crystals, where  $x = 0.045$  and  $0.05$ .



**Fig. 6** Polarization (a) and strain hysteresis (b) as a function of electric field for <001> oriented TGG Ba(Zr<sub>0.085</sub>Ti<sub>0.915</sub>)O<sub>3</sub> single crystal.



**Fig. 7** Unipolar strain hysteresis as a function of electric field for  $\langle 001 \rangle$  oriented TGG  $\text{Ba}(\text{Zr}_{0.085}\text{Ti}_{0.915})\text{O}_3$  single crystal.

**Table 1.** Effective electromechanical coupling data for 4.5 mol% Zr-doped orthorhombic  $\text{BaTiO}_3$  single crystal, oriented along the pseudocubic  $\langle 001 \rangle$ , grown by TGG.

DC bias (kV/cm)	Freq. Constant (Hz·m)	$k_{33}$	$\epsilon_{33}^T$	$S_{33}^D$ ( $10^{-12} \text{ m}^2 \text{ N}^{-1}$ )	$S_{33}^E$ ( $10^{-12} \text{ m}^2 \text{ N}^{-1}$ )	$d_{33}$ (pC/N)
4.6	1691	0.74	770	14.5	31.7	340
1.0	1689	0.74	730	14.6	31.7	330

# **APPENDIX 23**

# **Crystal orientation dependence of piezoelectric properties of single crystal barium titanate**

Xiao-hong Du, Qing-ming Wang, Uma Belegundu, Amar Bhalla and Kenji Uchino<sup>a)</sup>

International Center for Actuators and Transducers, Materials Research Laboratory

The Pennsylvania State University, University Park, Pennsylvania 16802

## **ABSTRACT**

The dielectric and piezoelectric constants of single crystal barium titanate have been theoretically calculated and experimentally measured for different cutting directions. The dielectric constant rapidly increases as the cutting direction deviates away from the spontaneous polarization direction [001]. The effective piezoelectric strain constant  $d_{33}$  has the same trend in the range from  $0^\circ$  to  $50^\circ$  away from the polarization direction and has the maximum value more than 3.5 times larger than its value along the polarization direction. The electromechanical coupling factor  $k_{33}$  is also enhanced by choosing a cutting direction canted away from the polarization direction.

<sup>a)</sup>Electronic mail: kenjiuchino@psu.edu

## 1. Introduction

In our previous papers, the orientation dependence of piezoelectric and dielectric properties for lead zirconate titanate (PZT) has been theoretically studied.<sup>1,2</sup> It was found that for tetragonal PZT, the effective piezoelectric constant  $d_{33}$  and electromechanical coupling factor  $k_{33}$  have the maximum values along the spontaneous polarization; however, for rhombohedral PZT, the maximum values of  $d_{33}$  and  $k_{33}$  are not along the polarization, but in a direction canted from  $50^\circ$  to  $60^\circ$  away from the polarization direction. For both rhombohedral and tetragonal PZT, the dielectric constant monotonously increases as the cut-angle from the spontaneous polarization direction increases.<sup>1,2</sup>

In this paper, we theoretically and experimentally investigated the crystal orientation dependence of another important piezoelectric crystal: single crystal barium titanate (BT). Due to its large dielectric constants, barium titanate ceramics and crystals are best optional materials for capacitance and barium titanate thin films are highly potential to be used in dynamic random access memories.<sup>3</sup> However, the utilization of its piezoelectric properties has been limited because of its small piezoelectric constant along its spontaneous polarization direction [001]. Nevertheless, our recent study shows that the single crystal barium titanate has an effective piezoelectric constant  $d_{33}$  as large as 250 (pC/N), which is comparable with that of PZT, if the electrical driving direction is canted about  $50^\circ$  away from the spontaneous polarization direction [001]. These results indicate that BT may be a good substitution for PZT in some application fields where lead-contained materials are objectionable.

## 2. Theoretical Calculation

In our theoretical calculations, we used the elastic, dielectric, and piezoelectric constants measured by A. Schaefer et al.<sup>4</sup> For an arbitrary cutting orientation, the corresponding values of these constants can be obtained by performing tensor operations.<sup>5, 6</sup> The details of the

calculations have been described in Ref. 1. The calculated results are shown in Figs. 1(a) and 2(a). In these figures, the absolute values of  $d_{33}$  and  $k_{33}$  along an arbitrary direction are represented by the distance from the origin to the surface of the graph along the direction. The cross sections are also shown in Figs. 1(b) and 2(b). From these figures, we can see that the maximum values of  $d_{33}$  and  $k_{33}$  can be obtained in the directions canted  $52^\circ$  and  $47^\circ$ , respectively, away from the polarization direction. Approximately, along cubic perovskite  $[111]$  direction,  $d_{33}$  and  $k_{33}$  values are most enhanced. The  $d_{33}$  of 250 (pC/N) for this canted angle is about 3.5 times larger than the  $d_{33}$  along the polarization direction. It is interesting that the orientation dependence of  $d_{33}$  and  $k_{33}$  in BT is very different from the situation in the tetragonal PZT that always has the maximum  $d_{33}$  and  $k_{33}$  along the spontaneous polarization direction  $[001]$ . The main reason is a very large  $d_{15}$  of BT.

### 3. Experiment

For convenience, we use  $d_{33}(\theta)$  to denote the value of effective  $d_{33}$  along a direction canted an angle  $\theta$  away from the spontaneous polarization direction  $[001]$ . For example,  $d_{33}(0)$  means the value of  $d_{33}$  along  $[001]$ , and  $d_{33}(45)$  means the value of effective  $d_{33}$  along the direction canted  $45^\circ$  away from  $[001]$ . This notation is also applied to other coefficients such as dielectric constants and electromechanical coupling factors.

Barium titanate single crystals were first poled along perovskite  $[001]$  direction. Then, the following two methods were used to observe the orientation dependence of  $d_{33}$ . Method 1 is the conventional resonance method for a length-extensional bar.<sup>7</sup> Method 2 uses a  $d_{33}$ -meter to quickly check the orientation dependence of  $d_{33}$ . Method 2 cannot accurately determine the absolute values of  $d_{33}(\theta)$ , but it is an easy way to observe the distribution of  $d_{33}(\theta)$  with respect to angle  $\theta$ ; i.e. the normalized value  $d_{33}(\theta)/d_{33}(0)$  with respect to  $\theta$ .

### 3.1 Method 1

A poled single crystal of BT was cut into four small bars along the directions canted  $0^\circ$ ,  $45^\circ$ ,  $50^\circ$ , and  $60^\circ$  from the  $[001]$  direction, respectively. After the samples were polished and the electrodes were sputtered, their resonance and anti-resonance frequencies were determined with an impedance analyzer (HP4194A). Then,  $d_{33}(\theta)$ ,  $k_{33}(\theta)$ , and  $s_{33}(\theta)$  were determined from these frequencies according to the IEEE standard.<sup>7</sup> A plate normal to each direction was also cut for determining the dielectric constant. The results are shown in Table I. The values of  $\epsilon_{33}$ ,  $k_{33}$ , and  $d_{33}(\theta)/d_{33}(0)$  are also plotted in Fig. 3, 4, and 5 for comparisons.

Compared with the third column in table I (after A. Schaefer et al.), we can see that the present value of  $d_{33}(0)$  is much lower. This is probably due to the depoling during the sample processing. In order to keep all the samples in the same poling states, we did not pole them after the sample preparation. After finishing the above measurement, the sample at  $0^\circ$  cut was poled and measured again. The  $d_{33}(0)$  and  $k_{33}(0)$  were recovered up to 75.58 pC/N and 0.6, respectively. In spite of the depoling,  $d_{33}(50)$  is still much larger than the  $d_{33}(0)$  that was measured by Schaefer et al.

### 3.2 Method 2.

Figure 6 illustrates this measurement. A poled crystal of BT was polished to a cylinder with its axis perpendicular to  $[001]$ . A chart marking degrees of angles was attached to an end of the cylinder. The test probes of a  $d_{33}$ -meter were placed in the middle of the cylinder. The cylinder was rotated when  $d_{33}(\theta)$  was measured for each angle  $\theta$ , which could be read from the chart. The normalized values of  $d_{33}(\theta)/d_{33}(0)$  were plotted in Fig. 5.

## 4. Discussions and Conclusions

Figure 3 shows that the dielectric constant has its minimum value along the polarization direction and rapidly increases as the cutting angle from the spontaneous polarization direction increases. For effective  $d_{33}$ , theoretical and experimental results show that more than 3.5 time enhancement can be obtained by choosing a cutting direction canted about  $50^\circ$  from the spontaneous polarization direction [001], as shown in Fig. 5. In this direction,  $k_{33}$  is also improved (Fig. 4).

These results imply that the piezoelectric properties can be much enhanced by adopting [111] orientation for barium titanate single crystals or thin films. The [111]-oriented BT has a large  $d_{33}$  which is comparable with that of PZT. This provides another option for actuator and transducer applications, especially in some application fields where non-lead materials are desired.

#### ACKNOWLEDGEMENT

The authors gratefully acknowledge the financial support from the Office of Naval Research under contract N00014-91-J-4145.

## REFERENCES

- <sup>1</sup>X. Du, U. Belegundu, and K. Uchino, Jpn. J. Appl. Phys., Part 1 **36**, 5580 (1997).
- <sup>2</sup>X. Du, J. Zheng, U. Belegundu, and K. Uchino, Appl. Phys. Lett. **72**, 2421 (1998).
- <sup>3</sup>B. A. Baumert, J. Appl. Phys. **82**, 2558(1997)
- <sup>4</sup>A. Schaefer, H. Schmitt, and A. Dorr, Ferroelectric **69**, 253 (1986).
- <sup>5</sup>J. F. Nye, Physical Properties of Crystals (Oxford, England, 1957).
- <sup>6</sup>W. G. Cady, Piezoelectricity (Dover, New York, 1964) Vol. 1, p.65.
- <sup>7</sup>ANSI/IEEE, IEEE Standard on Piezoelectricity, Std 176-1987 (IEEE, New York, 1987).

FIG.1. (a) Effective piezoelectric constants  $d_{33}$  of single crystal Barium Titanate. (b) The cross section curve when the figure in (a) is cut by the (010) plane.

FIG.2. (a) Effective electromechanical coupling factor  $k_{33}$  of single crystal Barium Titanate. (b) The cross section curve when the figure in (a) is cut by the (010) plane.

FIG.3. Dielectric constants of single crystal Barium Titanate at different cutting angles. The solid line is obtained by calculations using the data from A. Schaefer et al, 1986.

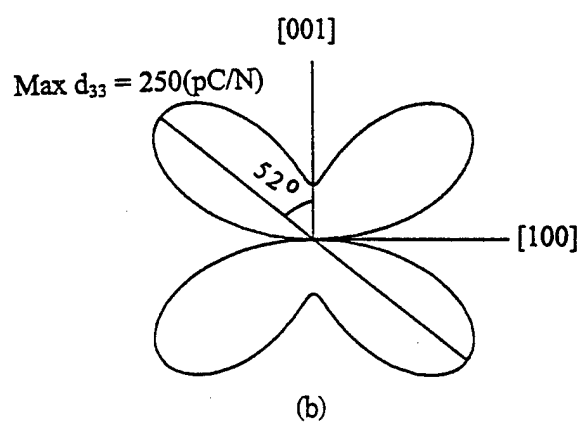
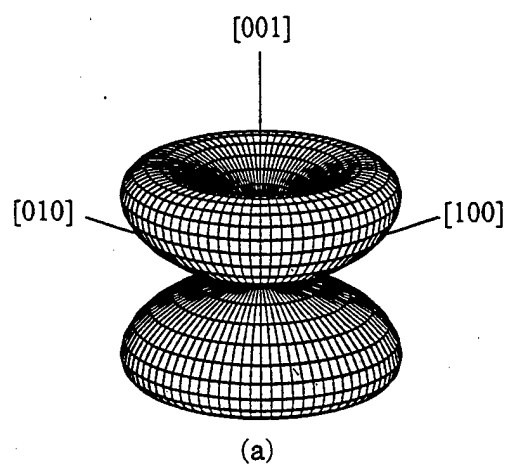
FIG.4. Effective electromechanical coupling factor  $k_{33}$  of single crystal Barium Titanate at different cutting angles.

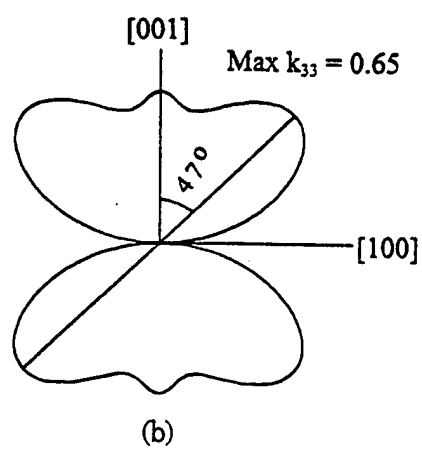
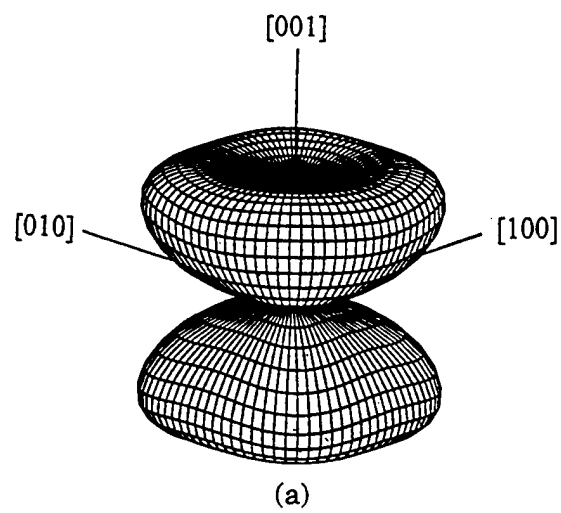
FIG.5. Effective piezoelectric constant  $d_{33}$  of single crystal Barium Titanate at different cutting angles. The values of  $d_{33}$  have been normalized by its value along the polarization direction [001]. The solid line is obtained by calculations using the data from A. Schaefer et al, 1986.

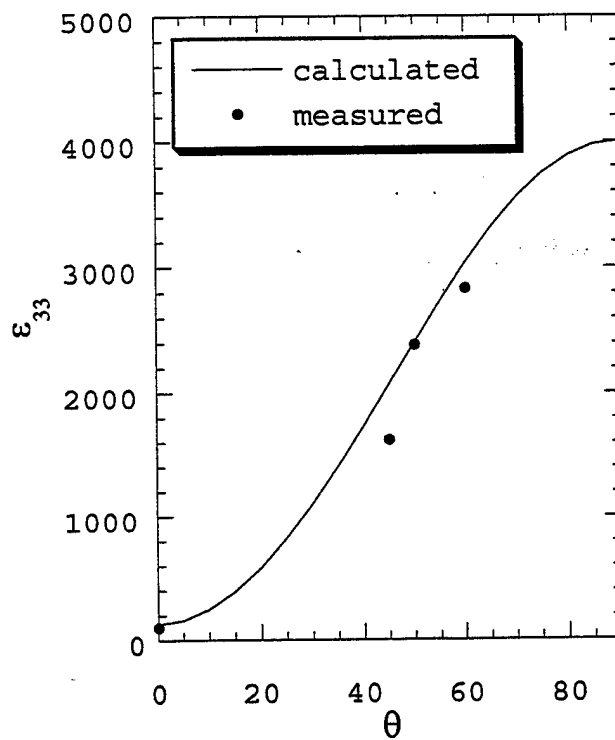
Fig. 6. Illustration of Method 2.

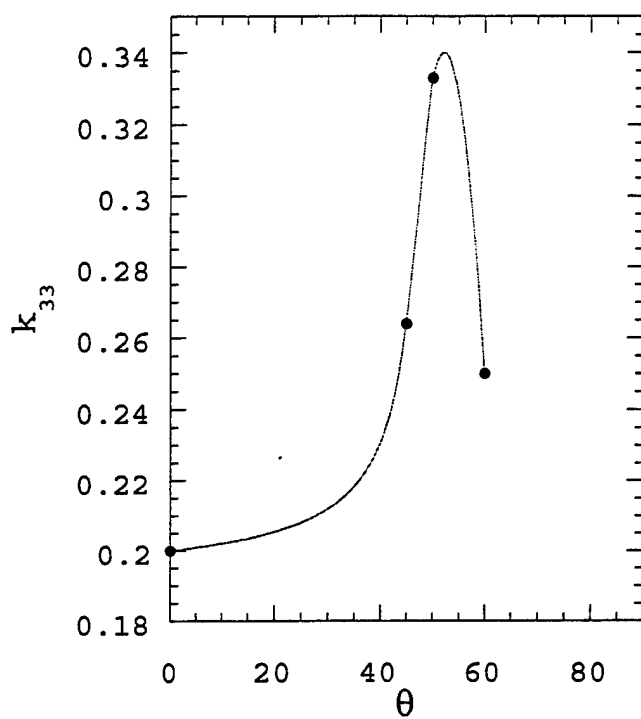
Table I Constants  $d_{33}$ ,  $k_{33}$ ,  $\epsilon_{33}$ , and  $s_{33}$  in different directions

<i>Constants</i>	$0^\circ$	$0^\circ$ (Ref. 4)	$45^\circ$	$50^\circ$	$60^\circ$
$d_{33}$ (pC/N)	24.69	68.5	85.72	129.44	95.4
$k_{33}$	0.2		0.264	0.33	0.246
$\epsilon_{33}$	103	130	1795	2873	2263
$s_{33}$ ( $\times 10^{-3}$ /Gpa)	17.56	14.95	6.63	5.94	7.47

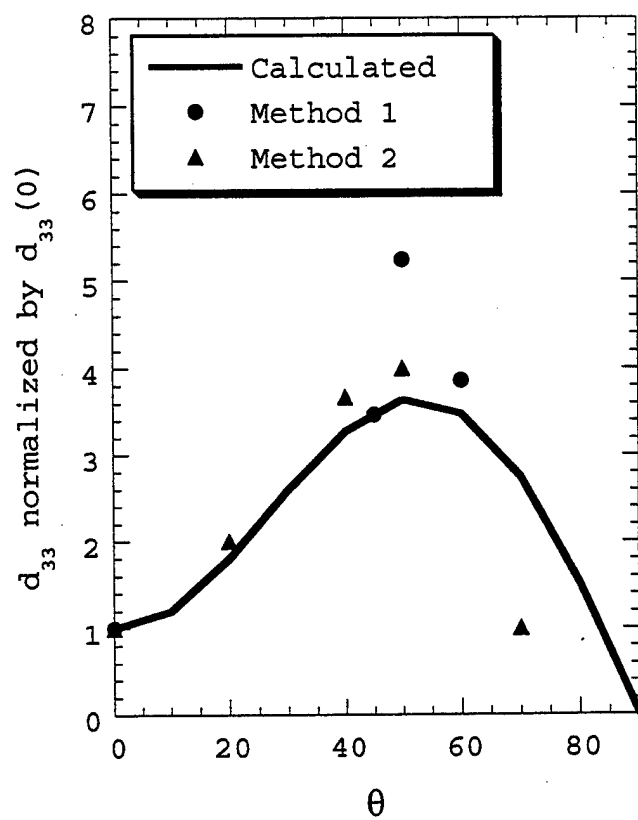


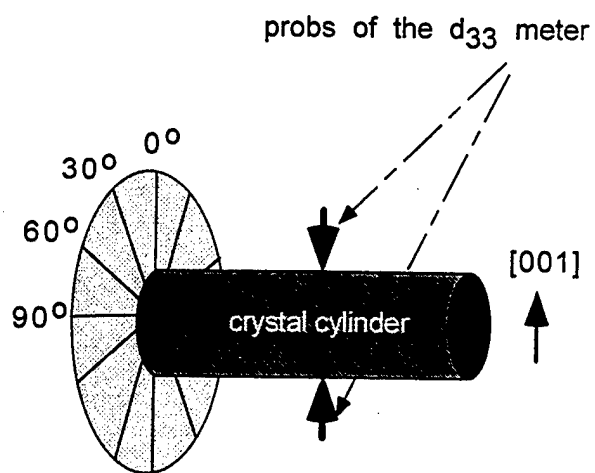






584





F 8.6

# **APPENDIX 24**

# CRYSTAL STRUCTURE ANALYSIS AND POLARIZATION MECHANISMS OF FERROELECTRIC TETRAGONAL TUNGSTEN BRONZE LEAD BARIUM NIOBATE

RUYAN GUO<sup>a</sup>, H. T. EVANS, JR.<sup>b</sup> and A. S. BHALLA<sup>a</sup>

<sup>a</sup> *Materials Research Laboratory, The Pennsylvania State University,  
University Park, Pennsylvania USA;* <sup>b</sup> *Geological Survey, United States  
Department of the Interior, Reston, Virginia, USA*

*(Received 28 February 1997; In final form 2 May 1997)*

Lead barium niobate single crystals of the composition  $\text{Pb}_{0.596}\text{Ba}_{0.404}\text{Nb}_{2.037}\text{O}_6$ , near the tetragonal: orthorhombic morphotropic phase boundary with tetragonal symmetry at room temperature, were the subject of this study. The crystallographic details, including the ionic coordination, the site occupancies and the thermal anisotropy of a lead-containing tetragonal tungsten bronze crystal are determined. This paper reports the structural refinement results, the site-preference by cations and vacancies, the macroscopic polarization properties derived from the cation displacement, and the apparent valences determined by the bonding distance. Unlike other non-lead-containing ferroelectric tungsten bronzes, significant polarization contribution can be attributed to cations ( $\text{Pb}^{2+}$  and  $\text{Ba}^{2+}$ ) at the A2-site. Large anisotropic thermal coefficients found for cations at the A2-site further strengthens the local polarization fluctuation model and suggests the local polarization components are perpendicular to the mirror plane along the  $\langle 110 \rangle$  direction.

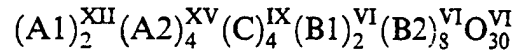
**Keywords:** Tungsten bronze lead; barium niobate

## INTRODUCTION

The tungsten bronze ferroelectric family is one of the largest oxygen octahedral ferroelectric families next to the ferroelectric perovskites. Similar to the perovskites, the ferroelectric tungsten bronzes typically have large spontaneous polarization and high dielectric constants. The structural flexibility and the chemistry versatility of this family make it more suitable

in many application aspects than the ferroelectric perovskites. Additionally, a morphotropic phase boundary (MPB) that separates two ferroelectric phases with mutually *perpendicular* polarization directions has been found so far only in tungsten bronze solid solution systems such as in  $\text{Pb}_{1-x}\text{Ba}_x\text{Nb}_2\text{O}_6$ , (PBN). Along with many optimized properties expected, it was also demonstrated that in PBN, polarization status can be controlled by applying external electric field in a crystal near the MPB composition<sup>[1]</sup> and crystals grown with proper compositions can have both the ferroelectric–ferroelectric and ferroelectric–paraelectric phase transitions in temperature span with good crystal quality and homogeneity.<sup>[2]</sup>

The prototype of all tetragonal tungsten bronzes is of point group 4/mmm. The chemical formula in an extended sense has complicated composition with the general form:



in which A1, A2, and C are the 12-, 15-, and 9-fold coordinated sites in the crystal structure surrounded by oxygen anions.<sup>[3]</sup> The  $\text{BO}_6$  octahedra are linked by their corners in such a manner as to form three (A1: square, A2: pentagonal, and C: triangular) different types of tunnels running through the structure parallel to the *c*-axis.<sup>[4]</sup> In  $\text{Pb}_{1-x}\text{Ba}_x\text{Nb}_2\text{O}_6$  the polar axis is parallel to the  $\langle 001 \rangle$  axis for the Ba-rich tetragonal phase but perpendicular to the  $\langle 001 \rangle$  for the Pb-rich orthorhombic phase.<sup>[5]</sup> The dependence of the polarization orientation on composition results in the appearance of the morphotropic phase boundary.

Determinations of ferroelectric tungsten bronze crystal structures were given by Jamieson, Abrahams, and Bernstein in their detailed structure measurements on specific compositions of SBN,<sup>[6]</sup> BNN,<sup>[7]</sup> and KLN.<sup>[8]</sup> However, precise determinations of ferroelectric tungsten bronze crystal structure for lead-containing compounds that may have polarization components in the *a-b* plane are so far lacking. To understand the ferroelectric tungsten bronzes, particularly the lead-containing families, for their relaxor behaviors (e.g., dispersive dielectric properties) at near the ferroelectric–paraelectric phase transitions,<sup>[9]</sup> or in a substantially lower temperature region,<sup>[10]</sup> knowledge of the structural details is necessary. This study was intended to fill in this gap by carrying out the crystallographic structure study on a lead containing tungsten bronze crystal, tetragonal  $\text{Pb}_{0.596}\text{Ba}_{0.404}\text{Nb}_{2.037}\text{O}_6$  (abbreviated hereafter as PBN60, or nominally,  $\text{Pb}_3\text{Ba}_2\text{Nb}_{10}\text{O}_{30}$ ).

## EXPERIMENTAL PROCEDURE

Single crystal specimens used for this study were grown by the Czochralski pulling technique, at the Materials Research Laboratory, Penn State University. Chemical composition of the crystal studied was determined by electron probe microscopical analysis as to be  $\text{Pb}_{0.596}\text{Ba}_{0.404}\text{Nb}_{2.037}\text{O}_6$ .

A tetragonal unit cell was measured from a Guinier-Hägg focused powder pattern. Precession photographs confirmed the Laue group 4/mmm with absences corresponding to a  $b$ -glide; the ferroelectric character of the crystal leads to a space group P4bm (no. 100). X-ray powder diffraction pattern was obtained on finely ground and annealed (550°C for 5 hours in air) crystal powder. The lattice parameters obtained by powder XRD after the least square fitting are  $a=b=12.502(3)$  Å,  $c=3.961(7)$  Å, and a unit cell volume of  $V = 619.2$  Å<sup>3</sup>. The measured density of the crystal is 6.13 g/cm<sup>3</sup>, comparing to the X-ray density of 6.18 g/cm<sup>3</sup>, based on its analytical formula.

The crystal chip selected was from an as grown crystal boule (without annealing) to obtain a single domain piece. A thin crystal flake, 0.3×0.3×0.03 mm in size, was selected and then mounted on the CAD4 diffractometer (Smithsonian Institution, Washington, D. C.). A total of 1148 reflections within one-quarter of the Ewald sphere with  $2\theta < 60^\circ$  were measured. These were reduced to 546 symmetry-independent structure factors, of which 506 had  $|F| > 3\sigma(F)$  (being significantly above background) and were used to refine the structure parameters.

## DATA ANALYSIS AND STRUCTURE REFINEMENT

Starting with the structure of  $\text{PbNb}_2\text{O}_6$  tungsten-bronze type, the structure was refined in space group P4bm holding  $z_{\text{Nb}_2}$  constant. Convergence was obtained at first with one Pb in site 2(a) and four Ba in site 4(c) ( $R_w = 0.10$ ). Refinement of population parameters indicated occupation 0.5 for Nb(1) and 1.0 for Ba. However, two measurements (EPMA analytical result and density measurement) clearly indicated a much higher proportion of lead in the sample.

Refinement was renewed with Pb(1) half occupied, and Ba half replaced by Pb(2). Following Brusset *et al.*<sup>[11]</sup> all the Ba is confined to the mirror-plane site. Least squares analysis continued to converge; population parameters were then released for refinement for Pb(1), Pb(2), and Ba, while position parameters for Ba were held to those of Pb(2). With anisotropic parameters

refined for Nb, Pb, and Ba,  $R_w$  reached 0.081. With O anisotropic  $R_w$  reached 0.076, but all O atoms tended to a nonpositive definite state.

It became apparent that the above procedure was not realistic. Refinement of Ba as above leads to unusual results ( $U=0.22$ ) and Pb:Ba = 5:2. The structure appears to be very "soft", that is, cross correlation and errors tend to become high. A more careful approach was followed and some basic restrictions such as Pb + Ba = 5, and that Pb:Ba = 3:2 were applied.

## REFINEMENT RESULTS AND DISCUSSIONS

Refinement with Nb and Pb anisotropic and Ba fixed to A2 with  $p=0.5$  led to  $R_w=0.085$ , but Pb:Ba = 2.87:2. With Pb:Ba fixed at 3:2 and only  $p$  for A1 refined and  $P$  for A2 adjusted to hold Pb/Ba at 3:2, with isotropic oxygen,  $R_w$  reached 0.090. This result led to occupancy of the 4-axis site of 0.551, and for the mirror-axis site 0.975. The A2 site is somewhat elongated normal to the mirror plane (Fig. 1), which suggests that the site could also be split with the atoms localized in positions to one side of the mirror. An attempt to refine such a model clearly showed that there is no concentration of electron density off the mirror plane. With split A2 atoms isotropically the model did refine but to a higher  $R$ , and anisotropically it drifted back to the elongated mirror position.

The final position coordinates and the final temperature coefficients corresponding to the best model successfully carried out referred to above are listed in Table I.

### (a) A1- and A2-Site Occupancies by Cations and Vacancies

The structure refinement results indicated that there are essentially no barium atoms in the A1-site. When an attempt was made to place barium atoms in the A1-site, the population for this site is refined to nearly zero.

The lattice parameters refined for the single crystal chip (unannealed state) are  $a=b=12.4970$  Å,  $c=3.9603$  Å, and the population of Pb in the A1-site is  $p=0.551$ . The lattice parameters found for the powder X-ray diffraction of the annealed powder, however, are  $a=b=12.5019$  Å,  $c=3.9605$  Å, and the population of Pb in the A1-site was found to be somewhat higher than  $p=0.551$  as in the case of unannealed crystal.<sup>[12]</sup> It is likely that the A1-site in the annealed state is larger than that in the unannealed state (or poled state), presumably due to the relaxation of

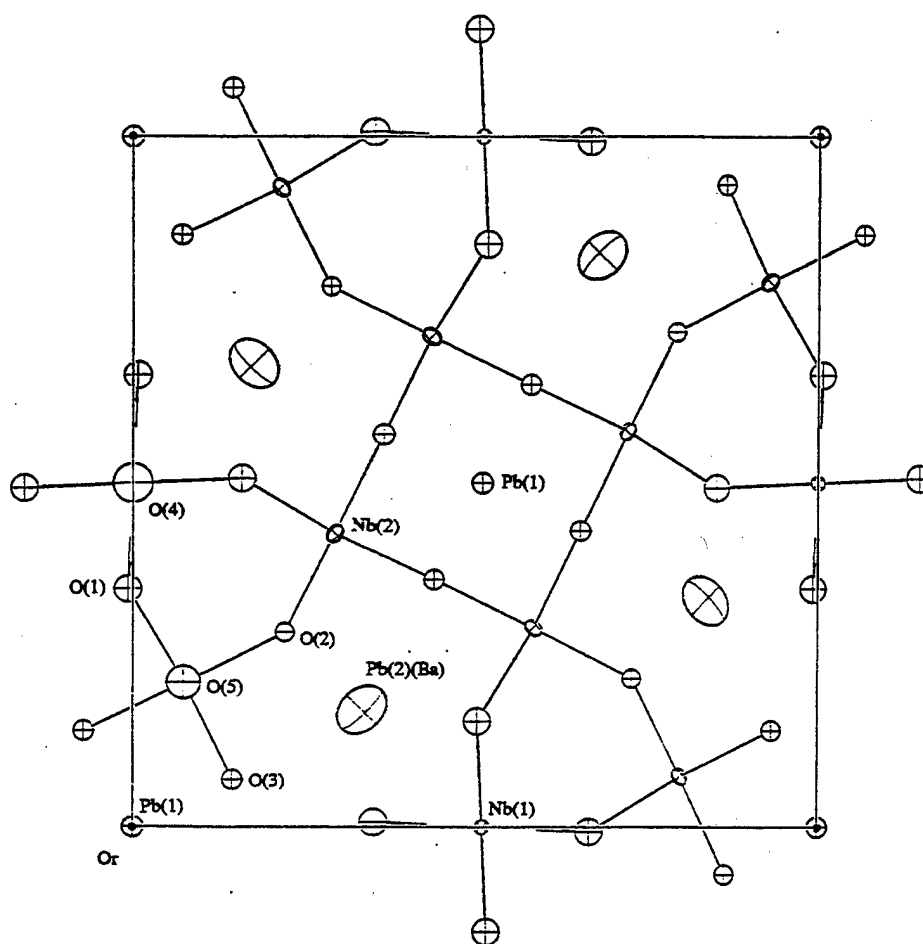


FIGURE 1 PBN60 single crystal refined structure viewed along the polar  $c$ -axis.

oxygen octahedron distortion and redistribution of vacancies after annealing that makes the A1-site more accommodate to the  $\text{Pb}^{2+}$  ions. This observation is in agreement with Trubelja *et al.* [13] that an increase in Sr occupancy in the A1-site was observed in  $\text{Sr}_{0.50}\text{Ba}_{0.50}\text{Nb}_2\text{O}_6$  upon annealing. It is a further support for the vacancy non-random distribution hypothesis proposed earlier, through an annealing and quenching effect study in tungsten bronze  $\text{Sr}_{1-x}\text{Ba}_x\text{Nb}_2\text{O}_6$  and  $\text{Ba}_{2-x}\text{Sr}_x\text{K}_{1-y}\text{Na}_y\text{Nb}_5\text{O}_{15}$  crystals. [14]

### (b) Oxygen Anisotropy

Attempts to refine oxygen anisotropically always led to a nonpositive definite result, but apparently with certain significance. An oblique view of the structure (Fig. 2) shows that the oxygen atoms are highly compressed normal to the Nb—O bonds as would be expected. Though the effect is

TABLE I Refined parameters for  $\text{Pb}_3\text{Ba}_2\text{Nb}_{10}\text{O}_{30}$ 

Populations: $2p_{\text{Pb1}} + 4p_{\text{Pb2}} + 4p_{\text{Ba}} = 5$ ; $\text{Pb}:\text{Ba} = 3:2$						
Coordinates						
Atoms	Position	<i>x</i>	<i>y</i>	<i>z</i>	<i>u</i>	<i>p</i>
Nb(1)	2b B1	0.0	0.5	-0.0089(34)	0.11(6)	1.0
Nb(2)	8d B2	0.0740(2)	0.2104(2)	0.0	0.16(8)	1.0
Pb(1)	2a A1	0.0	0.0	0.4887(26)	0.14(7)	0.551(3)
Pb(2)	4c A2	0.3287(5)	0.1713	0.4904(32)	0.26(13)	0.475
Ba	4c A2	$(x, y, z = \text{Pb}(2))$		0.30	0.500	
O(1)	8d	-0.007(1)	0.345(1)	0.048(7)	0.15(8)	
O(2)	4c	0.216(2)	0.274	0.062(7)	0.10(6)	
O(3)	8d	0.141(1)	0.070(1)	0.054(5)	0.11(6)	
O(4)	4c	0.0	0.5	0.546(24)	0.22(11)	
O(5)	8d	0.072(2)	0.211(2)	0.540(11)	0.19(19)	
Thermal Ellipsoids ( $\text{\AA}^2$ )						
Atoms	$U_{11}$	$U_{22}$	$U_{33}$	$U_{12}$	$U_{13}$	$U_{23}$
Nb(1)	0.007(1)	0.007	0.024(2)	-0.000(1)	0.0	0.0
Nb(2)	0.009(1)	0.008(1)	0.027(1)	0.002(1)	-0.007(2)	0.006(2)
Pb(1)	0.013(1)	0.013	0.030(2)	0.0	0.0	0.0
Ba/Pb(2)	0.078(2)	0.078	0.054(3)	0.021(2)	0.000(6)	0.000

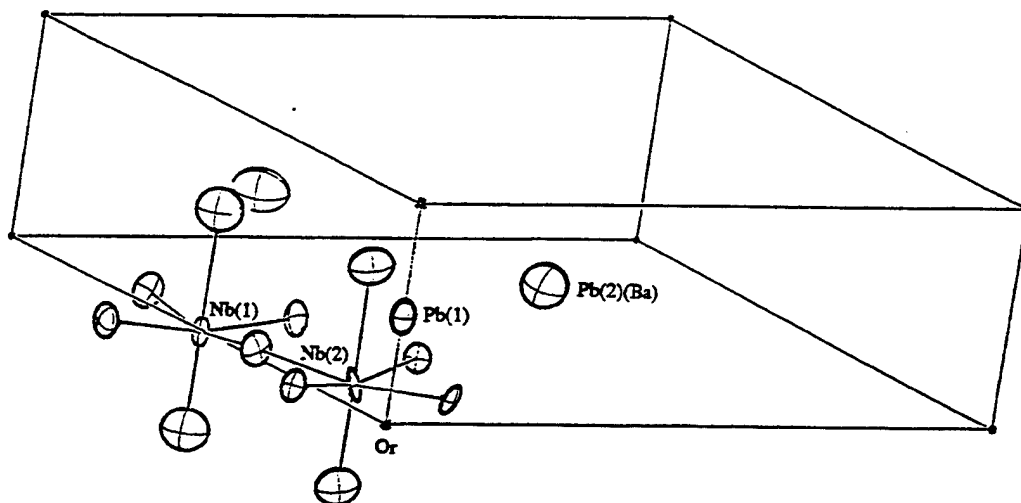


FIGURE 2 PBN60 single crystal refined structure showing oxygen anisotropy.

probably exaggerated by an inadequate absorption correction on the intensity data; nevertheless, the correction is to some degree valid as shown by the distinct improvement of  $R_w$  over conventional  $R$ . The O5 half-atom model used by Jamieson *et al.* [6] in other tungsten bronze crystals such as SBN was not adopted in this study as the isotropic temperature constants refined for O5 and O4 are within normal range.

## (c) Cation Displacement and Polarization

The final position coordinates of Table I and the lattice constants were used to calculate interatomic distances and angles, as listed in Table II.

As can be seen from the Figure 3, cations displace in the same sense away from the nearest mean plane of oxygen anions. The oxygen atoms lie close to a plane 0.2 Å below the level of the Nb atoms. The short apical Nb—O distance is 1.76(9) Å for Nb(1) and 1.82(4) Å for Nb(2), each of these sites

TABLE II Interatomic distances and angles in  $\text{Pb}_2\text{Ba}_2\text{Nb}_{10}\text{O}_{30}$ 

Distances (Å)		Angles (deg.)	
Atoms	<i>d</i>	Atoms	$\alpha$
Nb(1)—O(4)	1.76(9)	O(4)—Nb(1)—O(1)(x4)	97.7(8)
—O(1)(x4)	1.95(2)	O(1)—Nb(1)—O(1)(x4)	84.1(6)
—O(4)	2.20(9)	O(1)—Nb(1)—O(1)(x4)	94.3(6)
Nb(2)—O(5)	1.82(4)	O(4)—Nb(1)—O(4)	180.0
—O(3)	1.96(2)	O(1)—Nb(1)—O(1)(x2)	166.6(1.3)
—O(1)	1.98(2)	O(5)—Nb(2)—O(3)	96.7(9)
—O(3)	2.01(2)	O(5)—Nb(2)—O(1)	95.1(1.0)
—O(2)	2.02(2)	O(5)—Nb(2)—O(3)	95.6(9)
—O(5)	2.14(4)	O(5)—Nb(2)—O(2)	97.5(1.0)
Pb(1)—O(3)(x4)	2.61(2)	O(5)—Nb(2)—O(5)	178.8(9)
—O(5)(x4)	2.79(2)	O(3)—Nb(2)—O(1)	167.0(9)
—O(3)(x4)	2.99(2)	O(3)—Pb(1)—O(3)	89.1(6)
Ba/Pb(2)—O(2)	2.61(3)	O(3)—Pb(1)—O(2)	90.9(5)
—O(1)(x2)	2.71(3)	O(3)—Pb(1)—O(5)	84.2(8)
—O(2)	3.01(3)	O(1)—Ba/Pb(2)—O(3)	84.3(6)
—O(1)(x2)	3.02(2)	O(1)—Ba/Pb(2)—O(2)	93.0(6)
—O(4)	3.04(1)	O(1)—Ba/Pb(2)—O(5)	84.1(9)
—O(3)(x2)	3.18(2)	O(3)—Ba/Pb(2)—O(2)	166.8(1.0)
—O(5)(x2)	3.25(2)	O(3)—Ba/Pb(2)—O(5)	83.5(8)
—O(5)(x2)	3.39(2)	O(2)—Ba/Pb(2)—O(5)	83.4(1.0)
—O(3)(x2)	3.48(2)		

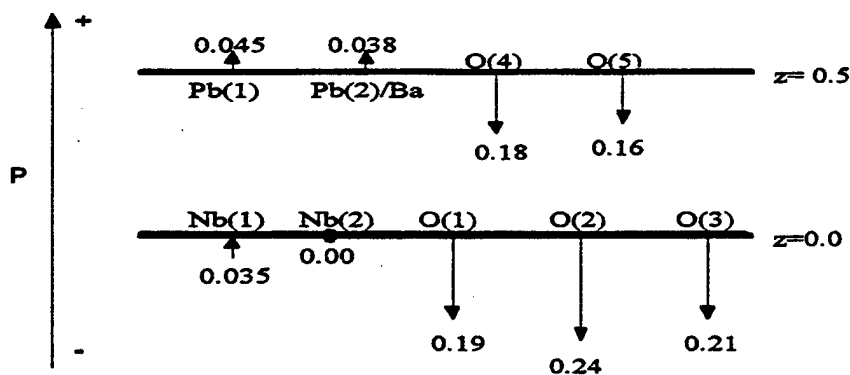


FIGURE 3 Magnitude and sense of atomic displacements (in angstroms) relative to the *c*-axis in PBN60. Macroscopic polarization is indicated by the large arrow.

possesses distorted octahedral symmetry. On average the apical distance is 1.78 Å and the opposite distance is 2.22 Å. The equatorial Nb—O distances are all near the average 1.97 Å (compared with the average distance of 2.0 Å in LiNbO<sub>3</sub> and 2.011 Å in KNbO<sub>3</sub>).

The Pb(1) coordination has *mm* symmetry and is 12-fold with Pb(1)—O distances average 2.80 Å. The Pb(2)/(Ba) environment is irregular with 15 oxygen contacts within 3.5 Å.

The direction of cation displacements can be related directly to the orientation of the macroscopic ferroelectric polarization as illustrated in the Figure 3. Note that the Nb(2) position was selected for the  $z = 0$  plane. It is known that for lead-free oxygen octahedron compounds, the displacement of Nb<sup>5+</sup> from the oxygen plane is the major contribution to the macroscopic polarization. Substantial polarization contributions in this crystal, however, can be attributed to the Pb<sup>2+</sup> and Ba<sup>2+</sup> displacements as they are of similar magnitude as that of the Nb<sup>5+</sup>.

An evaluation of the spontaneous polarization can be made based upon the knowledge of the atomic displacement. Two different approaches are compared:

- (a) From the proportionality relationship with displacement  $\Delta$  (in angstroms) developed by the "homopolar" metal atoms, the equation<sup>[15]</sup>

$$P_s = (258 \pm 9) \Delta [\mu\text{C}/\text{cm}^2] \quad (1)$$

can be used for  $P_s$  calculation for oxygen octahedra ferroelectrics, provided the ferroelectric material is of displacive type. Spontaneous polarization evaluated for the NbO<sub>6</sub> oxygen octahedra gave values  $P_s = 54.8 \sim 58.7 \mu\text{C}/\text{cm}^2$  (for Nb(1)O<sub>6</sub> group) or  $P_s = 39.8 \sim 42.7 \mu\text{C}/\text{cm}^2$  (for Nb(2)O<sub>6</sub> group). Simple weighted average of the Nb(1)- and Nb(2)-group yielded average value of  $P_s = 44.8 \sim 48.1 \mu\text{C}/\text{cm}^2$ . The calculated average values are in reasonable agreement with the experimentally determined value ( $P_s = 38 \sim 46 \mu\text{C}/\text{cm}^2$ ). It perhaps indicated that one dimensional displacive model is still suitable for this material, being consisted of the oxygen octahedra building blocks.

- (b) Assuming a point-charge model, using the expression:

$$P_s = \frac{e}{2V} \sum Z_i \Delta_i \quad (2)$$

where the summation is over the volume  $V$  containing  $i$  ions of charge  $Z_i$ , and  $\Delta_i$  is the atomic displacement vector along the polarization axis, the

total polarization taking into account each ions can be calculated. The value thus obtained is  $P_s = 41.7 \mu\text{C}/\text{cm}^2$ , compared to the experimental value.

#### (d) Apparent Valence of the Cations

The apparent valences ( $V_i$ ) of the cations for PBN60 single crystal using  $r_0$ s listed in Brown and Altermatt<sup>[16]</sup> were calculated for the refined structure. The results are summarized in Table III.

As it is clear from the Table III that the  $\text{Pb}^{2+}$  in the A2-site (15-coordination) are severely underbonded. High polarizability in the unique  $c$ -axis direction in this tetragonal structure therefore evidently includes the contribution from the largely rattling  $\text{Pb}^{2+}$  ions in the A2-site. Together with the high temperature anisotropy, the cation fluctuation in the A2-site could give dynamic polarization components perpendicular to the mirror plane, in the  $\langle 110 \rangle$  direction. With the increase of the Pb:Ba ratio, it is inevitable that more  $\text{Pb}^{2+}$  will occupy A2-site, that may aggravate the rattling status of the  $\text{Pb}^{2+}$  in the open cage until the orthorhombic structure became energetically more favored in the morphotropic phase boundary composition (Pb:  $\sim 63\%$ ). Slight overbonding is found for  $\text{Pb}^{2+}$  in the A1-site and  $\text{Ba}^{2+}$  in the A2-site. Nb(1) in B1-site is also slightly overbonded and is known to form less distorted oxygen octahedra compared to the more deformed Nb(2) in B2-site.

#### SUMMARY

Crystallographic structural refinement for a single crystal of composition  $\text{Pb}_{0.596}\text{Ba}_{0.404}\text{Nb}_{2.037}\text{O}_6$  was carried out and the results obtained allowed further understanding on the ferroelectric tungsten bronze polarization mechanisms. It is found that at Pb:Ba = 3:2 ratio, there is essentially no

TABLE III Apparent valences for cations in  $\text{Pb}_3\text{Ba}_2\text{Nb}_{10}\text{O}_{30}$

Atom	Site	Coordination	$V_i$
Nb(1)	B1	6	5.498
Nb(2)	B2	6	4.999
Pb(1)	A1	12	2.045
Ba	A2	15	2.088
Pb(2)	A2	15	1.307

$\text{Ba}^{2+}$  occupies the A1-site.  $\text{Pb}^{2+}$  cations prefer occupation of the A2-site over the A1-site as the A1-site was found nearly half vacant.  $\text{Pb}^{2+}$  in the A2-site is severely underbonded and both  $\text{Nb}^{5+}$  and  $\text{Pb}^{2+}/\text{Ba}^{2+}$  (in A2-site) are major contributors to the macroscopic polarization. Rattling  $\text{Pb}^{2+}$  in A2-site with large temperature anisotropy may cause significant polarization components normal to the mirror plane. Reduced thermodynamic energy may force the frozen of  $\text{Pb}^{2+}$  cations at one side of the mirror plane and cause local polarization components. There is no ionic concentration found away from the mirror plane at the environmental temperature.

### Acknowledgements

This research was supported partially by the National Science Foundation under Grant No. DMR-9510299. The use of facilities in the Department of Mineral Science, Smithsonian Institution, Washington, DC, is gratefully acknowledged.

### References

- [1] Guo, R., Bhalla, A. S. and Cross, L. E. (1990). *Applied Optics*, **29**, 904.
- [2] Burns, G., Dacol, F. H., Guo, R. and Bhalla, A. S. (1990). *Appl. Phys. Letters*, **57**, 543.
- [3] Hagg, G. and Magneli, A. (1954). *Rev. Pure Appl. Chem. (Australia)*, **4**, 235.
- [4] Lines, M. E. and Glass, A. M. (1977). *Principles and Applications of Ferroelectrics and Related Materials*, 280, Oxford University Press, Oxford.
- [5] Francombe, M. H. (1960). *Acta Cryst.*, **13**, 131.
- [6] Jamieson, P. B., Abrahams, S. C. and Bernstein, J. L. (1968). *J. Chem. Phys.*, **48**, 5048.
- [7] Jamieson, P. B., Abrahams, S. C. and Bernstein, J. L. (1969). *J. Chem. Phys.*, **50**, 4352.
- [8] Abrahams, S. C., Jamieson, P. B. and Bernstein, J. L. (1971). *J. Chem. Phys.*, **54**, 2355.
- [9] Guo, R., Bhalla, A. S., Randall, C. A., Chang, Z. P. and Cross, L. E. (1990). *J. Appl. Phys.*, **67**(3), 1453.
- [10] Guo, R., Bhalla, A. S., Randall, C. A. and Cross, L. E. (1990). *J. Appl. Phys.*, **67**(10), 6405.
- [11] Brusset, H., Gillier-Pandraud, H. and Mahe, R. (1972). *Bull. Soc. Chim. France*, **3**, 926.
- [12] Guo, R., Smith, D. K. *et al.* (unpublished result).
- [13] Trubelja, M. P., Ryba, E. and Smith, D. K. (1996). *J. Mat. Sci.*, **31**, 1435–1443.
- [14] Guo, R., Bhalla, A. S., Burns, G. and Dacol, F. H. (1989). *Ferroelectrics*, **93**, 397.
- [15] Abrahams, S. C., Kurtz, S. L. and Jamieson, P. B. (1968). *Phys. Rev.*, **172**, 551.
- [16] Brown, I. D. and Altermatt, D. (1985). *Acta Cryst.*, **B41**, 244–247.

# **MATERIALS STUDIES**

**New High Strain  
Polymer Materials**

# **APPENDIX 25**

## Electromechanical properties of electrostrictive poly(vinylidene fluoride-trifluoroethylene) copolymer

Xing-Zhong Zhao, Vivek Bharti, and Q. M. Zhang<sup>a)</sup>

*Materials Research Laboratory and Department of Electric Engineering, The Pennsylvania State University, Pennsylvania 16802*

T. Romotowski and F. Tito

*Naval Undersea Warfare Center, Newport, Rhode Island 02841*

R. Ting

*Department of Chemistry, University of Central Florida, Orlando, Florida 32816*

(Received 22 June 1998; accepted for publication 3 August 1998)

We report a large electrostrictive strain in electron irradiated poly(vinylidene fluoride-trifluoroethylene) copolymer at a composition with 65 mol % vinylidene fluoride, which also exhibits a large ratio of strain to applied field ( $\sim 275$  pm/V). The strain response is nearly independent of the external driving condition (unipolar or bipolar field) and does not change with temperature in about 20 °C temperature range near room temperature. Moreover, near room temperature, the material can reach a relatively high quasistatic longitudinal electromechanical coupling factor  $k_{33} \sim 0.33$ . © 1998 American Institute of Physics. [S0003-6951(98)03040-X]

Electroactive polymers with high electrostrictive strain and elastic energy density are very attractive for a broad range of actuator and transducer applications. Recently, we reported a massive electrostriction in electron irradiated poly(vinylidene fluoride-trifluoroethylene) [P(VDF-TrFE)] copolymers.<sup>1</sup> In addition, we also showed that the new material exhibits many features resembling those of relaxor ferroelectrics, that is, the slim polarization hysteresis loop at temperatures near the dielectric peak that gradually evolves into a normal ferroelectric hysteresis loop with reduced temperature, and the dispersion of the broad dielectric peak which follows the Vogel-Folcher law.<sup>1</sup> The results indicate that the electron irradiation breaks up the coherent polarization domain in normal ferroelectric P(VDF-TrFE) copolymer into nanopolar regions that transforms the material into a relaxor ferroelectric. In this letter, we will present the experimental results on electromechanical properties of irradiated P(VDF-TrFE) copolymer with 65 mol % VDF.

The copolymer was from Solvay and Cie of Bruxelles. The film used in this investigation was fabricated by melt pressing powder at 225 °C and then slowly cooled down to room temperature. The film thickness was between 20 and 40  $\mu\text{m}$ . The irradiation was carried out in an argon atmosphere with 3 MeV electrons and the dosage was in the range between 40 and 100 mrad. Several temperatures were chosen for the irradiation. The results reported in this letter were obtained from films irradiated at 120 °C with 60 mrad dosage. For the electric measurement, gold electrodes sputtered onto the film surfaces were used. It should be mentioned that in this investigation, we measured the field induced strain responses over a large group of specimens [both P(VDF-TrFE) 50/50 and 65/35 copolymers] under different processing and irradiation conditions, and it was found that the

specimen reported here possesses a relatively high ratio of induced strain/applied electric field among the specimens examined.

In this investigation, the electric field induced strain along the thickness direction (longitudinal strain) was characterized by a bimorph based strain sensor designed specifically for the polymer film strain measurement.<sup>2</sup> The polarization hysteresis loop was measured by a Sawyer-Tower circuit. The frequency range for the polarization and strain measurement is from 1 to 10 Hz. The elastic compliance was measured by a Dynamic Mechanical Analyzer in the frequency range from 1 to 100 Hz. Hence, the results presented correspond to the electromechanical performance of the material under nonresonance condition.

The induced strain level was examined under both bipolar and unipolar driving electric fields to compare the performance under these two different conditions. For an electrostrictive material, although in some actuator applications, it can be driven with a bipolar field, in most cases, the driving field will be unipolar. Hence, it is important for the material to have nearly the same performance under these two different driving conditions. Presented in Figs. 1(a) and 1(b) are the result obtained at room temperature. Clearly, the material exhibits a quite high strain level,  $\sim 3.3\%$  under a field of 120 MV/m with small hysteresis. Moreover, the strain levels under these two different driving conditions are nearly the same (the strain under unipolar driving is about 3% less than that under bipolar driving which is due to the existing small hysteresis). For comparison, the polarization hysteresis loop was also presented in Figs. 1(c) and 1(d). Apparently, there is only a small difference (about 5%) in the polarization level between the unipolar and bipolar driving, indicating that the small hysteresis at this temperature does not have marked effect on the polarization responses under different driving conditions. These results show that the material nearly recovers to its original zero field state after the applied field is

<sup>a)</sup> Author to whom correspondence should be addressed. Electronic mail: qxz1@psu.edu

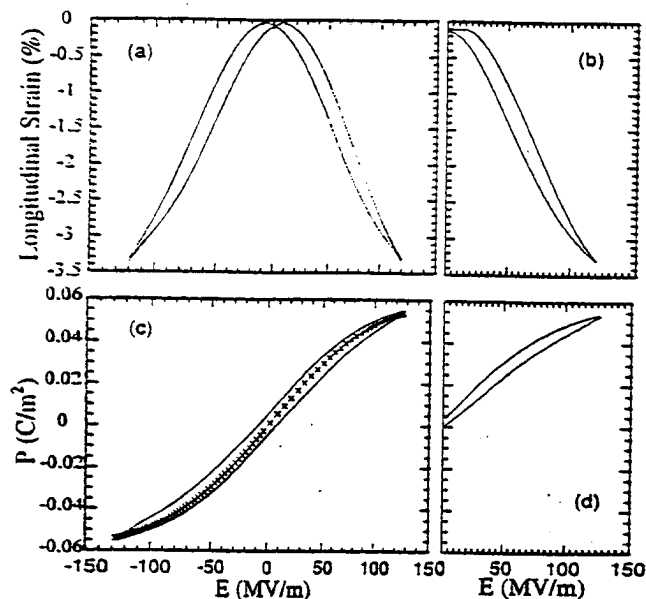


FIG. 1. The field induced strains at room temperature: (a) under bipolar driving field, (b) under unipolar driving field. The polarization hysteresis loops at room temperature: (c) under bipolar driving field, (d) under unipolar driving field. The crosses in (c) is the polarization curve fit using Eq. (2) where  $P_s = 0.063 \text{ C/m}^2$  and  $k = 1.01 \times 10^{-3} \text{ m/V}$ .

reduced to zero. Those are in sharp contrast with the behavior observed in unirradiated samples which exhibit a large polarization hysteresis and strain hysteresis.<sup>1,3</sup> In addition, there is a large difference between the responses under bipolar and unipolar electric field driving conditions.

The change of the induced strain under both unipolar and bipolar driving fields with temperature is presented in Fig. 2(a), where the temperature range is limited by the current measurement setup. The data were taken under a driving field amplitude of 120 MV/m. In comparison, the polarization with temperature under the same driving field amplitude

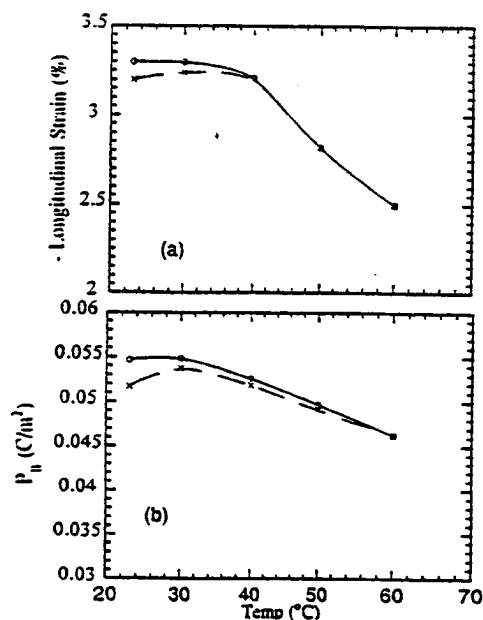


FIG. 2. (a) The induced strain and (b) the polarization as a function of temperature (open circles are under bipolar driving field and crosses are under unipolar driving field) where the driving field is 120 MV/m. The solid and dashed curves are drawn to guide eyes.

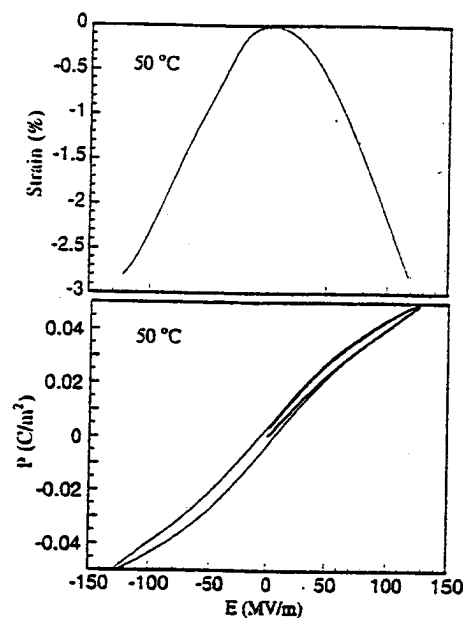


FIG. 3. (a) The strain vs applied field at 50 °C where the strains under unipolar and bipolar driving fields are the same within the instrument resolution. (b) The polarization vs applied field where the thin curve is under bipolar field and the thick curve is under unipolar field. The two curves are nearly overlapping with each.

is presented in Fig. 2(b). Apparently, as the temperature increases, the difference in the responses between unipolar field and bipolar field approaches zero. At 50 °C, the strain versus field is nearly hysteresis free as shown in Fig. 3(a) while the polarization hysteresis is still present [Fig. 3(b)] even though the polarization curve under bipolar driving field is overlapping with that under unipolar driving field. In addition, it was found that at temperatures above 50 °C, the measured "remanent polarization" (the polarization level at  $E = 0$  in the hysteresis loop) increases with temperature, an indication of increased conduction in the material. As also shown in Fig. 3(b), the polarization under the unipolar driving does not come back to zero after the field is reduced to zero. All these results suggest that the hysteresis observed in the polarization responses at 50 °C and above is mainly due to the increased conduction in the material.

Clearly, the data in Fig. 2 show that between room temperature and 40 °C, under a given driving field there is only a small change of the induced strain with temperature. Above that, the reduction becomes significant. To understand what is the response for this change of strain, the electrostrictive coefficient  $Q_{11}$  was determined from the relation  $S = Q_{11}P^2$  where  $S$  is the longitudinal strain and  $P$  is the polarization.<sup>4</sup> The result obtained is shown in Fig. 4 and as can be seen,  $Q_{11}$  in this temperature range is nearly temperature independent and has a value of about  $-12 \text{ m}^4/\text{C}^2$ . Therefore, the observed reduction of the strain with temperature for a given field is a direct consequence of the reduction of the polarization. Hence, in order to achieve the same strain level, a higher field is required at temperatures above 40 °C. It should also be pointed out that the electrostrictive coefficient obtained here is much higher than those of normal ferroelectric P(VDF-TrFE) copolymers ( $-12 \text{ m}^4/\text{C}^2$  compared with  $-2.5 \text{ m}^4/\text{C}^2$ ),<sup>3</sup> implying that the polarization

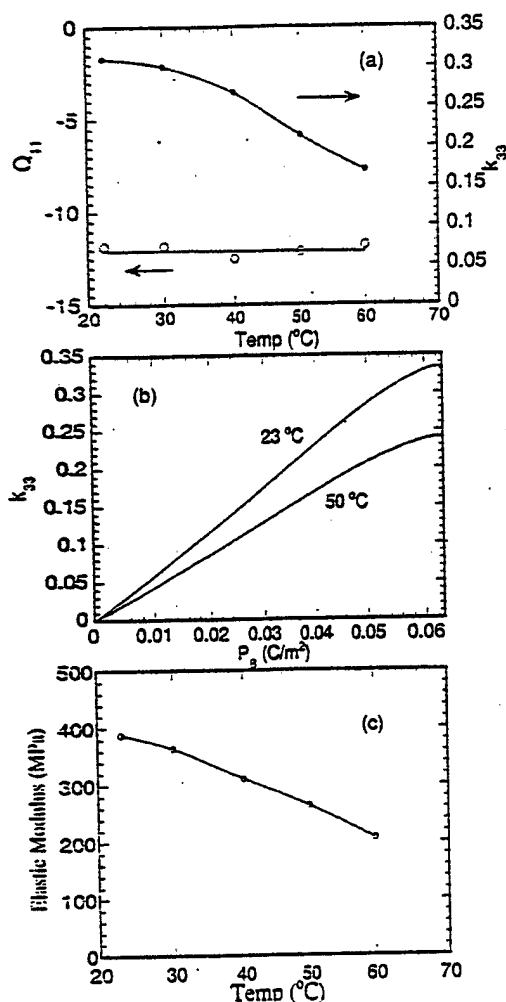


FIG. 4. (a) The electrostrictive coefficient  $Q_{11}$  (open circles) and quasistatic longitudinal electromechanical coupling factor  $k_{33}$  (filled circles) as a function of temperature under a driving field of 120 MV/m; (b) the coupling factor  $k_{33}$  as a function of the induced polarization level  $P_B$  evaluated at 23 and 50 °C based on Eq. (1) and data presented; (c) the elastic compliance as a function of temperature.

mechanism in the irradiated samples may be different from those in normal ferroelectric P(VDF-TrFE).

From the data acquired, the longitudinal electromechanical coupling factor  $k_{33}$  can be evaluated. Since the material exhibits the electrostrictive behavior, the result derived by Hom *et al.* on the quasistatic electromechanical coupling factor for electrostrictive materials is adopted here.<sup>5</sup>

$$k_{33}^2 = \frac{kQ_{11}^2 P_B^4}{s_{33}^p \left[ P_B \ln \left( \frac{P_s + P_B}{P_s - P_B} \right) + P_s \ln [1 - (P_B/P_s)^2] \right]} \quad (1)$$

where the polarization-field ( $P$ - $E$ ) relation is assumed to follow<sup>5</sup>

$$|P| = P_s \tanh(k|E|) \quad (2)$$

and  $P_s$  can be regarded as the saturation polarization and  $k$  is a constant.  $s_{33}^p$  is the elastic compliance under constant polarization. Equation (1) shows that  $k_{33}$  depends on the induced polarization level  $P_B$  and hence the driving field level. For the electrostrictive P(VDF-TrFE) copolymer here, it was found that the polarization curve can be described by Eq. (2) if the average polarization is used (to eliminate the small hysteresis) as shown in Fig. 1(c) (the cross in the figure). On the other hand, if Eq. (2) is modified to include a small coercive field  $E_c$  (on the order of 5 MV/m),  $|P| = P_s \tanh(k|E \pm E_c|)$ , it can be used to fit the data on both branches in the polarization hysteresis loop and  $P_s$  and  $k$  are nearly the same as those determined using the averaged polarization curve. In addition, it is  $s_{33}^E$  that was measured in the experiment and Eq. (1) is modified to account for that  $\{s_{33}^p = s_{33}^E [1 - (k_{33})^2]\}$ .<sup>6</sup> From the fit to Eq. (2), it was found that  $P_s$  in the experimental temperature range remains a constant of 0.063 C/m<sup>2</sup>, and the reduction in the field induced polarization with temperature is a result of reduction of the constant  $k$  in Eq. (2). Substituting these values from Eq. (2) along with the value of  $P_B$  under a field of 120 MV/m,  $Q_{11}$  and the elastic compliance [Fig. 4(c)] into Eq. (1) yields the coupling factor  $k_{33}$  (under 120 MV/m field) as also shown in Fig. 4(a). Since the coupling factor is a function of  $P_B$ , by increasing the driving field level which raises  $P_B$ ,  $k_{33}$  can be increased. As an example, the change of  $k_{33}$  with  $P_B$  is evaluated at room temperature and 50 °C and presented in Fig. 4(b). The result indicates that at room temperature, by increasing the driving field and hence raising  $P_B$  to near saturation, the quasistatic coupling factor can reach 0.33. In normal ferroelectric P(VDF-TrFE) copolymers,  $k_{33}$  is at 0.25 and even in single crystal P(VDF-TrFE) copolymer,  $k_{33}$  is still below 0.3.<sup>7-9</sup> The result here demonstrates the potential of irradiated P(VDF-TrFE) copolymer in achieving relatively high electromechanical coupling factor.

This work was supported by the Office of Naval Research through Grant No. N00014-97-1-0900 and National Science Foundation through Grant No. ECS-9710459.

<sup>1</sup>Q. M. Zhang, V. Bharti, and X. Zhao, *Science* **280**, 2101 (1998).

<sup>2</sup>J. Su, P. Moses, and Q. M. Zhang, *Rev. Sci. Instrum.* **69**, 2480 (1998).

<sup>3</sup>T. Furukawa and N. Seo, *Jpn. J. Appl. Phys., Part 1* **29**, 675 (1990).

<sup>4</sup>F. Jona and G. Shirane, *Ferroelectric Crystals* (Dover, New York, 1993).

<sup>5</sup>C. Hom, S. Pilgrim, N. Shankar, K. Bridger, M. Massuda, and S. Winzer, *IEEE Trans. Ultrason. Ferroelectr. Freq. Control* **41**, 542 (1994).

<sup>6</sup>IEEE Standard on Piezoelectricity, *ANSI/IEEE Std.* 176-1987.

<sup>7</sup>H. Wang, W. M. Zhang, L. E. Cross, and A. O. Sykes, *J. Appl. Phys.* **74**, 3394 (1993).

<sup>8</sup>K. Omote, H. Ohigashi, and K. Koga, *J. Appl. Phys.* **81**, 2760 (1997).

<sup>9</sup>H. Ohigashi and T. Hattori, *Ferroelectrics* **171**, 11 (1995).

# **APPENDIX 26**

## **Evolution of Transitional Behavior and Structure of Electron Irradiated**

### **Poly(vinylidene fluoride - trifluoroethylene) Copolymer Films.**

Vivek Bharti, G. Shanthi, H. Xu, Q. M. Zhang<sup>a</sup>  
Materials Research Laboratory, The Pennsylvania State University  
University Park, PA 16802

Kuiming Liang  
ATL Echo Ultrasound, Reedsville, PA 17084

#### **Abstract :**

The effect of high energy electron irradiation on poly(vinylidene fluoride - trifluoroethylene) (PVDF-TrFE) copolymer is investigated in a broad range of electron doses in light of a recent finding of the relaxor ferroelectric behavior and large electrostriction in the material. It is shown that although irradiation reduces both the crystalline and polar ordering, the two are not directly related to each other. In contrast to DSC and X-ray results which show that the copolymer becomes amorphous for higher irradiation dose, the dielectric data still exhibit relaxation peak which follows the Vogel-Fulcher law, indicating the presence of the local polar ordering.

PACS No. 77.65.-j, 77.80.-e, 77.22.-d, 77.84.Jd

<sup>a</sup>Corresponding author, e-mail : qxzl@psu.edu

Ferroelectric polymers have attracted much attention for the last few decades as they revealed a new aspect of polymers as functional materials. Among them, P(VDF-TrFE) copolymers have been investigated extensively because the material exhibits the highest ferroelectric polarization and electromechanical responses among the known polymers<sup>1,2</sup>. However, the electromechanical properties of P(VDF-TrFE) copolymers are still one order of magnitude smaller than those from piezoceramic materials, which severely limits their applications for electromechanical devices<sup>3</sup>. Recently, we reported<sup>4,5</sup> that under a proper high energy electron irradiation, P(VDF-TrFE) copolymers exhibited a massive electrostrictive strain (>4%) with high elastic energy density. It was also observed that a piezoelectric state can be induced in these polymers under a DC electric bias field with piezoelectric constants approaching those of the best piezoceramic materials<sup>6</sup>. In addition, the dielectric peak of irradiated films exhibited a strong frequency dispersion which followed Vogel-Fulcher (V-F) law<sup>7</sup>, an empirical law which was observed in many glass systems<sup>8</sup> and in relaxor ferroelectric ceramics<sup>9,10</sup>, suggesting that the material may belong to the relaxor ferroelectric family. In this letter, we report the experimental results on the structural evolution and transitional behavior as revealed by X-ray diffraction, dielectric, polarization and DSC data of irradiated films of P(VDF-TrFE) at 50/50 mol % composition over a broad electron irradiation dose range.

The P(VDF-TrFE) (50/50 mol%) was supplied by Solvay and Cie, Belgium and the molecular weight of the polymer is determined to be 200,000. The films were prepared by hot pressing the powder sandwiched between two aluminum foils at 215°C with a consequent slow cooling to room temperature. All the experiments were performed on the films of 25  $\mu\text{m}$  thickness. The irradiation was carried out using electrons of energy 3 MeV under the nitrogen

atmosphere at different temperatures. The dielectric data were taken in the frequency range from 30 Hz to 100 kHz, using a dielectric analyzer (TA Instruments, model 2970) in the temperature interval -60 to 125°C for a heating and cooling rate 2°C/min. The differential scanning calorimetry (DSC) measurements were carried out using a differential scanning calorimeter (TA Instruments, model 2010) at the scanning rate 10 °C/min under the nitrogen atmosphere. The X-ray pattern was taken at room temperature (20 °C) using a diffractometer (Scintag model Pad-V) with Ni filtered Cu K $\alpha$  radiation.

Figure 1 presented the dielectric constant data of un-irradiated and irradiated (from 30 to 150 Mrad) copolymer films. Consistent with the early observations<sup>4,5</sup>, the effect of irradiation is to broaden the dielectric peak and move it to near room temperature. More interestingly, all the dielectric data presented from irradiated films follow the V-F law (figures 1b and c), although the peak height drops monotonically with dosage. In addition, the freezing temperature  $T_f$  defined in the V-F law  $f=f_0 \exp[\frac{-U}{k(T_m - T_f)}]$  where  $T_m$  is the dielectric constant peak temperature,  $f$  is the frequency, and  $k$  is the Boltzman constant, does not change with irradiation dosage significantly, either. For instance, for films irradiated at 30 Mrad,  $T_f=310$  K while at 150 Mrad,  $T_f=307$  K.

In contrast, both the DSC data (figure 2) and X-ray data (figure 3) show a large change in structure and transitional behavior in the polymer as the dosage increases from 30 Mrad to 150 Mrad. In unirradiated films (figure 2a), DSC data show two well defined peaks, one at 160 °C and the other at 65 °C, corresponding to the melting and ferroelectric-paraelectric (F-P) transitions in the crystalline region, respectively<sup>11</sup>. At 30 Mrad irradiation (figure 2b), although there is no marked change in the melting peak (except a slight drop in the temperature), the peak

associated with the original F-P transition nearly disappears. Careful inspection of the data reveal that F-P transition peak becomes very broad and diffuse. When further increasing the dose to 60 Mrad, the melting peak shows a significant broadening as well as a large drop in transition temperature and transition enthalpy. At 100 Mrad, the melting peak could not be detected, indicating the disappearance of the crystalline phase in the films due to irradiation. The apparent lowering and broadening of the melting peak indicate a broad distribution in the crystallite sizes and reduction in the crystal ordering in irradiated films caused by the lattice defects, crosslinking within the crystallites and at the crystalline-amorphous interface.

It should also be noted that there is an important difference between the lattice ordering and the ferroelectric ordering. The lattice ordering is associated with the positional ordering of the monomer units while the ferroelectric ordering is from the dipolar alignment and their coupling. Hence, the ferroelectric ordering can be destroyed in a perfect lattice by random introduction of trans-gauche bonds in polymer chains (such as a paraelectric phase), while the decrease of the crystal ordering in irradiated films is caused by the lattice defects and reduction of the crystallinity due to the conversion of the crystallites to amorphous. Furthermore, local polar ordering can persist even though there is not much crystalline ordering such as observed in liquid crystals<sup>12</sup>. It is interesting to note here that although the enthalpy of the melting peak becomes zero at 100 Mrad, the enthalpy of the broad peak associated with the original P-F transition increases slightly at 100 Mrad, suggesting a slight increase of the local polar ordering in the copolymer. For films irradiated with 150 Mrad, the DSC data do not show any detectable features associated with the melting and polar order-disorder process.

We now analyze the evolution of the X-ray data with electron dose. The X-ray data were taken at 20 °C, just below the temperature of the dielectric constant maximum (about 40 °C) of

irradiated films (figure 3). As expected, the unirradiated film (figure 3a) exhibits two closely spaced peaks at 4.72 Å and 4.59 Å. The one at 4.59 Å appears due to the presence of ferroelectric  $\beta$ -phase which has an orthorhombic structure with (110) and (200) reflections nearly at the same position (pseudo-hexagonal at the plane perpendicular to the polymer chain direction). The one at 4.72 Å is from the 60° domain structure which can be reduced or eliminated by drawing or high voltage poling<sup>13</sup>. Upon 30 Mrad irradiation, only one peak is observed at the lower angle, indicating the expansion of the crystal lattice due to the introduction of trans-gauche bonds as observed in FTIR data and hence, a reduction of ferroelectric ordering<sup>14</sup>. The finding here is consistent with the polarization hysteresis measurement presented in figure 4 where the 30 Mrad irradiated films exhibit the hysteresis with a reduced remanent polarization and coercive field in comparison to unirradiated film.

Interestingly, after irradiation with 60 Mrad, the reflection peak becomes sharper and more intense in comparison with unirradiated and 30 Mrad irradiated films. The corresponding lattice spacing is equal to 4.84 Å which is close to the d spacing of the paraelectric phase of this copolymer determined from the X-ray above the Curie temperature<sup>15</sup>. Correspondingly, a slim polarization hysteresis is observed (figure 4). The FTIR measurements conducted on the same films also do not show any change in structure even when the sample was cooled down to -25°C<sup>14</sup>. The results suggest that after the irradiation the broad dielectric constant peak  $T_m$  does not correspond to the P-F phase change and macroscopically, the material is paraelectric-like even at temperatures below  $T_m$ . These results are very similar to those observed in relaxor ferroelectric ceramic and by drawing the analogy with those materials, the microstructure of irradiated P(VDF-TrFE) copolymer would be consisting of the local micro-polar regions embedded in a non-polar matrix. The increased coupling among these micro-polar regions as

the temperature is reduced results in the observed broad dielectric constant peak and freezing of the polar-regions of V-F type. It should also be pointed out that although the sharpening of the X-ray peak implies that there is an increase in the coherent length for the X-ray diffraction, which is due to the disappearance of the ferroelectric ordering and hence, domain structure, the ordering of the crystal lattice is reduced and there is a significant conversion of the crystalline phase into amorphous phase as revealed by the broad melting peak and significant reduction in the enthalpy of the melting (reduced by half in the enthalpy at this dose).

As the dose is increased further, we observed a broadening of the X-ray peak as well as a significant contribution of the intensity from a very broad peak centered at  $2\theta = 17.5^\circ$ , due to the amorphous phase. These results are consistent with the DSC and polarization data. However, in spite of significant broadening, the X-ray peak from the crystalline phase moves back towards the position of the original  $\beta$ -phase. This can be interpreted as a partial recovering to local trans bonds (polar-ordering) from trans-gauche bonds at these dose levels. The same feature was also observed in the DSC data, where the entropy of F-P transition peak shows a slight increase after 100 Mrad irradiation. Above 100 Mrad irradiation, the diffraction data become totally diffuse indicating the disappearing of the crystalline phase. However, in contrast to X-ray and DSC results, the 150 Mrad irradiated film still exhibits a V-F type dielectric constant maximum, indicating the existence of local polar-order regions and their coupling in an otherwise amorphous matrix.

All these results taken together give strong evidence that under high energy electron irradiation, P(VDF-TrFE) 50/50 copolymer is transformed from a normal ferroelectric to a relaxor ferroelectric with the existence of local polar regions. From the fitting to the V-F law, it was found that  $f_0$ , which can be regarded as the relaxation frequency of local polar regions

without much coupling with each other, increases with electron dose. At 30 Mrad,  $f_0$  is at about 1 MHz while at 150 Mrad, it becomes near 1 GHz. Such kind of increase of  $f_0$  is consistent with the decrease of the micro-polar region size with electron dose. Assuming that  $f_0$  is inversely proportional to the volume of micro-polar region, the result suggests that there is one order of magnitude reduction in the linear dimension of the micro-polar region when the dose is increased from 30 Mrad to 150 Mrad.

The authors wish to thank Z.-Y. Cheng and A. Glazounov for their fruitful discussions. The authors are also thankful to the Office of Naval Research (Grant no. N00014-97-1-0900) and National Science Foundation (Grant no. ECS-9710459) for providing the financial support to carry out this work.

## References

1. T.T. Wang, J.M. Herbert and A.M. glass, *The Applications of Piezoelectric Polymers*, (Blackie, London 1988).
2. T. Furukawa, Adv. Coll. Inter. Sci., **71-72**, 183 (1997).
3. H. Wang, Q. M. Zhang, L.E. Cross and A. O. Sykes. J. Appl. Phys., **74**, 3394 (1993).
4. Q.M. Zhang, V. Bharti and X. Zhao, Science, **280**, 2101 (1998).
5. V. Bharti, X-Z Zhao and Q.M. Zhang, Mat. Res. Innovat., **2**, 57 (1998).
6. Z-Y Cheng, V. Bharti, X. Zhao, S. Wang, T.-B. Xu and Q.M. Zhang, Intern. Symp. on Appl. of Ferroelectrics, Aug. 1998, Montreux, Switzerland.
7. H. Vogel, Z. Phys., **22**, 645 (1921); G. S. Fulcher, , J. Am. Ceram. Soc. **8**, 339 (1925).
8. Richert and Blumen, Springer-Verlag, *Disorder Effects on Relaxational Processes*, (Berlin Heidelberg 1994).
9. D. Viehland, S.J. Jang and L. E. Cross, J. Appl. Phys., **68**, 2916 (1990).
10. L.E. Cross, Ferroelectrics, **151**, 305 (1994).
11. T. Yamade, T. Ueda and T. Kitayama, J. Appl. Phys., **52**, 948 (1981).
12. H. Poths, E. Wischerhuff, R. Zentel, A. Schonfeld, G. Honn and F. Kremer, Liquid Crystals, **18**, 811 (1995).
13. G. T. Davis, T. Furukawa, A. J. Lovinger and M. G. Broadhurst, Macromolecules, **15**, 329 (1982).
14. T. Ramotowski, and F. Tito, ONR Transducer Materials and Transducer Workshop, State college, USA, May 12-14 (1998).
15. A. J. Lovinger, D. D. Davis, R. E. Cais and J. M. Kometani, Macromolecules, **21**, 78 (1988).

### Figure Captions

Figure 1: (a) The dielectric constant measured at 1 kHz as a function of temperature for P(VDF-TrFE) 50/50 mol% copolymer films, unirradiated and irradiated at 120°C for different doses. Relationship between the measurement frequency and the temperature of the dielectric constant maximum for two irradiation doses; (b) 30 Mrad and (c) 150 Mrad, points show experimental data, and the lines correspond to fit the Vogel-Fulcher law.

Figure 2 : DSC thermogram of P(VDF-TrFE) 50/50 mol% copolymer (a) unirradiated, and irradiated at 120°C for (b) 30 Mrad, (c) 60 Mrad, (d) 80 Mrad, (e) 100 Mrad, and (f) 150 Mrad doses.

Figure 3 : The X-ray diffraction pattern of P(VDF-TrFE) 50/50 mol% copolymer films, (a) unirradiated, and irradiated at 120°C using (b) 30 Mrad, (c) 60 Mrad, (d) 80 Mrad, (e) 100 Mrad, and (f) 150 Mrad doses. The arrows indicate the position of the broad peak corresponding to the amorphous phase in the copolymer.

Figure 4: Change in the polarization hysteresis loop with irradiation dose for P(VDF-TrFE) 50/50 mol% copolymer films irradiated at 120°C.

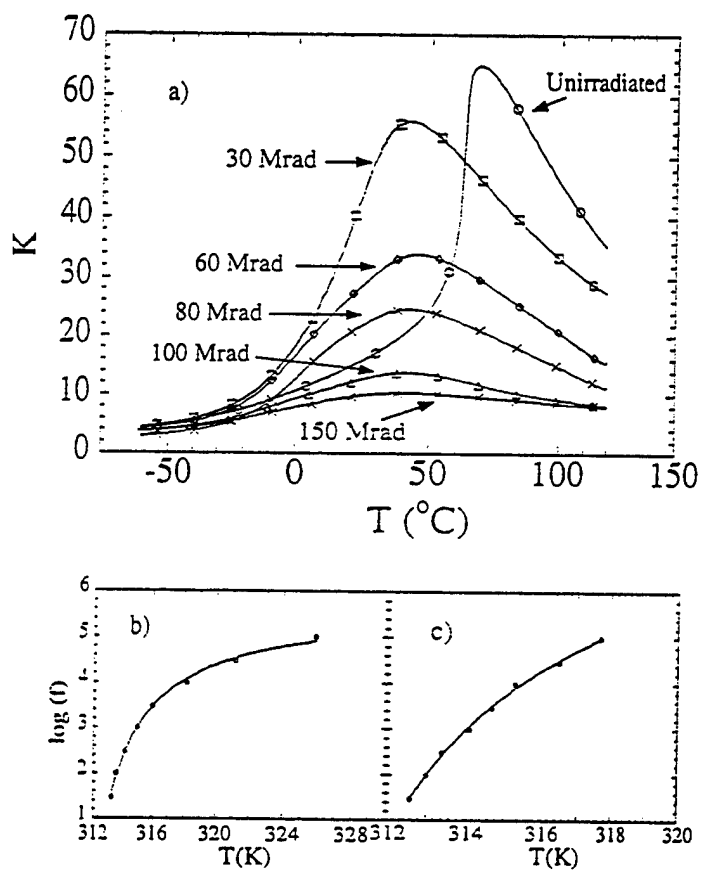


Figure 1, Vivek Bharti et al.

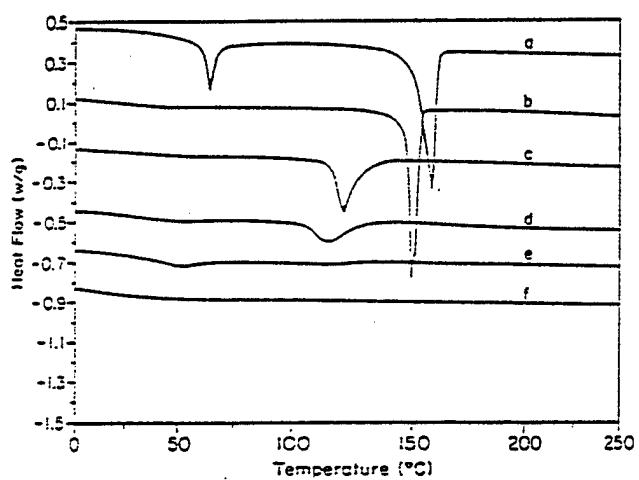


Figure 2, Vivek Bharti et. al

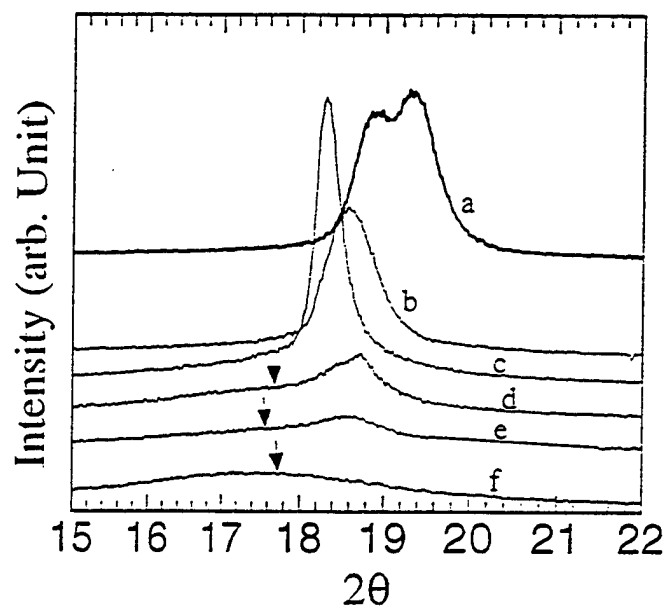


Figure 3 , Vivek Bharti et. al

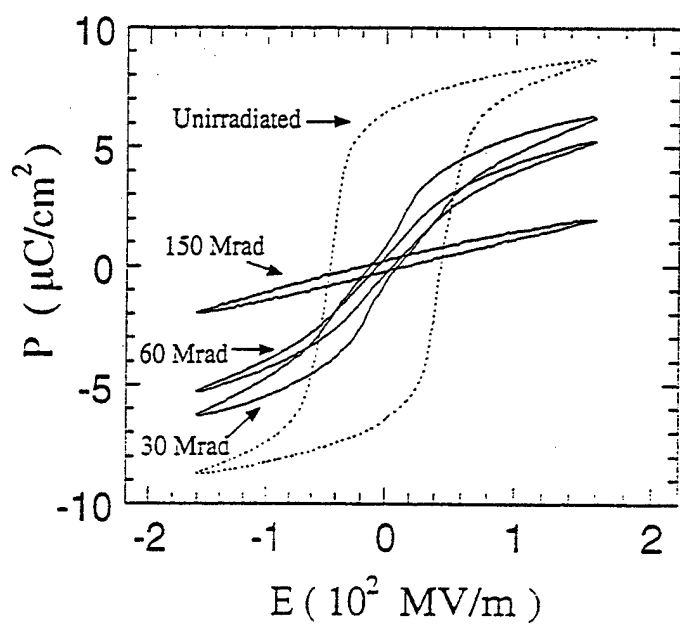


Figure 4, Vivek Bharti et. al.

# **APPENDIX 27**

# Transverse Strain Responses in Electrostrictive Poly(vinylidene fluoride-trifluoroethylene)

Films and Development of a Dilatometer for the Measurement

Z.-Y. Cheng, Vivek Bharti, T. B. Xu, Shexi Wang, and Q. M. Zhang<sup>a</sup>

Materials Research Laboratory, The Pennsylvania State University

University Park, PA 16802

T. Ramotowski and F. Tito

Naval Undersea Warfare Center, Newport, Rhode Island 02841

R. Ting

Chemistry Department, University of Central Florida, Orlando, Florida 32816

## Abstract

A dilatometer based on the cantilever beam concept has been developed. The dilatometer is easy to use and capable of measuring transverse strain response of soft polymer films in a broad strain range (from  $10^{-7}$  to  $10^{-1}$ ) without mechanical constraining of the sample. It is capable of detecting strain over a relatively wide frequency range from mHz to above 100Hz under different load and temperature. Using the set-up, the electric field induced transverse strains of the electrostrictive poly(vinylidene fluoride-trifluoroethylene) copolymer films were characterized which shows that a large transverse strain can be achieved in this class of polymer. In addition, the effect of mechanical tensile load on the transverse strain was also evaluated and the results show that the strain response will be affected by the load. However, depending on the load level, the strain response of the polymer film under a given electric field

may increase or decrease with load. Based on the phenomenological theory, it is shown that for a ferroelectric based material, the mechanical load will shift the Curie temperature. Hence, to a large extent, the change of the strain response with load observed here can be understood by linking it to the strain change with temperature.

PACS No: 77.84.Jd, 77.80.Bh, 07.10.Pz, 77.65. Bn

<sup>a</sup>Corresponding author, e-mail address: qxz1@psu.edu

## I. Introduction

Recently, it was found that a very large longitudinal electrostrictive strain (more than 4.5%) can be achieved in poly(vinylidene fluoride-trifluoroethylene) (P(VDF-TrFE)) copolymers under a proper electron irradiation treatment.<sup>1,2</sup> Further more, because of the relatively high elastic modulus, the polymer also exhibits a high elastic energy density which is crucial for many electromechanical actuator and transducer applications. These features represent a significant improvement in the electromechanical performance of this new material over the conventional electroactive ceramics and polymers.

For electromechanical applications,<sup>3</sup> in addition to the longitudinal response, the transverse response is also of great importance. In many devices operated in the longitudinal mode, a weak transverse strain response is desired which can reduce the mode coupling between the thickness direction and lateral directions for a thickness resonator or improve the device reliability. On the other hand, transverse strain responses are utilized in many areas and because the applied electric field is perpendicular to the strain direction, it offers a convenient means in generating actuation over large distances without the need to raise the driving voltage.

In this paper, we report the measurement of transverse strain response in the newly developed electrostrictive P(VDF-TrFE) copolymers. In order to characterize the strain response to high fields ( $\sim 50$  MV/m) without application of high voltages, thin polymer films of thickness about 20  $\mu\text{m}$  were used. One of the challenges in characterizing transverse strain response in thin polymer films is to measure the strain response in free standing form over a broad range without introducing constraints. To our knowledge, there is no existing instrument available for this type of measurement. Hence, in this paper we will first discuss the

development of a new setup which is simple, convenient to use, versatile, and capable of measuring transverse strain response of polymer films over a broad strain range. The performance of set-up was evaluated using the electric field induced transverse strains of both piezoelectric and electrostrictive polymeric films and the results show that the set-up is capable of characterizing transverse strain responses of polymer films with a high sensitivity over a relatively wide frequency range (from near static to above 100 Hz). The electric field induced transverse strains of electron irradiated (PVDF-TrFE) 65/35 mol% copolymer films under different load conditions are also presented, which illustrates that for ferroelectric based electroactive materials, the main effect of external mechanical loads on the electromechanical responses can be understood from the shift of the ferroelectric-paraelectric transition temperature caused by the loads.

## II. Dilatometer for Transverse Strain Measurement in Polymer Films

In general, the strain measurement techniques can be grouped into two categories: contact methods and non-contact methods.<sup>4</sup> The contact methods such as strain gauge and linear variable differential transformer (LVDT) which are used for transverse strain measurement in inorganic materials will impose severe constraints on polymer films due to low elastic modulus of polymers compared with inorganic materials.

For the non-contact method, although in principle laser dilatometer can be used to characterize the transverse strain response in polymer films, to reflect the laser beam mirrors are needed on two ends of the film which is a very difficult task. In addition, the sample holding is another challenge for a soft polymer film.<sup>5</sup> Optical microscope offers a convenient means to

characterize the transverse strain response.<sup>6</sup> However, its resolution is limited so that it cannot be used at low strain response region. In the case when a high applied electric field is required, and hence, the polymer film is immersed in insulation oil to increase the breakdown voltage, the operation of an optical microscope to obtain reliable results is quite difficult. In fact, these two methods have been tested and considered for transverse strain measurement of newly developed polymer films and no satisfactory results can be obtained.

From both the application and fundamental understanding points of view, the electromechanical properties of an electroactive material under mechanical loads are important parameters. Thus, in developing a new technique or set-up for characterizing the electromechanical behavior of materials, the capability of the set-up working when the material is under mechanical loads should be an important concern.

The set-up developed for characterizing transverse strain response of polymer films is shown schematically in Fig. 1(a). The key part of the set-up is a plastic cantilever which holds the polymer film to be measured under a slight tension as shown in Fig. 1(b). As seen from the figure, the polymer film to be tested has one end clamped at a solid base (fixed) and the other end attached to the free end of the plastic cantilever which is fixed at a solid base. When the polymer film is subjected to an electric field, its expansion and contraction cause the free end of the plastic cantilever to move which can be detected using optical technique. In the current set-up, a photonic sensor (Model 2000, MTI Instruments) is employed. However, if needed, a laser dilatometer can be used here to probe the movement of the free end of the cantilever which will yield a great sensitivity. This is one of the advantages of this setup, that is, the displacement probe and mechanical holding part are two separate units and can be changed separately without affecting the other part.

The photonic sensor with the optic probe (MTI 2032R) has two sensitivity ranges: the sensitivity for range 1 is 0.019  $\mu\text{m}/\text{mV}$  and for range 2 is 0.137  $\mu\text{m}/\text{mV}$ . All the measurements were conducted at AC mode. The output signal of the photonic sensor was measured/recorded through a Lock-in Amplifier (SRS Model SR 830 DSP) at small strain region and/or a digital oscilloscope (LeCroy 9310A) at high strain region of polymer films. The output signal noise of the photonic sensor, whose working frequency is from DC to 100 kHz, is about 10mV<sub>p-p</sub>. The working frequency of the lock-in amplifier is from 0.005Hz to 100 kHz. The lock-in amplifier has a dynamic reserve greater than 100 dB which makes it possible to measure a signal of a few  $\mu\text{V}$  in a 10 mV noise background.

We now proceed to describe the details of the set-up. The symbols used are summarized here. For the polymer film under test,  $L$  is the length,  $t$  is the thickness,  $A$  is the cross section area, and  $E_t$  is the elastic modulus in the transverse direction. The typical values of  $t$ ,  $A$ , and  $L$  are about 20  $\mu\text{m}$ ,  $6 \times 10^{-2} \text{ mm}^2$ , and 12 to 15 mm, respectively. For the plastic cantilever,  $l$  is the length,  $h$  is the thickness,  $b$  is the lateral width, and  $E_c$  is the elastic modulus. For the data presented in this section, the values of  $b$ ,  $h$ , and  $l$  are about 6 mm, 0.8 mm, and 80 mm, respectively. The typical value of  $\delta_0$ , which is the static displacement of cantilever's free end from its equilibrium position as shown in Fig. 1(b), is 2 mm. The elastic modulus of the plastic cantilever used is about 5 GPa. For the plastic cantilever with one end firmly fixed, the deflection  $\delta_0$  at the free end will generate a static force ( $F$ ) which are related to each other as:<sup>7</sup>

$$\delta_0 = \frac{1}{3} \frac{Fl^3}{E_c I} \quad (1)$$

where  $I$  (in  $\text{m}^4$ ) is the inertia moment of the cantilever,

$$I = \frac{1}{12}bh^3 \quad (2)$$

Combing the two equations yields

$$\delta_0 = 4 \frac{Fl^3}{E_cbh^3} \quad (3a)$$

or

$$F = \frac{E_cbh^3}{4l^3} \delta_0 \quad (3b)$$

Because the polymer film is directly attached to the free end of the cantilever, this force will act as a static tensile load to the polymer film. Apparently, Eq. (3) shows that by adjusting  $\delta_0$ ,  $h$ , and other parameters of the cantilever, the mechanical load can be varied over a wide range. This is another advantage of this set-up.

As the polymer film is subjected to an AC electric field, its expansion and contraction will induce a corresponding AC motion in the free end of the cantilever as shown by the dashed lines in Fig. 1(b). As long as this displacement  $\delta(E)$  is in the range " $\delta_0 + \delta(E) > 0$ ", the strain response of the film can be measured. For the piezoelectric PVDF and electrostrictive P(VDF-TrFE) copolymer films studied here,  $\delta(E)$  is in the range from 0 to  $-0.4$  mm. As the polymer film extends or contracts under applied fields, the free end of the cantilever will move as

$$\delta(E) = -L [d_{13}E_3 + M_{13}E_3^2] - \frac{L}{AE_s} \frac{E_cbh^3}{4l^3} \delta(E) \quad (4)$$

where  $E_3$  is the applied electric field (along the thickness direction, 3-direction),  $d_{31}E_3$  describes the piezoelectric effect, and  $M_{13}E_3^2$  the electrostrictive effect in the polymer film, respectively.<sup>8</sup> The last term in Eq. (4) is due to the dynamic load from the cantilever since a change in  $\delta$  will cause change in the force level at the free end of the cantilever as shown in Eq. (3). In fact, this

term can be made use of to evaluate the change of the elastic modulus of the polymer film with external load. The measured transverse strain response of the polymer film is

$$S(E) = \frac{-\delta(E_3)}{L} = \frac{d_{13}E_3 + M_{13}E_3^2}{1 + \Delta} \quad (5)$$

$$\Delta = \frac{S_0 L}{\delta_0} = \frac{E_c b h^3}{4l^3} \frac{L}{AE_s}$$

where,  $\Delta > 0$ ,  $S_0$  is the static strain of the sample corresponding to the static load originated from the static displacement ( $\delta_0$ ) of cantilever's free end. In the current set-up,  $\Delta$  is much smaller than 1 (on the order of 0.001) and hence, the strain response can be linked directly to the piezoelectric and electrostrictive coefficients of the polymer evaluated, i.e.,

$$S(E) = d_{31}E_3 + M_{13}E_3^2 \quad (6)$$

Eq. (6) expresses the transverse strain response under an external electric field  $E_3$  for a film under a constant mechanical stress. In present case, the constant stress on the sample originates from the static force which is determined by the static displacement ( $\delta_0$ ) of cantilever's free end as shown in Eq. (3). Since, for most electroactive materials, both  $d_{13}$  and  $M_{13}$  will depend on the stress (load),<sup>9,10</sup> the dilatometer can be used to characterize the electromechanical properties of polymeric films under different load conditions.

In the set-up, special consideration and design were made so that the film under test can be immersed in an oil chamber, which serves to increase the breakdown electric field so that the measurement can be carried out to high fields. Thus, the temperature of the sample is the same as the temperature of the oil. Since the temperature of the oil can be easily changed, the set-up can be used to evaluate the transverse strain responses of polymer films with temperature. During the development of the set-up, it was found that in order to reduce the error in the measured strain response, it is necessary to keep the film flat. Therefore, a stage which is

capable of translating the cantilever in three orthogonal directions as well as rotation in one of the axes is used.

The set-up is calibrated using a commercial piezoelectric PVDF film whose  $d_{31}$  value is known. As shown in Fig. 2(a), the strain versus applied field exhibits a linear curve, indicating the response is piezoelectric as expected. The piezoelectric coefficient  $d_{13}$  is determined through the electric field strength and measured transverse strain. The results, which are consistent with the value from the manufacturer, are shown in Fig. 2(b).

The displacement sensitivity was also evaluated using the newly developed electrostrictive P(VDF-TrFE) 65/35 mol% copolymer and the results are presented in Fig. 3. The data were obtained at 1 Hz applied field with the time constant of 30 seconds for the lock-in amplifier. For the range 1 of the photonic sensor, the lowest measurable displacement is about 0.1 nm, while for the range 2, it is about 1 nm. Considering a fact that  $L=10$  mm, the results indicate that the set-up is capable of measuring transverse strain to  $10^{-7}$  range. On the other hand, the photonic sensor used here can measure displacement up to 0.7 mm range which corresponds to a strain in polymer films of 0.07. However, photonic sensors with the upper range to more than 5 mm is commercially available. Clearly, the separation of the sample holding unit and displacement sensing unit in the set-up enables us to characterize the strain in polymer films over a very wide range. In addition, the linear log-log plot of the data in figure 3 implies that the strain response of the polymer follows  $S(E)=M_{13}E^n$  relation (power law) and slopes yield  $n=1.99$  and  $n=2.08$ , respectively, which is consistent with the longitudinal strain data on the similar films measured in the low field range ( $<10$  MV/m) and shows that the response is electrostrictive ( $n=2$ ).<sup>2</sup> The electrostrictive coefficient  $M_{13}$  calculated from the data in Fig. 3 is  $1.9 \times 10^{-18} \text{ m}^2/\text{V}^2$ .

The operation frequency range is another concern when developing a strain measurement set-up. At the low frequency end, the frequency limit depends on the frequency range of a lock-in amplifier and the strain level of the sample. The limiting frequency for the former is 0.005 Hz in the present system. And the later is caused by the increased noise of the environment which has approximately  $1/f$  spectrum, where  $f$  is frequency. On the high frequency end, the operation frequency is limited by the resonance frequency ( $f_1$ ) of the cantilever. The lowest resonance frequency of a cantilever with one end fixed and the other free is given by:<sup>11</sup>

$$f_1 = 0.16154 \frac{h}{l^2} \sqrt{\frac{E_c}{\rho}} \quad (7a)$$

While the lowest resonance frequency of a cantilever with two ends fixed is determined by:<sup>11</sup>

$$f_1' = 1.0279 \frac{h}{l^2} \sqrt{\frac{E_c}{\rho}} \quad (7b)$$

where  $\rho$  (in  $\text{kg/m}^3$ ) is the density of the plastic probe used. Since in our set-up, one end of the cantilever is fixed firmly at a base and another end is not totally free (attached to the polymer film), the resonance frequency should be somehow in between the  $f_1$  and  $f_1'$  of Eq. (7).

Therefore, as the polymer film is driven electrically with increasing frequency, a series of resonance in the cantilever will be excited. For example, the frequency response data using the commercial piezoelectric PVDF film as the polymer sample attached to the cantilever probe is presented in Fig. 4(a). A resonance was observed at a frequency of the AC driving electric field at about 170 Hz for a cantilever beam with  $\rho = 1.47 \times 10^3 \text{ kg/m}^3$  and  $E_c = 5 \text{ GPa}$ , and the result is in accord with what was expected from Eq. (7). The weak frequency dependence of the piezoelectric coefficient at frequencies below 50 Hz as shown in Fig. 4(a) is consistent with what measured in a thick copolymer sample (mm thickness) of P(VDF-TrFE) 75/25 mol%

piezoelectric copolymer.<sup>5</sup> With the same probe, the frequency dependence of transverse strain response of a newly developed electrostrictive copolymer film under a field of 35.7 MV/m (P(VDF-TrFE) 50/50 mol% irradiated at 95 °C with 100 Mrad dose) was also characterized. As shown in figure 4(b), there is a resonance at a frequency near 90 Hz of the AC driving electric field. The apparent lowering of the resonance frequency here is caused by the electrostrictive response of the polymer film ( $S=ME^2$ ) which generates a mechanical motion of  $2f$  frequency when the driving electric field has a frequency  $f$ . Apparently, at below 50 Hz, the effect of the resonance to the measured data is negligible here. By adjusting the dimension of the cantilever probe, one can raise the resonance frequency to above 500 Hz which makes it possible to characterize the transverse strain response of a polymer film up to more than 100 Hz if needed.

### III. Transverse Strain Response of Irradiated P(VDF-TrFE) 65/35 Copolymer

In this section, the change of the transverse strain of stretched films (5x stretching ratio) of P(VDF-TrFE) 65/35 copolymer with mechanical load was evaluated. Shown in Fig. 5 is the transverse strain response as a function of applied field measured at room temperature for films with different irradiation conditions under load free condition. Clearly, the response depends strongly on the irradiation condition.

With regard to electroactive materials for electromechanical applications, although the electric field induced strain response at load free condition is important to understand and to characterize the materials behavior, the material response when subjected to external load is crucial for most of the device applications. Needless to say, the information is also valuable

from a basic understanding point of view. Here, the film irradiated at 95 °C with 60 Mrad dosage is examined under different mechanical load conditions, since this is the one that exhibits the best transverse strain response at load free condition as seen from Fig. 5. In order to vary the mechanical load over a broad range, plastic cantilever beams with thickness from 0.8 mm to 4 mm were used. The  $E_c$  of the plastic trips is from 2.5 GPa to 6 GPa. In addition, the static displacement ( $\delta_0$ ) of cantilever's free end was varied from 2 mm to 6 mm. Thus, the static tensile load on the polymer film can change from nearly zero to more than 45 MPa.

The relation between the electric field and the transverse strain response for the sample under different static tensions is shown in Fig. 6(a). The static tension dependence of electric field induced strain for the same material at different external electric fields is shown in Fig. 6(b). In these experiments, the load (stress) was along the stretching direction of the copolymer film and the transverse strain was also measured along the stretching direction. Although the strain response of a sample at the same electric field strongly depends on the static tension, it is found that at a low electric field ( $<15\text{MV/m}$ ) the strain response for the sample under different static load conditions always linearly depends on the square of the electric field strength. This is what is expected from the electrostrictive effect.<sup>1,2</sup> However, the electrostrictive coefficient depends strongly on the static load.

The results in Fig. 6 indicate that for a given field, the transverse strain increases with load initially and then decreases with the load after reaching the maximum. For the polymer studied here, the electric field induced strain response mainly originates from the phase changes from a non-polar to a polar phase under external electric field.<sup>1,11,12,15</sup> Hence, this load dependence behavior can be understood based on how this change is affected by the load.

Before the electron irradiation, the copolymer exhibits typical first order phase transition from para- to ferro- electric phase.<sup>1,14</sup> However, after the electron irradiation, the physical properties of the copolymer are very similar to that of relaxor ferroelectrics.<sup>1,15</sup> For relaxor ferroelectrics, it is known that the local phase transition temperature (or the freezing temperature of the polar region) is distributed in a very broad range and that the density of the frozen polar regions increases with decreasing temperature.<sup>15,16</sup> Thus, the dielectric behavior and the electric field induced strain response strongly depends on the temperature. For relaxor ferroelectrics under stress free condition, there is a broad dielectric constant maximum at a temperature ( $T_m$ ) which depends on the frequency. It is believed that the density of the frozen polar region is relatively large and the interaction between the frozen polar regions is still not high at temperatures near  $T_m$ .<sup>16</sup> In addition, the relaxor ferroelectrics has another characteristic temperature, depolarization temperature ( $T_d$ ) which is lower than  $T_m$  by a few tenths degrees.<sup>15,17</sup> At temperatures lower than  $T_d$ , most of the polar regions are frozen and the interaction among the frozen polar regions is relatively high. Thus, both  $T_m$  and  $T_d$  can be used as parameters to characterize the average phase transition temperature of local transition between para- and ferro-electric phases. For the material studied here, the  $T_m$  is about 27 °C at 30 Hz as measured from the dielectric data.<sup>18</sup> It has been observed that under a relatively high driving electric field, it is expected that the induced strain will increase as the temperature is lowered towards  $T_d$ .<sup>19</sup> However, as the temperature is lowered further, the strain response will decrease due to increased 180° domain wall motions associated with the macro-polarization switching.

Based on Devonshire phenomenological theory, for a ferroelectric material under a stress  $X_i$  and with a polarization ( $P_3$ ) along "3" direction, if only consider the contribution to the

free energy of the system from the electrostrictive effect (first order approximate),<sup>20</sup> the shift of phase transition temperature with stress is:

$$\Delta T = 2\varepsilon_0 C Q_{i3} X_i \quad (8)$$

Where  $\Delta T = T_c(X_i) - T_c(0)$ ,  $\varepsilon_0 = 8.85 \times 10^{-12}$  F/m,  $C$  is the Curie-Weiss constant,  $Q_{i3}$  is the electrostrictive coefficients defined as  $S_i = Q_{i3} P_3^2$  and  $T_c$  is the Curie temperature. Although the Eq. (8) is written for a single crystal normal ferroelectrics, the trend should be the same also for the relaxor ferroelectrics considering the micro-structure of the relaxor ferroelectrics. For relaxor ferroelectrics, the stress will shift both  $T_m$  and  $T_d$  and the direction of the shifting will depend on the sign of  $Q$ , the electrostrictive coefficient. For the polymer investigated here,  $Q_{i3} > 0$  and the applied stress is  $X_i > 0$ . Thus, equation (8) shows that  $\Delta T > 0$ . That is, both  $T_m$  and  $T_d$  of the sample will move to a higher temperature with the tensile load.

This result indicates that the measured strain responses at room temperature for films under different load are, to a large extent, equivalent to the strain responses measured at different temperatures under stress free condition. Since  $T_m$  for the polymer under free stress condition is close to room temperature, the measured strain response will increase with tensile stress. This is what was obtained at the low load range as show in Fig. 6. However, as the load increases further which moves  $T_d$  to higher than room temperature, the strain response will decrease. Below  $T_d$ , most of polar regions are frozen and the interaction among the frozen polar regions is very high. Thus, the contribution to the electric field induced strain from the para- to ferro- electric phase transition decreases. This is why the electrostrictive response decreases with load in the high load region as shown in Fig. 6.

#### IV. Summary and Acknowledge

A new dilatometer is developed for characterizing the electric field induced transverse strain of free standing polymer films under different load conditions and at different temperatures. The set-up is easy to use, can be operated in a broad strain range with high sensitivity, and has a reasonable operation frequency range, from mHz to above 100 Hz. Using the dilatometer, the electric field induced transverse strains of high energy electron irradiated P(VDF-TrFE) films were characterized. It was found that a high transverse strain response can be achieved in this class of material which depends crucially on the irradiation condition. It was also found that the field induced strain will change with external load. For example, for P(VDF-TrFE) 65/35 mol% copolymer irradiated at 95 °C with 60 Mrad dosage, the transverse strain measured at room temperature increases with tensile load initially until a load near 15 MPa, beyond that the strain decreases slowly with the load. Based on Devonshire phenomenological theory, it can be shown that for the polymer investigated here, the tensile stress will favor the low temperature phase and the change of the strain with load can be understood qualitatively from the shifting of  $T_m$  and  $T_d$  due to the load. In general, for ferroelectric based materials, the dependence of strain response with load can be understood from the shifting of the Curie temperature with stress.

This work was supported by the National Science Foundation through Grant No ECS-9710459 and the Office of Naval Research through Grant No N00014-97-1-0900.

## References

1. Q. M. Zhang, V. Bharti, X. Zhao, *Science*, **280**, 2101 (1998).
2. X. Zhao, V. Bharti, Q. M. Zhang, T. Romotowski, F. Tito, and R. Ting, *Appl. Phys. Lett.* **73**, 2054 (1998).
3. J. M. Herbert, *Ferroelectric transducers and sensors* (Gordon and Breach Science Publishers, New York, 1984).
4. J. Su, P. Moses, and Q. M. Zhang, *Rev. Sci. Instrum.*, **69**, 2480 (1998).
5. H. Wang, Ph. D. Thesis, The Pennsylvania State University, 1994.
6. R. E. Pelrine, R. D. Kornbluh, and J. P. Joseph, *Sensors and Actuators*, **A64**, 77 (1998).
7. K. Lingaiah, *Machine Design Data Handbook* (McGraw-Hill, Inc. New York, 1994).
8. IRE Standards on Piezoelectric Crystals, *Proc. IRE* **49**, 1169 (1961).
9. Q. M. Zhang, W. Y. Pan, S. J. Jang, L. E. Cross, *Ferroelectrics* **88**, 147, (1988).
10. J. Zhao, et al. To be published in *Appl. Phys. Lett.* (1999).
11. J. Merhaut, *Theory of Electroacoustics* (McGraw-Hill, Inc. New York, 1981).
12. Z. -Y. Cheng, et al. Submitted to *Appl. Phys. Lett.*
13. K. Tashiro, in *Ferroelectric Polymers*, H. S. Nalwa, Ed. (Dekker, New York, 1995), pp. 63-181.
14. T. Furukawa, *Phase Transition*, **18**, 143 (1989).
15. L. E. Cross, *Ferroelectrics*, **76**, 241 (1987).
16. Z. -Y. Cheng, R. S. Katiyar, X. Yao, and A. S. Bhalla, *Phys. Rev. B* **57**, 8166 (1998).
17. V. Bharti, X. Zhao, Q. M. Zhang, T. Ramotowski, F. Tito, and R. Ting, *J. Mater. Res. Innovations* **2**, 57 (1998).

18. Q. M. Zhang, To be published.
19. J. Zhao, Q. M. Zhang, N. Kim, T. Shrout. Jpn. J. Appl. Phys. **34**, 5658 (1995).
20. M. E. Lines and A. M. Glass, *Principles and Applications of Ferroelectrics and Related Materials* (Oxford University Press, New York, 1977).

## Figure Captions

- Fig. 1 Schematic of the setup (a) where the stable stage can move along x-y-z directions as well as rotate about the x-axis. The displacement of cantilever's free end (b). In the experiment,  $\delta_0$  and  $\delta(E)$  are much smaller than  $l$ , the length of the cantilever
- Fig. 2 Transverse strain (a) and corresponding piezoelectric constant,  $d_{31}$ , (b) of pure PVDF piezoelectric film under different electric fields of 1 Hz at room temperature.
- Fig. 3 The displacement sensitivity of the system when the photonic sensor is in the range one and two.
- Fig. 4 Frequency dependence of the electric field induced transverse strain of PVDF piezoelectric film (a) and P(VDF-TrFE) electrostrictive film (b) under a constant electric field.
- Fig. 5 The electric field dependence of the transverse strain measured at room temperature for stretched 65/35 mol% P(VDF-TrFE) copolymer films under different electron irradiation conditions.
- Fig. 6 The load effect on the electric field induced transverse strain response measured at room temperature with applied electric field of 1 Hz for 65/35 mol% P(VDF-TrFE) copolymer film irradiated at 95 °C with 60Mrad dosage. (a). The relation between the strain response and electric field for films under different loads. (b). The relation between strain response and static load for films at different electric field strengths. Symbols in figure express the measured data, while solid lines in figure are drawn to guide eyes.

Fig. 1(a)

Z. -Y. Cheng, et al.

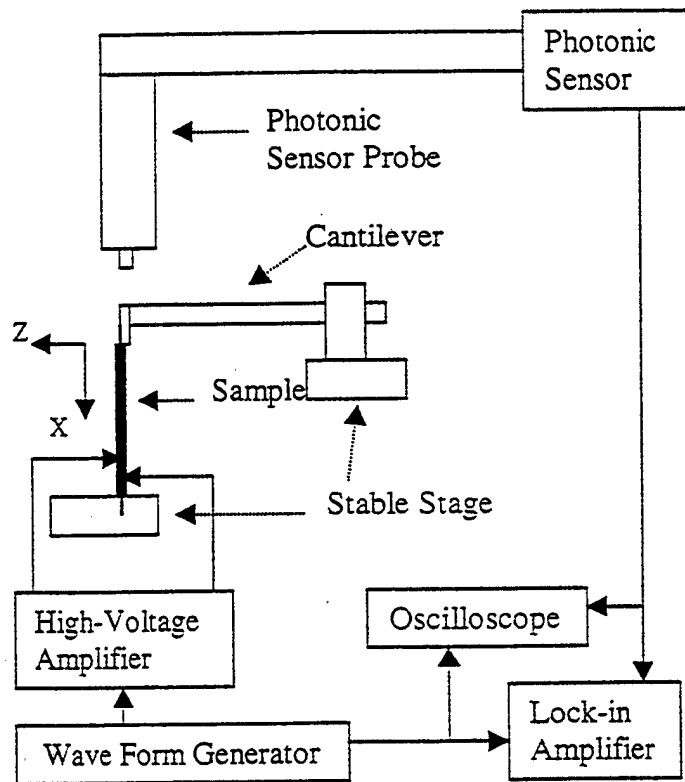


Fig. 1(b)

Z. -Y. Cheng

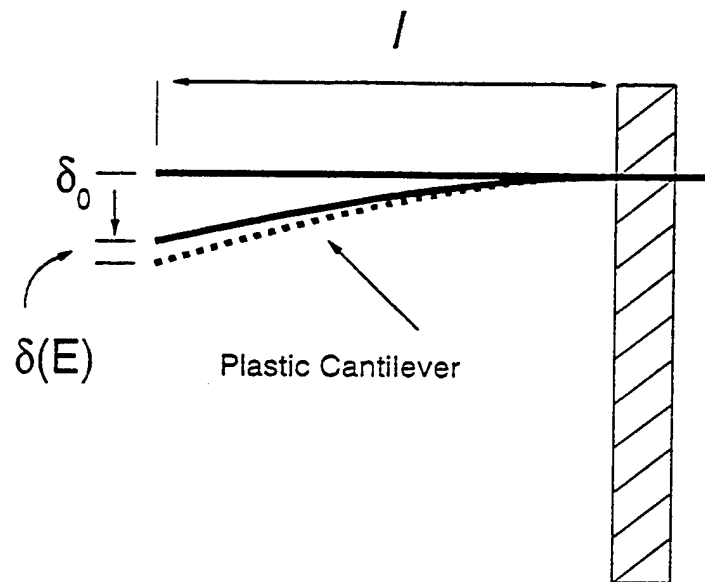


Fig. 2

Z. -Y. Cheng, et al.

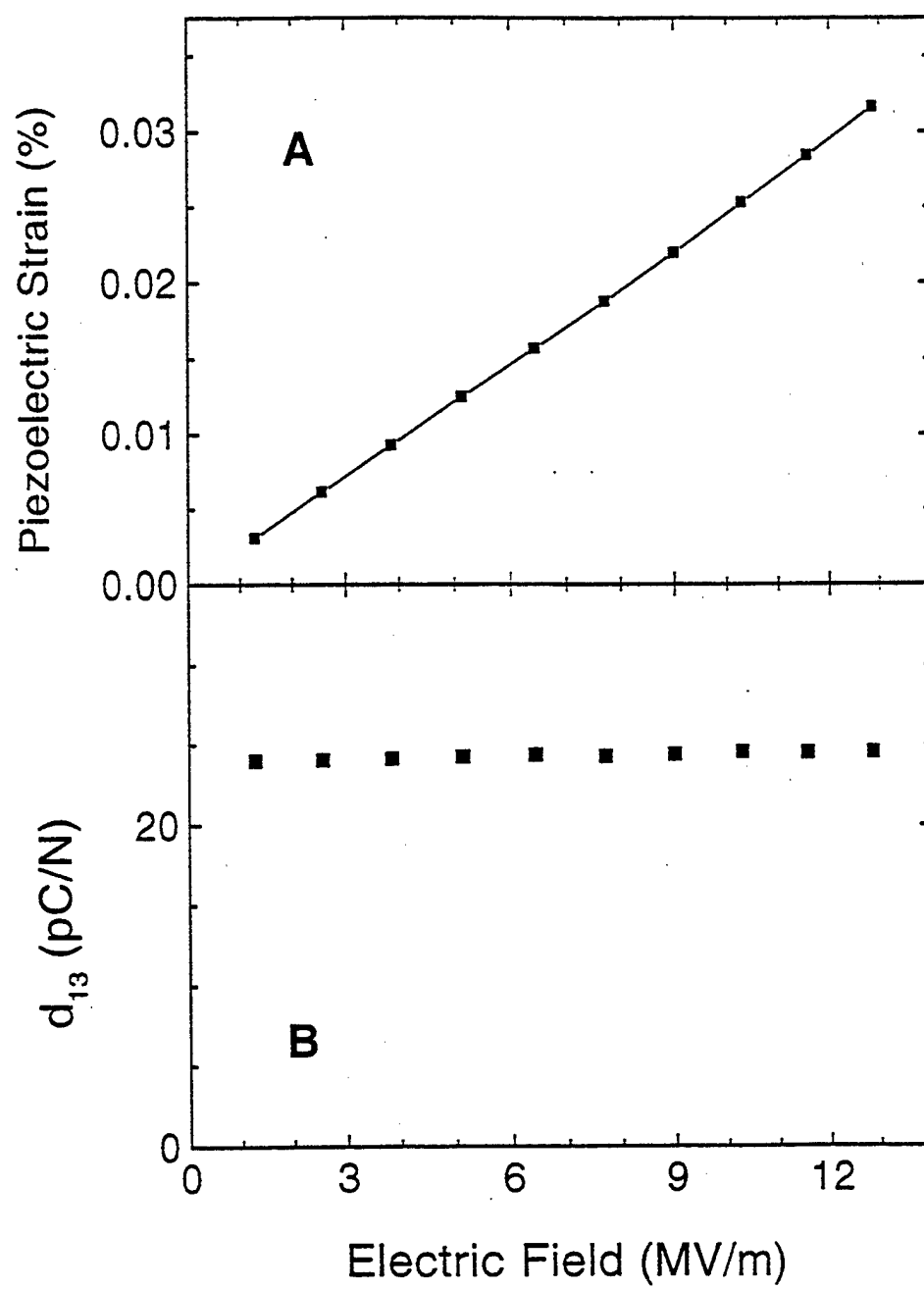


Fig. 3 Z. -Y. Cheng, et al.

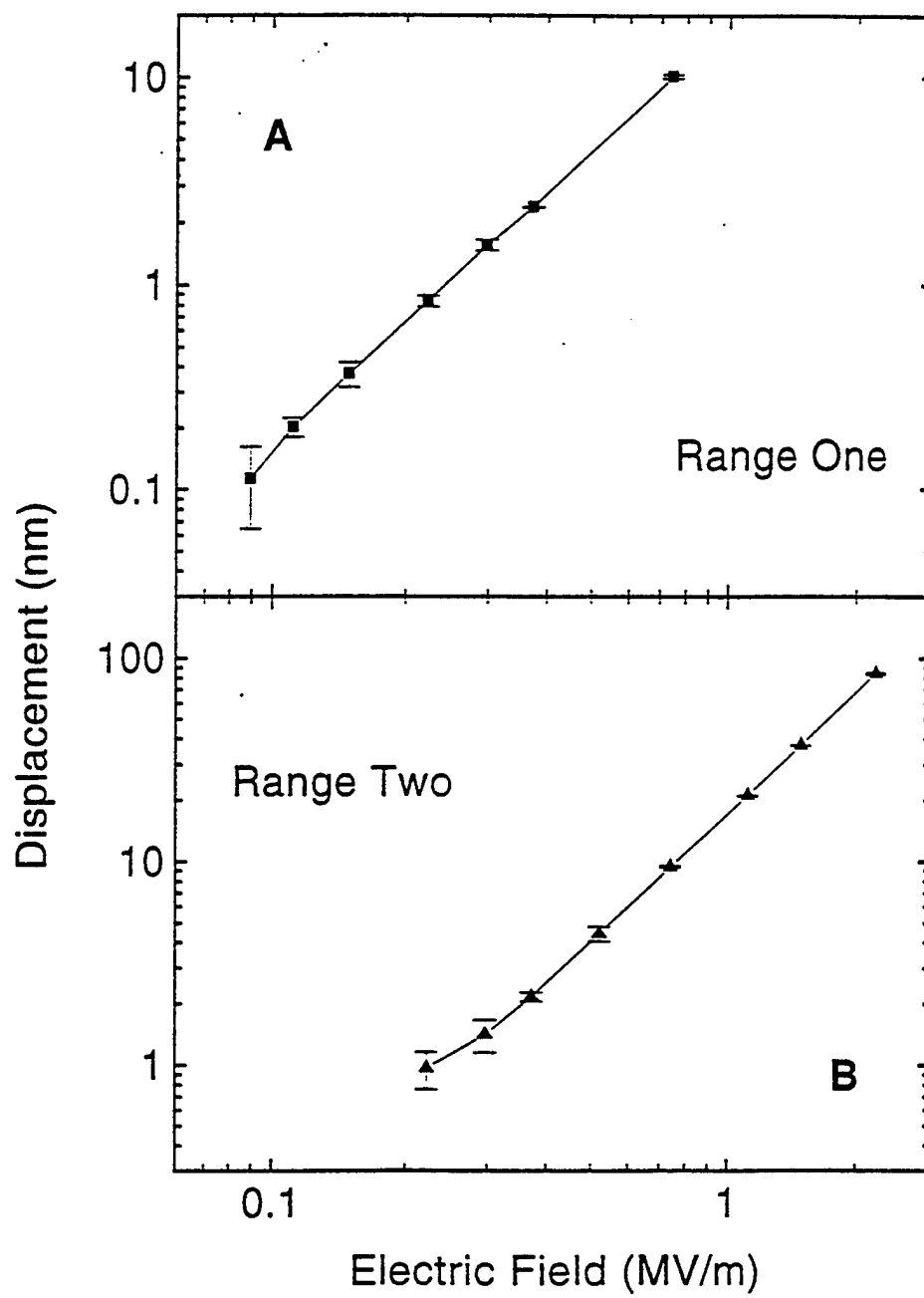


Fig. 4 (A)

Z. -Y. Cheng, et al.

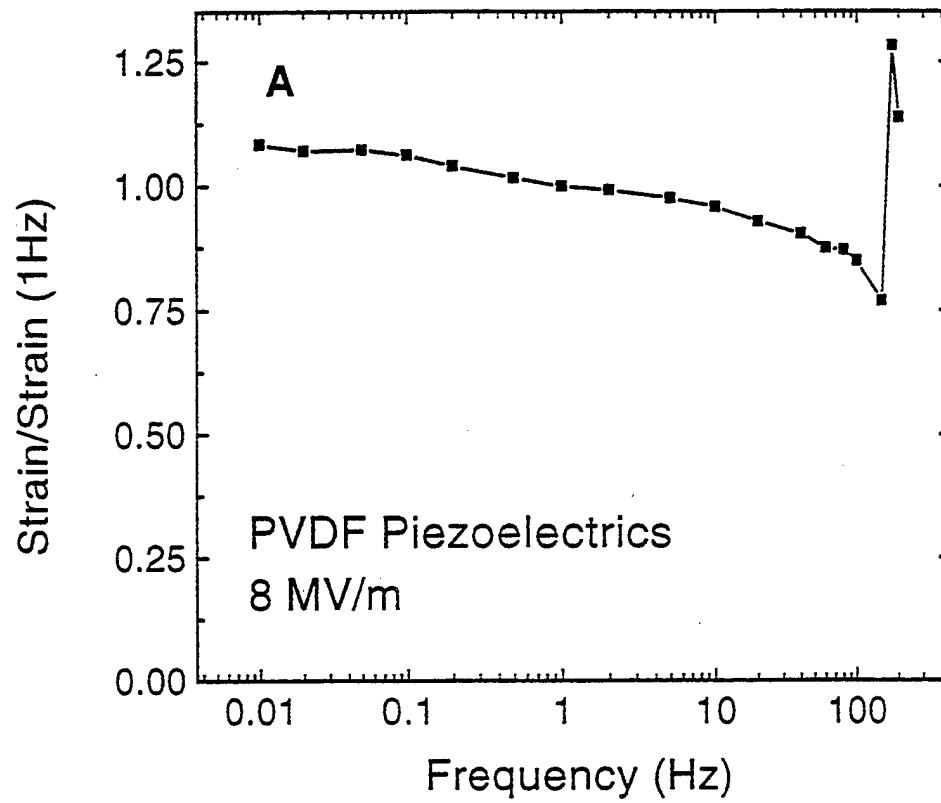


Fig. 4 (B)

Z. -Y. Cheng, et al.

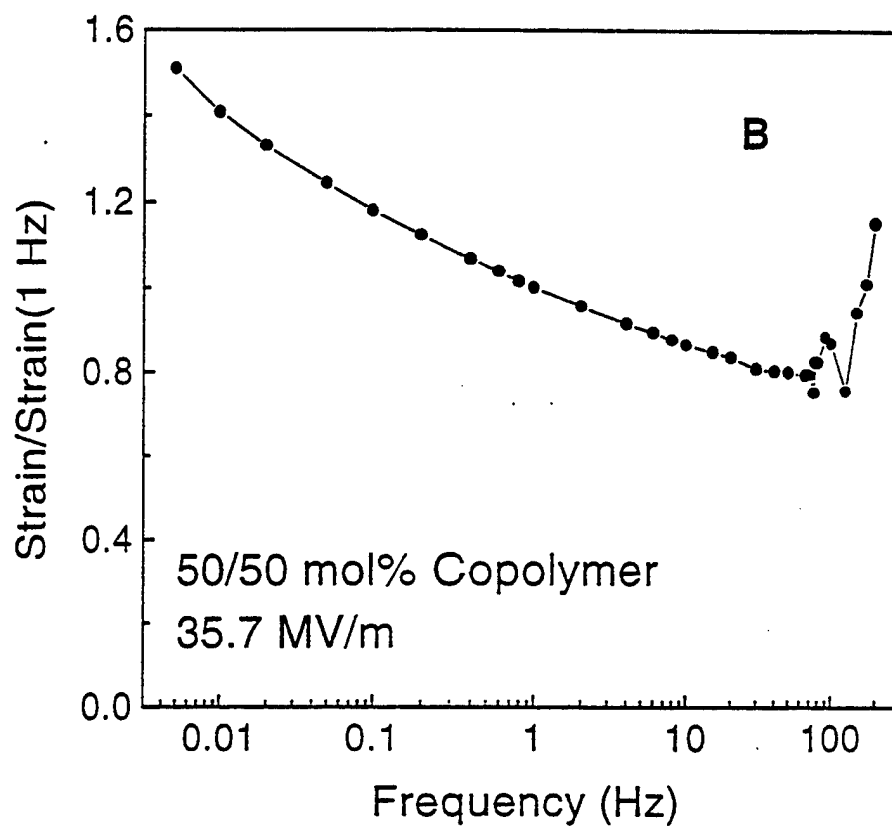


Fig. 5 Z. -Y. Cheng, et al.

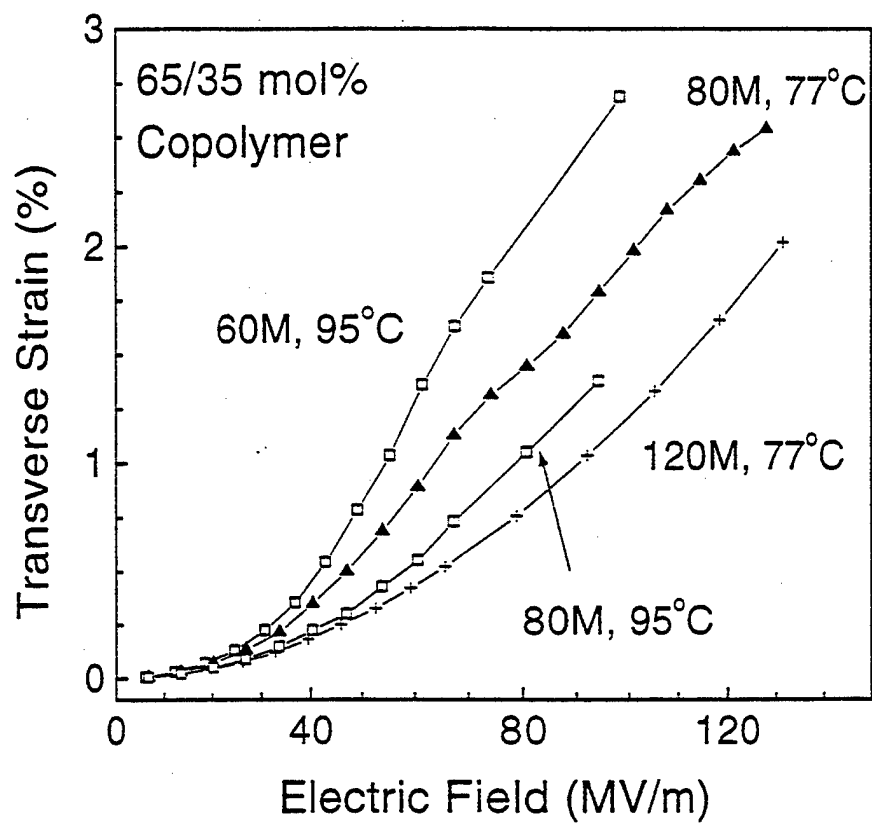


Fig. 6(A) Z. -Y. Cheng, et al

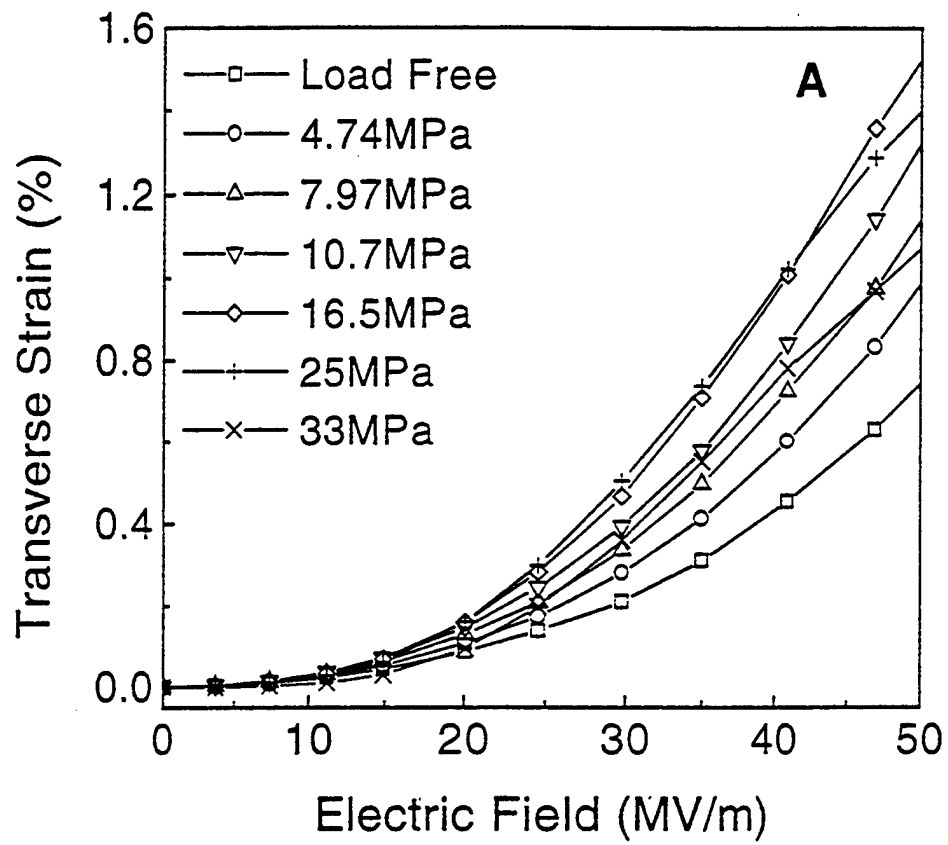


Fig. 6(B)

Z. -Y. Cheng, et al

